MODELING OF LIQUID WATER AND IONIC SOLUTIONS BY FIRST-PRINCIPLES SIMULATIONS

A Dissertation
Submitted to
the Temple University Graduate Board

---

in Partial Fulfillment
of the Requirements for the Degree of
DOCTOR OF PHILOSOPHY

---

by
Jianhang Xu
December 2020

Examining Committee Members:

Dr. Xifan Wu, Advisory Chair, Temple University Department of Physics
Dr. Adrienn Ruzsinszky, Temple University Department of Physic
Dr. Qimin Yan, Temple University Department of Physic
Dr. Vincenzo Carnevale, Temple University Department of Chemistry

©

by

Jianhang Xu

December 2020

All Rights Reserved

ABSTRACT

MODELING OF LIQUID WATER AND IONIC SOLUTIONS BY FIRST-PRINCIPLES SIMULATIONS

Jianhang Xu

DOCTOR OF PHILOSOPHY

Temple University, December 2020

Dr. Xifan Wu, Chair

Water is one of the most important materials and has enormous impacts on life. Due to its delicate Hydrogen bond (H-bond) network, water shows various anomalous properties which has not been fully illuminated. Advanced experimental methods, such as scattering experiments and various spectroscopy techniques, have been developed and applied to study the nature of H-bond in liquid water. On the other hand, *ab initio* molecular dynamics (AIMD) have been widely adopted as an important theoretical tool to provide microscopic information of water on a sub-picosecond timescale. Recent AIMD studies based on the strongly constrained and appropriately normed (SCAN) exchange correlation functional yield an excellent description of the structural, electronic, and dynamic properties of liquid water.

In this dissertation, we will focus on studying the structural, electronic and dynamic properties of liquid water as well as the modeling of the hydration structures of ions in aqueous solutions, using AIMD with potential energy surface provided by the novel SCAN functional. In the first work we represent an accurately predicted

infrared spectrum of liquid water and show how the improvements are connected to the description of the underlying H-bond network. The second work mainly focusing on modeling the nuclear quantum effects (NQEs) and isotope effect of liquid water with a force field model based on artificial neural network, where qualitative agreements with experimental observations are achieved. In the third work, we study the isotope effect on the x-ray absorption spectra of liquid and attribute observed differences to the structural distinctions between light and heavy water as mentioned in the previous work. And in the last two projects, we systematically show the necessity of including NQEs of the hydrogen atom when modeling chloride ionic solution. Prominent changes in the hydration structure as well as electronic structure can be identified when NQEs are taken into consideration.

To my parents.

ACKNOWLEDGEMENTS

First of all, I would like to thank my advisor Dr.Xifan Wu for the kindly and detailed instruction and support in both academic work and personal life. I have learned a lot from you. I would also like to thank my committee: Dr. Adrienn Ruzsinszky, Dr. Qimin Yan and Dr. Vincenzo Carnevale for the helping in the writting process of this dissertation. I would like to acknowledge post-doctoral fellows in our group, Dr. Mohan Chen, Dr. Hongwei Wang, Dr. Zhaoru Sun, Dr. Fujie Tang and Dr. Chunyi Zhang. Thanks for introducing me into this fascinating field, teaching me how to conducting calculations and discussing with me during projects. The dissertation is composed of the materials in my papers and manuscripts. Here, I give special thanks to all the co-authors in my works for their great work and fruitful discussions. Also to my roommates: Siyu Wu, Shaoyang Wu and other wonderful friends: Jeng-yuan Tsai, Baozhu Lu, Xunzhen Yu, Fei Qin and more, I have spend so much great time with you on delicious food, beautiful scenery... Special thanks to my fiancee Shuo Jia. You are always there accompanying me and supporting me, especially during this pandemic. Finally, my sincerely thanks to my beloved parents Chengde Xu and Juan Cai. Only with you, I become who I am today.

Contents

ABSTRACT **iv**

DEDICATION **vi**

ACKNOWLEDGEMENT **vii**

LIST OF FIGURES **x**

LIST OF TABLES **xii**

1 INTRODUCTION **1**

2 BACKGROUND **6**
2.1 Theoretical background 6
2.1.1 Born-Oppenheimer approximation 6
2.1.2 The Hohenberg-Kohn theorem 7
2.1.3 The Kohn-Sham equation 9
2.1.4 Exchange-correlation functionals 12
2.1.5 *Ab initio* molecular dynamics 15
2.2 Water in liquid phase 21
2.2.1 Properties of liquid water 21
2.2.2 Modeling of liquid water 24

3 INFRARED SPECTRUM OF LIQUID WATER **28**
3.1 Introduction 28
3.2 Methods to compute infrared spectra in liquid water 31
3.3 Simulated infrared spectra 33
3.3.1 Stretching modes 34
3.3.2 Bending mode 39
3.3.3 Far-infrared modes 41
3.4 Conclusion 44

4 NUCLEAR QUANTUM EFFECTS AND ISOTOPE EFFECTS ON LIQUID WATER **46**
4.1 Introduction 46
4.2 Methods 49
4.3 Proton transfer coordinates 53

4.4 Radial distribution functions 56
4.5 Statistics of H-bond ordering 62
4.6 Electronic properties 65
4.7 Conclusion 69

5 ISOTOPE EFFECTS ON X-RAY ABSORPTION SPECTRA OF LIQUID WATER 71
5.1 Introduction 71
5.2 Methods to compute XAS in liquid water 74
5.3 Simulated x-ray absorption spectra 75
5.3.1 Pre-edge 78
5.3.2 Main-edge 80
5.3.3 Post-edge 82
5.4 Conclusion 83

6 NUCLEAR QUANTUM EFFECTS ON THE HYDRATION OF CHLORIDE ION 85
6.1 Introduction 85
6.2 Method 89
6.3 Competing NQEs on H-bond 89
6.4 NQEs on the first hydration shell of Cl^- ion 92
6.5 NQEs on the perturbed liquid water structure 95
6.6 Conclusion 97

7 NUCLEAR QUANTUM EFFECTS ON THE ELECTRONIC STRUCTURE OF CHLORIDE SOLUTION 99
7.1 Introduction 99
7.2 Method 103
7.3 Computed quasiparticle density of states 104
7.4 Connections between molecular and electronic structures 106
7.5 Conclusion 111

BIBLIOGRAPHY 112

APPENDICES

A COMPUTATIONAL RESOURCES AND SOFTWARE 130

B SUPPORTING INFORMATION FOR CHAPTER 5 133

C SUPPORTING INFORMATION FOR CHAPTER 6 140

D SUPPORTING INFORMATION FOR CHAPTER 7 151

E LIST OF PUBLICATIONS 154

LIST OF FIGURES

2.1 Molecular structure of water 21
2.2 Tetrahedral structure of H-bond 22
2.3 Radial distribution function 24

3.1 Infrared spectra of liquid water 33
3.2 Comparison of vibration modes in water vapor and liquid water . . 35
3.3 Spacial decomposed infrared spectra of liquid water 36
3.4 First order rotational correlation functions of liquid water 43

4.1 Flow diagram of DP-GEN active learning procedure 49
4.2 Proton transfer coordinate in liquid water 54
4.3 O-O radial distribution functions in liquid water 57
4.4 O-H radial distribution functions in liquid water 59
4.5 H-H radial distribution functions in liquid water 61
4.6 Distribution of H-bond numbers in liquid water 62
4.7 O-O-O angular distributions in liquid water 64
4.8 Density of state of liquid water 66
4.9 Distributions of maximally localized wannier function centers in liquid water 67
4.10 Distribution of dipole moments in liquid water 68

5.1 X-ray absorption spectra in liquid water with isotope effects 75
5.2 Structural changes in liquid water under isotope effects 77
5.3 Short range ordering features of H-bond network (pre-edge) 78
5.4 Intermediate-range ordering features of water (main-edge) 81

6.1 Distribution of maximally localized Wannier function centers of water in chloride solution 90
6.2 Proton transfer coordinates in chloride solution 91
6.3 Structural features of the hydration of chloride ion 93
6.4 Destructive effects of chloride ion on the structure of liquid water . 96

7.1 Quasiparticle density of states of chloride solution 104
7.2 Spacial distributions of Cl-O pairs and chloride $3p$ orbital charge density 107
7.3 Polarized structures of the hydration of chloride ion 108

B.1 Comparison of O-O radial distribution functions from PI-DPMD and PI-AIMD within NpT ensemble 136
B.2 Decomposed x-ray spectra of liquid water based on local structure index 139

C.1 Comparison of O-O radial distribution functions from PI-DPMD and PI-AIMD within NVT ensemble 141
C.2 Polarized hydration structures of chloride ion 143
C.3 Coordination number in the first hydration shell of chloride solution 144
C.4 O-Cl-O angular distribution functions in chloride solution 145
C.5 H-Cl-H angular distribution functions in chloride solution modeled by PBE functional at 363K 146

D.1 Convergence test of VBM and CMB calculations 152

LIST OF TABLES

3.1 Water monomer vibration frequencies 34

4.1 Peak positions of O-O, O-H and H-H radial distribution functions in liquid water 57

7.1 Peak positions of quasiparticle density of state in chloride solution . 105

C.1 Peak positions of Cl-O and Cl-H radial distribution functions in chloride solution 142

C.2 H-bond count in chloride solution 145

CHAPTER 1

INTRODUCTION

Water is one of the most important materials and has enormous impacts on life. Despite the simplicity of a three atoms molecule, water shows various anomalous properties in its condensed phases, such as its density maximum at 4 ° C and its complex phase diagram, which has not been fully understand. The complexity of water mostly originates from the delicate Hydrogen bond (H-bond) network. In this nearly tetrahedral structure, water molecules on neighboring sites are attracted by highly directional H-bonds, which constantly break and reform on the timescale of picosecond due to thermal fluctuations at ambient conditions. Not surprisingly, the fundamental understanding of liquid water properties is at the center of scientific interests. Various advanced experimental methods, such as scattering experiments and various spectroscopy techniques, have been developed and applied to study the nature of H-bond in liquid water. On the other hand, *ab initio* molecular dynamics (AIMD) has been widely adopted as an important theoretical tool to provide microscopic information of water on a sub-picosecond timescale. Recent AIMD studies based on the strongly constrained and appropri-

ately normed (SCAN) exchange correlation functional yield an excellent description of the structural, electronic, and dynamic properties of liquid water. This provides one a reliable way to model and study various physical properties of the aqueous systems.

In this dissertation, we will focus on using AIMD with potential energy surface provided by the novel SCAN functional to study the structural, electronic and dynamic properties of liquid water as well as the modeling of the hydration structures of ions in aqueous solutions. Our results in this dissertation provide one with the following important views: First, we confirm the reliability of our model by representing an accurately predicted infrared spectrum of liquid water and connecting these improvements to the better description of the underlying H-bond network. Second, we address the importance of quantum effects on the light weighted hydrogen atoms by adopting the Feynman path-integral (PI) method. And we show that a force field model based on artificial neural network is capable to qualitatively capture the isotope effect of liquid water compared to neutron scattering experiments and x-ray absorption experiments. Third, we systematically present the necessity of including NQEs of the hydrogen atom when modeling chloride ionic solution. A prominent structural changes can be identified when NQEs are taken into consideration. Following is the outline of the rest of this dissertation.

In Chapter 2, we present some background knowledge included in this dissertation. First, a brief introduction of density functional theory and AIMD is given. Second, we provide some necessary information about water molecules and H-bond network in liquid water. At last, we discuss about the history of modeling liquid water systems by AIMD.

In Chapter 3, we study the infrared spectrum of water within the canonical ensemble, based on the liquid structures modeled by AIMD by using maximally localized Wannier functions as basis. In particular, we employ both Perdew-Burke-Ernzerhof (PBE) functional within generalized gradient approximation (GGA) and the state-of-art meta-GGA level approximation provided SCAN functional. We demonstrate that the SCAN functional improves not only the water structure but also the theoretical infrared spectrum of water. Our analyses in this chapter show that the improvement in the stretching and bending bands can be mainly attributed to the better descriptions of directional H-bonding and the covalency at the inter- and intra-molecular levels, respectively. On the other hand, the better agreements in libration and hindered translation bands are due to the improved dynamics of the H-bond network enabled by a softer liquid structure towards the experimental direction. Overall, the predicted spectrum by SCAN shows a much better agreement with experimental data compared to the conventionally widely adopted PBE functional at the GGA level.

In Chapter 4, we employ Feynman path-integral deep potential molecular dynamics (PI-DPMD) calculations to study both light (H_2O) and heavy water (D_2O) within the isothermal–isobaric ensemble, where the deep neural network is trained based on *ab initio* data obtained from the SCAN exchange-correlation functional. As the lighter mass of hydrogen than deuteron, the properties of light water are more influenced by nuclear quantum effect than those of heavy water. We identify clear isotope effects in terms of hydrogen-bond structure and electronic properties of water that are closely associated with experimental observables. The molecular structures of both liquid H_2O and D_2O agree well with the data extracted from

scattering experiments. And the delicate isotope effects on radial distribution functions and angular distribution functions are well reproduced. Our approach demonstrates that deep neural network combined with SCAN functional based AIMD provides an accurate theoretical tool for modeling water and its isotope effects.

In Chapter 5, we study the isotope effects in x-ray absorption spectra of liquid water by a many-body approach within electron-hole excitation theory. The molecular structures of both light and heavy water are modeled by model as discussed in previous Chapter. The experimentally observed isotope effect in x-ray absorption spectra is reproduced semiquantitatively in theory. We show that, as compared to the spectrum in light water, the blueshifted and less pronounced pre- and main-edge in heavy water reflect that the heavy water is more structured at short- and intermediate-range of the hydrogen-bond network. In contrast, the isotope effect on the spectrum is negligible at post-edge, which is consistent with the identical long-range ordering in both liquids as observed in the diffraction experiments.

In Chapter 6, we employ PI-AIMD calculations to probe the nature of solvation of chloride ion in aqueous solution. NQEs are shown to weaken hydrogen bonding between the chloride anion and the solvation shell of water molecules. As a consequence, the disruptive effect of the anion on the solvent water structure is significantly reduced compared to what is found in the absence of NQEs. The chloride hydration structure obtained from PI-AIMD agrees well with information extracted from neutron scattering data. In particular, the observed satellite peak in the hydrogen-chloride-hydrogen triple angular distribution serves as a clear sig-

nature of NQEs. Our results suggest that NQEs are likely to play a crucial role in determining the structure of saline solutions.

In Chapter 7, we theoretically predict the energetics of a solvated chloride anion and liquid water based on many-body perturbation theory at the static G_0W_0 level, where the ionic solution is modeled as discussed in Chapter 6. The electronic structure results in energetics are in excellent agreement with experiment. In particular, we find that the good agreement between the computed density of states and experimental photoelectron spectra is largely due to the NQEs that effectively weaken the interaction between the Cl- anion and its hydration shells. This result confirms that NQEs are important in order to accurately predict the electronic structure of the aqueous solvation of ions of the Hofmeister series.

CHAPTER 2

BACKGROUND

In this first part of this chapter, we give some brief reviews of the theoretical framework that is utilized throughout this work. Since theory itself is not the object of this dissertation, only basic concepts will be discussed in this chapter, without touching the complex mathematical derivation of these theorem. In the second part, we give some introduction about properties of water molecules and liquid water as well as a brief overview of modeling liquid water with *ab inito* molecular dynamics.

2.1 Theoretical background

2.1.1 Born-Oppenheimer approximation

Systems of man-body condensed matter physics usually contain a combination of both nuclei and electrons. In principle, one can describe the status of the system with a combined Hamiltonian for N_e electrons and N_n nuclei,

$$\hat{H} = [\hat{T}_n + \hat{T}_e + \hat{U}_{ee}(\vec{r}) + \hat{U}_{nn}(\vec{R}) + \hat{U}_{en}]. \tag{2.1}$$

The Born-Oppenheimer (BO) approximation recognizes the large mass difference between the nuclear and electron, including the difference in the time scale of nuclear motions and electronic motions. The BO approximation rationalizes the approach which treats the electrons and nuclei part separately , where the former instantly follow the movement of the latter [Born and Oppenheimer, 1927]. Mathematically, the BO process can be simplified as an expression of the total wave function as the product of electronic term and nuclear term,

$$\Psi(\vec{r}, \vec{R}, t) \approx \psi_e(\vec{r}, \vec{R})\psi_n(\vec{R}, t), \tag{2.2}$$

where $\psi_n(\vec{R}, t)$ is the nuclear wave function, $\psi_e(\vec{r}, \vec{R})$ is the electronic wave function that depends on the nuclear positions, and the cross terms are ignored. As a result, the static electronic Schrodinger's equation

$$\hat{H}_e\psi_e(\vec{r}, \vec{R}) = E_e\psi_e(\vec{r}, \vec{R}) \tag{2.3}$$

and the Schrodinger's equation for the nuclear motion (time dependent)

$$[\hat{T}_n + E_e]\psi_n(\vec{R}, t) = i\hbar\frac{\partial}{\partial t}\psi_n(\vec{R}, t) \tag{2.4}$$

can be treated and solved separately. Note that the BO approximation stands well in our target system, that is liquid water.

2.1.2 The Hohenberg-Kohn theorem

In order to solve for physical properties, such as total energy and band gap, of a N-electron system, the most intuitions way is to utilize the Schrodinger's equation with N-electron wave function $\psi(\vec{r_1}, \vec{r_2}, ..., \vec{r_N})$. However, since all electrons are coupled with each other, one can only get analytical solutions for the simplest

systems. As number of electrons N increases, the computational cost increase exponentially. It is almost impossible to solve a system with a large N. To address this issue, Thomas and Fermi independently bring out a model that assumes that the total energy of a given system can be described as a function of the electron density in the late 1920s, which takes the form:

$$\begin{aligned} E(n(\vec{r})) &= T(n) + U_{eN}(n) + U_{ee}(n) \\ &= C_k \int n(\vec{r})^{\frac{5}{3}} d\vec{r} + \int n(\vec{r}) V(\vec{r}) d\vec{r} + \frac{1}{2} \int \int \frac{n(\vec{r}) n(\vec{r}')}{|\vec{r} - \vec{r}'|} d\vec{r} d\vec{r}' \end{aligned} . \tag{2.5}$$

Due to the fact that such model ignores Pauli exclusion principle and the correlation between electrons, the Thomas-Fermi theory is very limited in accuracy. This method only works fine for simple metals and has been shown to give poor predictions in atomic and molecular systems.

Inspired by Thomas-Fermi theory,Thomas-Fermi theory, Hohenberg and Kohn brought up and proved two fundamental theorems in 1964 [Hohenberg and Kohn, 1964], which later became the cornerstone of the density functional theory (DFT) [Sholl and Steckel, 2009]. The first theorem states that: *The ground-state energy from Schrodinger's equation is a unique functional of the electron density* $n(\vec{r})$. This theorem indicates a one-to-one correspondence between the ground-state wave functions and the ground-state election density. That is to say, all properties of a N-electron system, including but not limited to energy wave functions, can be uniquely determined by the ground-state electron density through a functional. The second theorem is: *The electron density that minimizes the energy of the universal functional* $F[n]$ *is the true electron density corresponding to the full solution of the Schrodinger equation.* Based on this theorem, the energy of the

N-electrons system can be written as,

$$E[n] = \int v(\vec{r})n(\vec{r})d\vec{r} + \frac{1}{2}\int\int \frac{n(\vec{r})n(\vec{r}')}{|\vec{r}-\vec{r}'|}d\vec{r}d\vec{r}' + F[n]. \tag{2.6}$$

If the exact form of the universal functional is known, one can solve for the ground-state of any given N-electrons system by the minimization of the energy functional of the three-dimensional density function $E[n]$ throughout variational method under the restriction $N[n] \equiv \int n(\vec{r})d\vec{r} = N$. Unfortunately, these two theorems do not explicitly give the form of universal functional $F[n]$.

2.1.3 The Kohn-Sham equation

Soon after the publication of the Hohenberg-Kohn theorem, Kohn and Sham proposed an approximation for the universal functional of the density [Kohn and Sham, 1965]. They expressed the universal functional as

$$F[n] \equiv T_s[n] + E_{xc}[n], \tag{2.7}$$

where $T_s[n]$ is the kinetic energy of a fictitious system of non-interacting electrons with electron density $n(\vec{r})$ and $E_{xc}[n]$ is the exchange-correlation energy of an interacting system with density $n(\vec{r})$. The expression to approximate the exchange-correlation energy is another important topic in DFT and will be discussed later in section 2.1.4.

By the Kohn-Sham method, one can find the exact ground-state energy $E_{KS}[n(\vec{r})]$ as a function of the electron density of a fictitious system. The system includes N non-interacting electrons who see an effective potential $V_{eff}(\vec{r})$ and have the same density $n(\vec{r})$ as the real interactive electrons'. The ground-state energy takes the

form:

$$E_{KS}[n] = \int d^3r v(\vec{r})n(\vec{r}) + U[n] + T_s[n] + E_{xc}[n], \tag{2.8}$$

where $v(\vec{r})$ is the external potential of nuclei, $U[n]$ is the Hartree electron interact energy:

$$U[n] = \frac{1}{2}\int d^3r \int d^3r \frac{n(\vec{r})n(\vec{r})}{|\vec{r} - \vec{r'}|}, \tag{2.9}$$

$T_s[n]$ is non-interacting Kinetic energy:

$$T_s[n] = \frac{1}{2}\sum_{\alpha=1}^{N} \int d^3r \phi_a^*(\vec{r})(-\frac{1}{2}\nabla^2)\phi_a(\vec{r}), \tag{2.10}$$

and $E_{xc}[n]$ is the approximated exchange-correlation energy . The electron density is defined by:

$$\begin{aligned} n(\vec{r}) &= N \int d^3r_1 d^3r_2 \ldots d^3r_N |\psi(\vec{r_1}, \vec{r_2}, ..., \vec{r_N})|^2 \\ &= \sum_{\alpha=1}^{N} |\phi_\alpha(\vec{r})|^2, \end{aligned} \tag{2.11}$$

where $\psi(\vec{r_1}, \vec{r_2}, ..., \vec{r_N})$ is the wave function of the real electrons and $\phi_\alpha(\vec{r})$ are wave functions of the fictitious non-interacting electrons.

In order to obtain $n(\vec{r})$, one can address the non-interacting orbitals $\phi_a(\vec{r})$ first, by solving the one-particle Schrodinger equation like Kohn-Sham equation:

$$[-\frac{1}{2}\nabla^2 + v_{eff}(\vec{r})]\phi_a(\vec{r}) = \epsilon_a \phi_a(\vec{r}) \tag{2.12}$$

where

$$v_{eff}(\vec{r}) = v(\vec{r}) + v_H(\vec{r}) + v_{xc}([n], \vec{r}) \tag{2.13}$$

The first term of $v_{eff}(\vec{r})$ is the external ionic potential,

$$v(\vec{r}) = \sum_I \frac{Z_I}{|\vec{R}_I - \vec{r}|}, \tag{2.14}$$

that defines the interaction between electrons and the atomic nuclei. The second term is the Hartree potential

$$v_H(\vec{r}) = \frac{\delta U[n]}{\delta n(\vec{r})} = \int d^3r \frac{n(\vec{r})}{|\vec{r} - \vec{r}'|}, \tag{2.15}$$

which describes the Coulomb repulsion between electrons. As the electron density is calculated based on all electrons, this term will lead to a self-interaction where the electron will have Coulomb interactions with itself. This nonphysical interaction and other energy shift due to the non-interacting electron approach can be corrected by a proper model of the last potential term v_{xc}. It defines the exchange-correlation contributions the chemical potential of the fictitious single electron system, and can be calculated based on the functional derivation of E_{xc},

$$v_{xc} = \frac{\delta E_{xc}}{\delta n(\vec{r})}. \tag{2.16}$$

It is worth mentioning that the eigenvalues ϵ_a and eigenstates $\phi_a(\vec{r})$ of the Kohn-Sham equation are constructed mathematically. In principle, the physical meanings of ϵ_a and $\phi_a(\vec{r})$ are not well defined. The sum of the Kohn-Sham eigenvalues should not be directly treated as the total energy of the system.

With the Kohn-Sham equation, one can solve a N-electron system self-consistently. The self-consistent iteration to solve a system can be summarized as follows:

i) Begin with an initial guess for the single electron wave functions.

ii) Use equation 2.11 to calculate the electron density $n(\vec{r})$ based on the single electron wave functions.

iii) Use equation 2.13 to calculate the KS potential $V_{eff}([n], \vec{r})$ from $n(\vec{r})$.

iv) Solve the KS equation 2.12 and get the single electron wave functions $\phi_\alpha(\vec{r})$.

v) Check the convergence. If the preset convergence threshold is achieved, then stop. Otherwise, go back to step ii and repeat.

vi) Calculate physical properties with the obtained wave functions, such as position, nuclear motion, or classical force $\vec{F_\alpha} = -\frac{\partial E}{\partial \vec{R}_\alpha}$

2.1.4 Exchange-correlation functionals

So far, we have demonstrated an outline of solving a N-electron system with the Kohn-Sham method. To solve the Kohn-Sham equations, one need the specific the form of the exchange-correlation function E_{xc}. However, the exact definition of E_{xc} still remains unknown. In the following content, we will show some commonly used approximations of E_{xc} in DFT.

Local Density Approximation (LDA)

Along with the Kohn-Sham equation, Kohn-Sham proposed an approximation of treating the $E_{xc}(\vec{r})$ [Kohn and Sham, 1965]. For a inhomogeneous system, where $n(\vec{r})$ varies slowly, one can treat the local exchange-correlation potential as the exchange-correlation potential in homogeneous electron gas with the same electron density. With this approximation the exchange-correlation energy can be written as

$$E_{xc}[n] = \int n(\vec{r})\epsilon_{xc}[n(\vec{r})]d\vec{r}, \tag{2.17}$$

where $\epsilon_{xc}[n(\vec{r})]$ is the exchange-correlation energy per electron of a uniform electron gas with density n. Furthermore, one can always treat the exchange term and correlation term independently $\epsilon_{xc}[n(\vec{r})] = \epsilon_x[n(\vec{r})] + \epsilon_c[n(\vec{r})]$. As uniform electron

gas is a well studied system [Dirac, 1930], its exchange term can be described as

$$\epsilon_x(n) = -\frac{3}{4}(\frac{3}{\pi})^{\frac{1}{3}} n^{\frac{1}{3}}. \tag{2.18}$$

The correlation term, however, needs to be carefully treated to amend the aforementioned self interaction error. And the analytical form of correlation term was proposed by Perdew and Zunger in the 1980s [Perdew and Zunger, 1981].

With the local density approximation, the variation of the exchange-correlation energy can be written as

$$\delta E_{xc}[n] = \int [\epsilon_{xc}^{LDA}[n] + n\frac{\partial \epsilon_{xc}^{LDA}[n]}{\partial n}] d\vec{r}\delta n, \tag{2.19}$$

and the correspond exchange-correlation potential is

$$v_{xc}^{LDA}[n] = \epsilon_{xc}^{LDA}[n] + n\frac{\partial \epsilon_{xc}^{LDA}[n]}{\partial n}, \tag{2.20}$$

which can be used in the self-consistent iteration of solving the Kohn-Sham equation.

Generalized gradient approximation (GGA)

For systems, where electron density varies fast in space, the LDA will not stand. A natural thought is to include higher order terms of electron density to capture the fast variation of the exchange-correlation energy. Similar to LDA, GGA models the local exchange-correlation energy as a function of the local electron density $n(\vec{r})$ as well as the gradient of local electron density $\nabla n(\vec{r})$,

$$E_{xc}[n] = \int n(\vec{r})\epsilon_{xc}[n(\vec{r}), \nabla n(\vec{r})] d\vec{r}. \tag{2.21}$$

Moreover, the dependence of density gradient $\nabla n(\vec{r})$ is often achieved by adding a enhancement factor F_{XC} based on the LDA, that is

$$E_{xc}[n] = \int n(\vec{r})\epsilon_{xc}^{LDA}[n(\vec{r})] F_{XC}[n(\vec{r}), \nabla n(\vec{r})] d\vec{r}. \tag{2.22}$$

Intensive studies have been focusing on the field which leads to a wide pool of existing GGA functionals, such as the BLYP [Becke, 1988; Lee et al., 1988] and the PBE [Perdew et al., 1996a, 1997] functional. During last decades, the GGA level functionals is the most widely adopted exchange-correlation functionals and have been used in the modeling of varieties of systems.

meta GGA

Following the similar approach, higher accuracy in modeling exchange-correlation energy can be achieved by taking more density related information into account as a variable of ϵ_{xc}. By adding second order gradient Δn and (or) orbitial kinetic energy densities $\tau = \sum_i |\nabla \phi_i|^2$, one can obtain higher level meta-GGAs exchange-correlation functionals, such as the TPSS [Tao et al., 2003] and SCAN [Sun et al., 2015] functional, where

$$E_{xc}[n] = \int n(\vec{r})\epsilon_{xc}[n(\vec{r}), \nabla n(\vec{r}), \Delta n, \tau] d\vec{r}. \tag{2.23}$$

As will be shown later, SCAN functional has a great performance in capturing covalent bond, hydrogen-bond, as well as including inter-medium range dispersion [Sun et al., 2016]. As a result, we adopt the SCAN functional in most of the studies in this dissertation.

Hybrid functional

Based on the "adiabatic connection" formula, that "connect" the non-interacting Kohn-Sham system to the interacting real physical system, Becke showed the general frame work of the hybrid theory [Becke, 1993b]. Generally, hybrid functional takes the form of mixing exchange energy from Hatree-Fock (HF) theory [Hartree

and Hartree, 1935] and exchange-correlation energy from DFT,

$$E_{xc}^{hyb} = E_{xc}^{DFT} + a_0(E_x^{HF} - E_x^{DFT}). \tag{2.24}$$

Particularly, in the case of PBE0 [Perdew et al., 1996b], a 25% mixing rate is adopted. The study shows that the hybrid functionals PBE0 improves the accuracy of predicting molecular properties like binding energy. Furthermore, as the exact exchange energy is expressed as a function of Kohn-Sham orbitals instead of the electron density, the calculation of hybrid functionals tends to increase the calculation burden by a considerable amount.

2.1.5 *Ab initio* molecular dynamics

Under the framework of BO approximation, one would investigate movements of nuclei after obtaining proper treatments of the static electronic system. In this section, we will focus on modeling the dynamics of nuclei with the instantaneous ground state of electronic captured by DFT [Tuckerman, 2002].

Classical nuclei approximation

Recall from equation 2.1 and 2.4, the motions of nuclei on the ground electronic surface are described by

$$[\hat{T}_n + \hat{U}_{nn} + E_e]\psi_n(\vec{R}, t) = i\hbar\frac{\partial}{\partial t}\psi_n(\vec{R}, t) \tag{2.25}$$

Due to the large mass, the wave function of the nuclei tends to be very localized in real-space. As a result, the nuclei are usually treated as classical particles by taking the form

$$\psi_n(\vec{R}, t) = A(\vec{R}, t)e^{iS(\vec{R},t)/\hbar}. \tag{2.26}$$

This will result in the classical Hamiltonian-Jacobi equation

$$\sum_{I}^{N_n} \frac{\vec{P}_I^2}{2M_I} + U_{nn}(\vec{R}) + E_e(\vec{R}) + \frac{\partial S}{\partial t} = 0. \tag{2.27}$$

The equation of motion can be calculated by

$$\dot{\vec{R}}_I = \frac{P_I}{M_I}$$

$$\dot{\vec{P}}_I = -\nabla_I (U_{nn}(\vec{R}) + E_e(\vec{R})).$$

According to the Hellman-Feynman theorem [Feynman, 1939], the second term in the lower equation can be expressed based on the ground state of electronic wave functions as

$$\nabla_I E_e(\vec{R}) = \langle \psi_e(\vec{R}) | \nabla_I H_e(\vec{R}) | \psi_e(\vec{R}) \rangle, \tag{2.28}$$

which can be calculated on the fly by adopting the DFT approach. In practical applications, Verlet algorithm [Verlet, 1967]

$$\vec{R}_I(t + \Delta t) = 2\vec{R}_I(t) + R_I(t - \Delta t) + \frac{\Delta t^2}{M_I} \vec{F}_I \tag{2.29}$$

is often adopted to propagate the nuclear coordinates with error on the order of Δt^4.

With the aforementioned approach, one can solve the time-dependent Schrodinger equation of physical system of the N_e electron and N_n nuclei within the BO scheme. First, one can calculate the ground state electronic structure for the initial nuclear coordinates with DFT. Then, the nuclear coordinates can be updated by the Verlet algorithm. And one can follow the above two processes to study the time evolution of the whole system. Such algorithm is known as the Born-Oppenheimer molecular dynamics (BOMD). As BOMD requires updating the ground state of electronic structures for each molecular step, it is a very computational cost consuming method.

Car-Parrinello (CP) algorithm

To reduce the requirement of computational cost, one can use the unified Car-Parrinello approach to propagate the electronic and nuclear degrees of freedom at the same time [Car and Parrinello, 1985]. This is accomplished by introducing a fictitious dynamics for electrons via defining orbital 'velocities' $\dot{\phi}_i$ and a fictitious electron 'mass' parameter μ. The fictitious orbital 'kinetic energy' can be expressed as

$$T_{orbital} = \mu \sum_i \langle \dot{\phi}_i | \dot{\phi}_i \rangle. \tag{2.30}$$

The orbital movements can be adding into a extended dynamical system with the Lagrangian

$$L = \mu \sum_i \langle \dot{\phi}_i | \dot{\phi}_i \rangle + \frac{1}{2} \sum_I M_I \dot{\vec{R}}_I^2 - E_e[\phi, \vec{R}] - U_{nn}(\vec{R}) + \sum_{i,j} \Lambda_{ij} (\langle \phi_i | \phi_j \rangle - \delta_{ij}), \tag{2.31}$$

where Λ_{ij} is a set of Lagrange multipliers to ensure the orthonormal condition of CP orbitals and $\langle \phi_i | \phi_j \rangle = \delta_{ij}$ is satisfied as a constraint along the trajectory. Based on the Euler-Lagrange equation, the equations of motion of the extended system can be expressed as

$$\begin{aligned} M_I \ddot{\vec{R}}_I^2 &= -\nabla_I E[\phi, \vec{R}] \\ \mu | \ddot{\phi}_i \rangle &= \frac{\partial E[\phi, \vec{R}]}{\langle \phi_i |} + \Lambda_{ij} | \phi_j \rangle, \end{aligned} \tag{2.32}$$

where $E[\phi, \vec{R}] = U_{nn}(\vec{R}) + E_e[\phi, \vec{R}]$, which can be used to calculate the dynamics of the system. The above discussions give a brief picture of the CP algorithm. We stop the discussion here without providing further details. Although the CP approach remains influential, calculations based on BOMD are now widely used, due to the growth of the computational power in recent years.

Path integral (PI) method

For the systems with light nuclei, such as hydrogen atoms, it might be necessary to address the quantum motion of the light nuclei. This can be addressed by the Feynman path integral method [Feynman and Hibbs, 1965]. The general idea of PI method is to replace the quantum partition function of distinguishable particles with a classical partition function [Ceriotti et al., 2010b, 2016]. For simplicity, we take the canonical ensemble as an example. In the canonical ensemble the partition function can be written as

$$Z = \int d\vec{R} \langle \vec{R} | e^{-\beta \hat{H}} | \vec{R} \rangle. \tag{2.33}$$

For any given value of n, one can re-express the partition function by

$$Z = \frac{1}{n} \int \prod_{i=1}^{n} d\vec{R}_i \langle \vec{R}_i | e^{-\tau \hat{H}} | \vec{R} \rangle, \tag{2.34}$$

where $\tau = \beta/n$. Even though this expression is exact, one need to approximate the quantum Hamiltonian $\hat{H}$ in practical applications. At any given approximation of $\hat{H}$, the computed quantum value will converge in the limit when $tau \to 0$.

The most commonly used approximation is based on the second-order Trotter expansion

$$e^{-\tau \hat{H}} \approx [e^{-\frac{1}{2}\tau \hat{U}} e^{-\tau \hat{T}} e^{-\frac{1}{2}\tau \hat{U}}], \tag{2.35}$$

with the error of order τ^2. Such approximation leads to a classical Hamiltonian of n copies of the system, where the corresponding atoms are connected with harmonic spring, which is also known as ‘ring polymer‘. The Hamiltonian of the jth copies is expressed as

$$H_j(\vec{R}, \vec{P}) = U_j^0(\vec{R}, \vec{P}) + U(\vec{R}, \vec{P}), \tag{2.36}$$

where

$$U_j^0(\vec{R},\vec{P}) = \sum_i^{3N_n}(\frac{Pi^2}{2M_i} + \frac{1}{2}M_i\omega^2[R_i^{(j)} - R_i^{(j-1)}]^2) \tag{2.37}$$

is the Hamiltonian of an harmonic oscillator with $\omega = 1/\tau\hbar$, and $U(\vec{R},\vec{P})$ is the external potential felt by nuclei. This enables one to sample the quantum partition function with a classical manner with molecular dynamics (PIMD).

Similar algorithms as used in the classical nuclei approximation, such as Ring polymer molecular dynamics (RPMD) [Craig and Manolopoulos, 2004; Habershon et al., 2013] and centriod dynamics (CMD) [Cao and Voth, 1994; Jang and Voth, 1999] , can be adopted to model the time evolution of the system. For most of work in this dissertation, we adopt the RPMD approach. With RPMD, one splits the Hamiltonian into a free ring polymer part and a external potential part as shown in equation 2.36. Because the time evolution of the first part can be easily done with the normal mode representation of the harmonic oscillator, it is a natural thought to propagate the two parts separately. The procedure of RPMD can be describe as follows: First, one propagates the system under the influence of the external Hamiltonian for $\Delta t/2$ interval. Second, one transforms the system from bead representation to the normal mode representation by a orthogonal transformation. Third, one calculates the exact time evolution of the system for Δt under the ring polymer Hamiltonian. Fourth, one transforms the system back to bead representation. Fifth, one propagates the system under the influence of the external Hamiltonian for another $\Delta t/2$ interval.

Thermostats

In the above discussions, we propagate the system without energy exchanges, that is the microcanonical ensemble, where the number of particles N, the volume V and the total energy are constant (NVE). On one hand, one may want to compare the MD result with experimental observations, which typically occurs with a constant temperature T in the canonical ensemble (NVT) or even with a constant pressure in the isothermal-isobaric ensemble (NpT). On the other hand, one expects to accelerate the exploration of the possible configurations in the phase space without bias during the MD simulation. The above issue can be addressed by applying thermostats during MD. One of the most wide adopted thermostats is proposed by Nose and hoover [Nosé, 1984; Hoover, 1985]. In Nose's work, the model of time evolution in NVT ensemble are achieved by construct a extended Hamiltonian including a time-scale variable s, its conjugate momentum p_s and a fictitious mass Q,

$$H = \Phi(\vec{q}) + \sum_I \frac{\vec{p_I}^2}{2M_I s^2} + \frac{p_s^2}{2Q} + gkTlns. \tag{2.38}$$

Nose have proved that this microcanonical distribution with the augmented set of variable is equivalent to describe variables $q, p/s$ in the canonical ensemble [Nosé, 1984]. Hoover updated the concept by defining the thermodynamic friction coefficient $\zeta \equiv p_s/Q$ and redefining $p \equiv m\dot{q}$ [Hoover, 1985], then equations of motion of the system can be expressed as

$$\begin{aligned} \dot{q} &= p/m \\ \dot{p} &= F - \zeta p \\ \dot{\zeta} &= [\sum p^2/m - XkT]/Q, \end{aligned} \tag{2.39}$$

where F is the external force and X is the degrees of freedom of the system. Noting that Hoover also showed that by introducing the reduce coordinates $x \equiv q/V^{\frac{1}{D}}$, the 'external pressure' P_{ext} and the relaxation time τ, the method applied to describing the isothermal-isobaric ensemble for D dimensional system.

2.2 Water in liquid phase

In the previous section, we have shown an introduction to the theoretical background of this dissertation. Next, we will briefly introduce the target system: liquid water to the reader.

2.2.1 Properties of liquid water

Water molecule

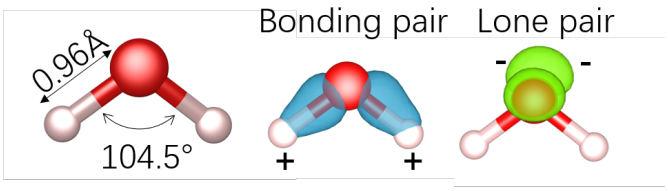

Figure 2.1: Atoms and electron pairs of a water molecule

The atomic composition of water was first established thorough the experiments of Cavendish and Lavoisier in the 1780s. Since then, extensive studies have been done/worked on analysis structural, energetic information of water molecules [Eisenberg and Kauzmann, 2005]. Nowadays, one knows that water molecule is a polarized molecules consist of 2 hydrogen atoms and 1 oxygen atoms with 2 covalent bonds as shown in Figure 2.1. It is symmetric with two mirror planes

and a 2-fold rotation axis (point group C_{2v}) Also, it has 4 valence electron pairs. Two of them locate along the covalent bond between the hydrogen and oxygen atom, which are bonding pairs. The other two, that locate at the opposite side of oxygen atom, are called the lone pairs.

Hydrogen bond

Despite its simple structure as a three-atom molecule, water is of great complexity in its condensed phase, where the electropositive site near hydrogen atom and the electronegative site close to oxygen atom tend to attract each other and forms hydrogen bond (H-bond), whose energy is around 10 kJ/mol, about one order weaker then the covalent bond.

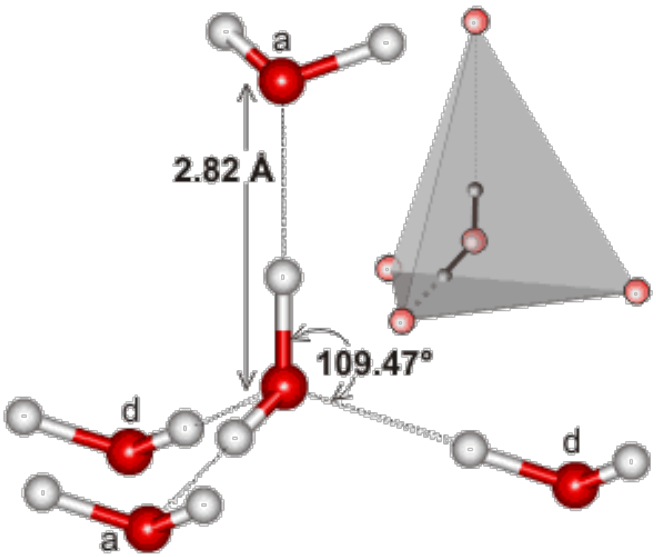

Figure 2.2: Schematic diagram for tetrahedral structure of H-bond. Figure is extracted online from http://www1.lsbu.ac.uk/water/water_hydrogen_bonding.html

Typically, in hexagonal ice, each water molecule both donate (where its hydrogen atom point to oxygen atom in other water molecule) and accept (where its oxygen atom is pointed by hydrogen atom in other water molecule) two H-bonds. These H-bonds forms tetrahedral structures as show in Figure 2.2. In the

case of liquid water, these H-bonds constantly breaks and reform under thermal fluctuations at the time scale of picoseconds [Zhang et al., 2011a]. With a fraction of water molecules have broken H-bonds, liquid water tends to form a more disordered structures. Some of the weakened H-bonded water molecules are able to occupied the interstitial region of the tetrahedral network, which increase the density of liquid water as compared to ice.

Structural parameters

To capture and describe characteristics of the disordered structure of liquid water, various of structural parameters have been used. H-bond statistics, such as the averaged donate (accept) H-bond numbers of a water molecule, are often used to evaluate the strength of H-bond [Chen et al., 2017; Zheng et al., 2018]. Tetrahedral order parameters [Chau and Hardwick, 1998], defined by angles (or distance) between a water molecule and its four nearest neighbors

$$\begin{aligned} q_{angle} &= \frac{3}{32}\sum_{i=1}^{3}\sum_{j=k+1}^{4}(\cos\theta_i j + \frac{1}{3})^2 \\ q_{distance} &= \frac{1}{3}\sum_{i=1}^{4}\frac{(r_i - \bar{r})^2}{4\bar{r}^2}, \end{aligned} \tag{2.40}$$

are often used to probe the local disorders of the H-bond network. Other local order parameters such as local structure index LSI, local density ρ, triple oxygen angular distributions $\mathrm{P_{OOO}}(\theta)$[Duboué-Dijon and Laage, 2015] are also widely adopted in the field.

The overall structures of liquid water are often modeled by the radial distribution functions (RDF), which is defined by the probability of finding a particle particle pair AB with relation $\vec{r}$ as shown in Figure 2.3 (a),

$$g_{\mathrm{AB}}(\vec{r}) = V\frac{\mathrm{d}P_{\mathrm{AB}}(\vec{r})}{\mathrm{d}\vec{r}}. \tag{2.41}$$

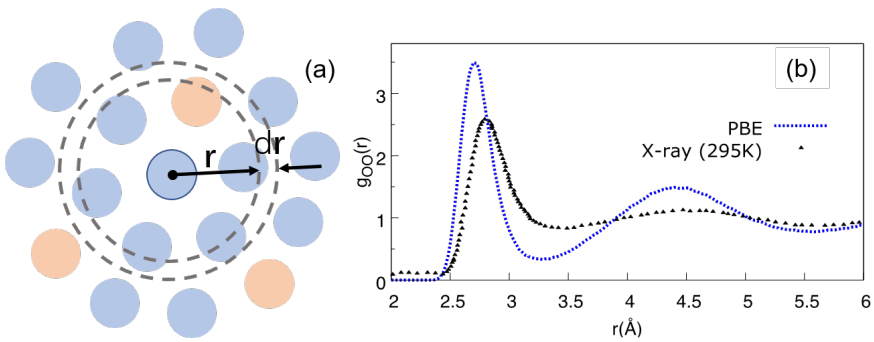

Figure 2.3: (a) Schematic diagram for the definition of radial distribution functions. (b) Example of O-O radial distribution functions

The angular contributions of RDF are often integrated out due to its isotropic property in liquid water. As a result, in *ab initio* molecular dynamic studies, RDFs of liquid water are often evaluated by

$$g_{\mathrm{AB}}(r) = \frac{1}{4\pi r^2 \rho} \frac{\mathrm{d}n_{\mathrm{AB}}(r)}{\mathrm{d}r}, \tag{2.42}$$

where n_{AB} is the averaged number within r and $r + \mathrm{d}r$, ρ is the overall density. Furthermore, RDF can be evaluated through structure factor $S(q)$, which is an observable from scattering experiments. Figure 2.3 (b) shows a comparison between the O-O RDFs either calculated from *ab initio* molecular dynamic simulations or derived from scattering experiment [Skinner et al., 2013]. Noting that the value of $g(r)$ indicates the correlation between given atom pairs. A homogeneous system will have $g(r) = 1$.

2.2.2 Modeling of liquid water

Liquid water as one of the most important chemical substances on earth has significant impacts on various chemical and biological processes [Franks, 2007; Ball, 2008; Bellissent-Funel et al., 2016]. Fundamental experimental and theoretical studies on the structure of water have been at the center of scientific interests for

decades [Stillinger, 1980; Luzar and Chandler, 1996; Fecko et al., 2003; Pettersson et al., 2016; Nilsson and Pettersson, 2015; Thämer et al., 2015; Kim et al., 2017; Chen et al., 2018; Soper, 2019].

In experiment, various advanced techniques, such as x-ray and neutron diffraction [Soper, 2013; Skinner et al., 2013], infrared and Raman spectroscopy [Brubach et al., 2005; Auer et al., 2007], x-ray absorption and photoemission spectroscopy [Fransson et al., 2016; Winter and Faubel, 2006], have been employed to study liquid water. X-ray and neutron diffraction experiments are widely adopted to probe the time-averaged structural information of liquid water. Combined with post-processing techniques, such as the empirical potential structure refinement (EPSR) method [Soper, 2001, 2005], the diffraction cross section data can be converted to commonly used structural properties, i.e. the radial distribution functions (RDFs) and angular distribution functions (ADFs). The infrared and Raman spectroscopy are used to probe vibration modes and dynamics of water [Brubach et al., 2005; Auer et al., 2007]. Whereas the x-ray absorption and photoemission spectroscopy provide electronic structure information, which is directly related to local bonding configurations at molecular scale [Fransson et al., 2016; Winter and Faubel, 2006]. However, the interpretation of experimental results in terms of structure is not straightforward and may induce artificial errors [Ceriotti et al., 2016], making *ab initio* molecular dynamics (AIMD) [Car and Parrinello, 1985] simulation an important theoretical tool to provide microscopic structural information of water on a sub-picosecond time scale. In AIMD, the forces acting on atoms are generated "on the fly" by the instantaneous first-principle based electronic ground state of the atomic structure without any empirical input. AIMD

can be used to predict structural, electronic, and dynamic properties of a given system at certain thermodynamic conditions. Since the early simulation of water in the 1990s [Laasonen et al., 1992; Tuckerman et al., 1995], AIMD has become an ideal approach to explore various chemical and biological aqueous systems.

In AIMD simulations, density functional theory (DFT) [Hohenberg and Kohn, 1964; Kohn and Sham, 1965] is adopted to calculate the potential energy surface (PES) at each time step due to a reasonable balance between accuracy and computational cost. Even though DFT is an exact theory in principle, the practical form of exchange-correlation (XC) functional requires approximations. Different levels of approximations for the XC term have been developed to increase the predictive power of DFT, including the local density approximation (LDA), generalized gradient approximation (GGA), meta-GGA, and hybrid functionals [Perdew, 2001]. Early studies on water clusters [Laasonen et al., 1992, 1993a] showed that the LDA approximation overestimates H-bond strengths and leads to excessive short distances between water molecules. The widely adopted GGA-level XC functionals, such as Perdew-Burke-Ernzerhof (PBE) [Perdew et al., 1996a,a], improve the structure of water, but still yield discrepancies with experimental observations [Gillan et al., 2016]. The remaining problems of GGA functionals can be summarized in two key points. For one, conventional XC functionals at the GGA level do not capture intermediate- and long-range non-local van der Waals (vdW) interactions [Hermann et al., 2017], which have been proved to be crucial for the correct prediction of water density [Gaiduk et al., 2015]. Secondly, the well-known self-interaction error [Perdew and Zunger, 1981] of GGA functionals leads to the delocalization of protons in liquid water, which increases the stiffness of H-bond ar-

tificially. The above drawbacks can be largely compensated by mixing a fraction of the exact exchange and adding vdW corrections [Miceli et al., 2015; Wiktor et al., 2017]. For example, studies adopting PBE0 hybrid functional and Tkatchenko Scheffler [Tkatchenko and Scheffler, 2009] dispersion corrections (PBE0+TS) have shown improved covalent bond vibration frequencies and less overstructured RDF and ADF distributions [DiStasio et al., 2014; Ko et al., 2019]. However, the application of such AIMD method depends semi-empirical treatments of vdW corrections and the hybrid functional requires a significant amount of computational cost. The strongly constrained and appropriately normed (SCAN) meta-GGA functional [Sun et al., 2015], which satisfies all 17 known exact constraints on the semilocal XC functional and includes intermediate-range vdW interactions, is a viable option to address the above issues. Recent works have proved that the SCAN functional provides accurate descriptions of O-H covalent bond and H-bonding strength as well as dynamical properties in water clusters, liquid water, and ice with the level of accuracy comparable to vdW inclusive hybrid functional [Sun et al., 2016; Chen et al., 2017; Zheng et al., 2018; Xu et al., 2019; Sharkas et al., 2020]. Moreover the computational cost of SCAN functional is marginally higher than GGA but about an order of magnitude less than hybrid functionals when applied to condensed phases [Furness et al., 2020].

CHAPTER 3

INFRARED SPECTRUM OF LIQUID WATER

3.1 Introduction

As stated in the introduction, advanced experimental methods, such as scattering [Soper, 2013; Skinner et al., 2013] and spectroscopy [Fransson et al., 2016] techniques, have been developed and applied to detect the nature of H-bond in water. In particular, the infrared (IR) spectroscopy provides a unique probe, in which both molecular configuration and its dynamics dielectric response can be inferred from the measured spectra [Brubach et al., 2005; Auer et al., 2007]. In the IR spectrum, four main spectral features have been identified in experiments. Located in the relatively higher frequency range, the stretching and the bending bands can be traced back to the molecular vibrations in water vapor, which are strongly modified due to the presence of H-bond network in condensed phase. On the other hand, the libration and the hindered translational bands with lower fre-

quencies originate from the collective motion of water molecules in the H-bonded network. Therefore, such vibrations have no counterparts in a single molecule.

Ab initio molecular dynamics (AIMD) simulation provides an ideal theoretical framework to study the IR spectra in water from first principles [Car and Parrinello, 1985]. In AIMD simulations, water structures can be modeled by AIMD trajectories at finite temperatures, in which the forces acting on nuclei are obtained by the electronic ground state determined by the density functional theory (DFT) [Hohenberg and Kohn, 1964; Kohn and Sham, 1965]. The direct calculation of IR spectrum is allowed by the advent of modern theory of polarization given by the Berry phase formulation for extended systems [King-Smith and Vanderbilt, 1993]. The detailed dynamics dipolar correlation and its dependence on the H-bond network were further revealed later [Sharma et al., 2005], The above were facilitated by a rigorous decomposition of overall polarization onto the electric dipoles belonging to individual water molecules based on maximally-localized Wannier functions (MLWFs) [Marzari et al., 2012].

Despite the above progress, difficulties remain when the computed IR is compared with available experiments. It is recognized that the accuracy of the predicted water structure depends on the level of adopted exchange-correlation functional in DFT. For the simulations of water, the GGA [Perdew et al., 1996a] is widely applied. However, the GGA functional significantly overestimates the H-bonding strength as well as the polarizability of water, which is evidenced by the large red shift ($\sim$200 cm^{-1}) [Sharma et al., 2005; Chen et al., 2008] of the computed stretching band compared to the experimental data. The above deficiency is partially due to the inherited self-interaction error. As a result, one electron

state applies a spurious electrostatic interaction on itself [Perdew and Zunger, 1981]. By mixing a fraction of exact exchange, recent simulations showed that the underestimated stretching band in IR spectra of water can be largely improved by the PBE0-based AIMD simulation [Zhang et al., 2011a]. However, the application of hybrid DFT based AIMD demands significantly increased computational cost. Due to this reason, the available AIMD trajectories were relatively short, and the statistics was limited. Moreover, all the conventional functional approximations at the GGA level lack the description of long-range van der Waals (vdW) interactions. The long-range vdW is the key physical factor behind the larger mass density of water than that of ice [Zhang et al., 2011b; Chen et al., 2017]. Even in the canonical (NVT) ensemble, where the density of water is fixed to the experimental value at ambient conditions, the vdW inclusive AIMD simulation was found to have large effects on the water structure, which can be seen by the enhanced population of water molecules in the interstitial region [Schmidt et al., 2009b; Hermann et al., 2017]. It is accepted that the long-range vdW interaction has relatively small effect on the directional H-bonding. However, water molecules in the interstitial region are expected to be weakly bonded or non-bonded. So far, it is unclear whether or not the increased fluctuation of water molecules in the interstitial region will affect the overall IR spectra in a nontrivial way. Clearly, an improved modeling of the water structure and its dynamics via the DFT approach is prerequisite to answer the above questions.

To address the above issues, we compute the IR spectrum of water from a systematically improved modeling of liquid water by the SCAN [Sun et al., 2015] meta-GGA functional. The IR spectrum computed from the conventional PBE-

GGA [Perdew et al., 1996a] AIMD trajectory is also presented here for comparison. By satisfying all the seventeen known exact constraints on the semi-local functional, the recently developed SCAN functional presented a greatly improved description in both covalency in water cluster [Sun et al., 2016] and H-bond network in liquid water and ice [Chen et al., 2017; Zheng et al., 2018]. Consistently, our computed IR spectrum based on SCAN-AIMD shows a significant improvement over the entire spectral range compared to the spectrum generated from conventional PBE-GGA functional. The red frequency shift and overestimated amplitude of the stretching band obtained with the PBE-GGA functional are largely corrected by the improved directional H-bonding strength. By using the MLWFs as basis, the increased population of water molecules in the interstitial region is found to be anticorrelated which partially contributes to the decreased spectral amplitude towards the measured IR spectrum. The better agreement of the bending band frequency can be mainly attributed to the improved description of covalency of water molecules. On the other hand, the blue shift of the libration modes towards the experimental direction is correlated to the improved prediction of dynamical property in water.

3.2 Methods to compute infrared spectra in liquid water

We computed the IR spectra of liquid water based on trajectories from Car-Parrinello molecular dynamics [Car and Parrinello, 1985] using the Quantum Espresso package [Giannozzi et al., 2017]. The PBE and SCAN exchange-correlation

functionals were used. Norm-conserving pseudopotentials [Hamann, 2013] were adopted with an energy cutoff of 85 Ry. All simulations were carried out in a periodically cubic box with side lengths of 23.57 Bohr (12.47 Å), and 64 D_2O molecules were included in the box. The time step was set to 2 a.u. (∼0.048 fs), with electron mass as 100 a.u.. The temperature was set to 330 K and the Nosé-Hoover thermostat [Nosé, 1984; Hoover, 1985] was adopted with the canonical ensemble. All simulations were run for more than 50 ps. In addition, we carried out ground-state DFT calculations for water monomer in a cubic box with cell lengths being 30 Bohr (15.88 Å), using both SCAN and PBE with an energy cutoff of 250 Ry, to calculate the vibrational frequencies.

The IR spectra of liquid water are computed based on the IR absorption rate in terms of the total dipole moment (dipole approximation). The formula [McQuarrie, 2000] is derived using the Fermi's golden rule and Poynting vector with a classical approach [Bader and Berne, 1994] applied, where we treat the quantum time correlation function classically:

$$\alpha(\omega)n(\omega) = \frac{2\pi\beta\omega^2}{3cV}\int_{-\infty}^{+\infty} dt e^{-i\omega t}\langle M(0)M(t)\rangle \tag{3.1}$$

where $\alpha(\omega)$ is the light absorption coefficient per unit depth as a funcition of the frequency ω, $n(\omega)$ is the refractive index, $\beta = (k_B T)^{-1}$ with k_B and T being the Boltzmann factor and temperature, respectively. The total dipole moment M in the simulation cell is computed via the formula: $\sum_{i=1}^{n} \mu_i$, where the molecular dipole moment of the ith water molecule μ_i can be calculated via the position of nuclei and corresponding Wannier centers. Furthermore, we adopted a gaussian window [Harris, 1978] in the form of $e^{-t^2/2\alpha^2}$ with $\alpha = 0.5$ ps, when the discrete Fourier transform in Eq. 3.1 is performed.

3.3 Simulated infrared spectra

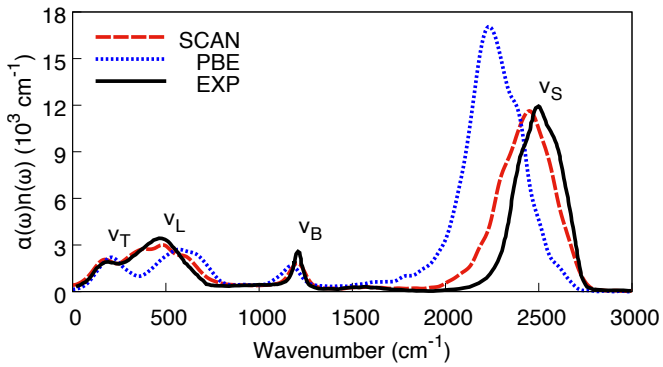

Figure 3.1: IR spectra of liquid water obtained from AIMD simulations in the NVT ensembles. The experimental data [Max and Chapados, 2009] are at room temperature. Labels ν_T, ν_L, ν_B, and ν_S correspond to translation, libration, DOD bending, and OD stretching peaks, respectively.

As shown in Figure 3.1, we present the theoretical IR spectra generated by SCAN-AIMD and PBE-AIMD trajectories. For comparison, the experimental spectrum is also shown. Four main dipole correlated vibrational bands can be identified in Figure 3.1, whose characteristics belong to the hindered translation (T), libration (L), deuterium-oxygen-deuterium (DOD) bending (B), and the oxygen-deuterium (OD) stretching (S) modes with increasing frequencies. The IR spectrum computed from SCAN-AIMD shows a significantly improved accuracy comparable to that computed with the hybrid DFT functional [Zhang et al., 2011a], in which the better agreement with the experiment can be seen in both the spectral positions and spectral shape. The peaks of the above four bands, calculated by SCAN-AIMD, are centered at ν_T=172 (186) cm^{-1}, ν_L=483 (486) cm^{-1}, ν_B=1207 (1209) cm^{-1}, ν_S=2448 (2498) cm^{-1}. In comparison, the same bands obtained from PBE-AIMD are predicted to be centered at ν_T=207 (186) cm^{-1}, ν_L=572 (486) cm^{-1}, ν_B=1174 (1209) cm^{-1}, and ν_S=2233 (2498) cm^{-1} re-

spectively. In the above, the values presented in the parenthesis are taken from experiment [Max and Chapados, 2009]. In particular, the improvement by SCAN in the positions of the liberation and stretching modes is significant, which can be seen by the frequency shift of ∼100 and ∼200 cm^{-1} respectively. At the same time, the spectral shape is also largely improved towards the experimental direction as clearly evidenced by the reduced intensity in the stretching band over 30%, which is severely overestimated at the PBE level.

3.3.1 Stretching modes

The OD stretching band originates from the molecular vibrations in water vapor (gas) phase. Based on the C_{2v} point group symmetry of water monomer, these vibrations can be further categorized as symmetric and anti-symmetric eigen modes with a slightly higher frequency of the later in experiments. Under the development of stretching modes, the covalent bond is elongated with a tendency towards dissociation, which also directly modifies the electric dipole of water molecules. Not surprisingly, the stretching band in the IR spectra not only locates at the highest frequency range but also has the most prominent spectral intensity among the four IR spectral features. At the PBE level, the frequencies of both symmetric and anti-symmetric modes in gas phase are underestimated over

Table 3.1: Water monomer (D_2O) vibration frequencies in cm^{-1}. (Subscripts b,ss, and as stand for bending, symmetric stretching, and anti-symmetric stretching modes, respectively.)

Methods	ν_b	ν_{ss}	ν_{as}
SCAN	1193	2710	2832
PBE	1162	2660	2770
EXP [Benedict et al., 1956]	1206	2784	2889

∼4% compared to experiment as shown in Table 3.1, which is consistent with the previous calculations [Zhang et al., 2011a]. Compared to PBE, the SCAN functional predicts better stretching frequencies in water gas phase with improvement of ∼2% towards experiment as shown in Table 3.1. The above can be attributed to the improved prediction of covalency in water monomer. Indeed, the better agreement with experiments by SCAN functional in terms of bond angle, bong length, and binding energies in single water molecule and water clusters in gas phase have been widely recognized recently [Sun et al., 2016; Zheng et al., 2018].

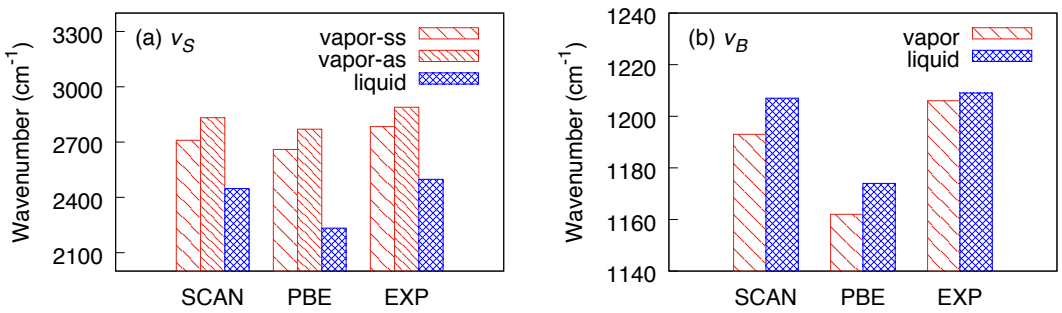

Figure 3.2: (a) Stretching frequency ν_S and (b) bending frequency ν_B of single water molecule (vapor) and liquid water as compared using SCAN, PBE, and experiment data (EXP) of vapor [Benedict et al., 1956] and liquid water [Max and Chapados, 2009]. (Note that symmetric stretching frequency ν_{ss} and anti-symmetric stretching frequency ν_{as} are listed separately for water vapor.)

In the liquid phase, the difference between symmetric and anti-symmetric modes is smeared by the disordered environment and the stretching band is formed. Moreover, the H-bond, represented by the weak attraction of a proton to the oxygen lone pair of the neighboring molecules, also facilitates the elongation of OH bonds as shown by the red shift of the stretching vibration by ∼300 cm^{-1} in liquid compared to the corresponding vibration in vapor phase as measured experimentally in Figure 3.2 (a). However, due to the significant overestimation of the H-bond strength by PBE functional, the stretching frequency of liquid water

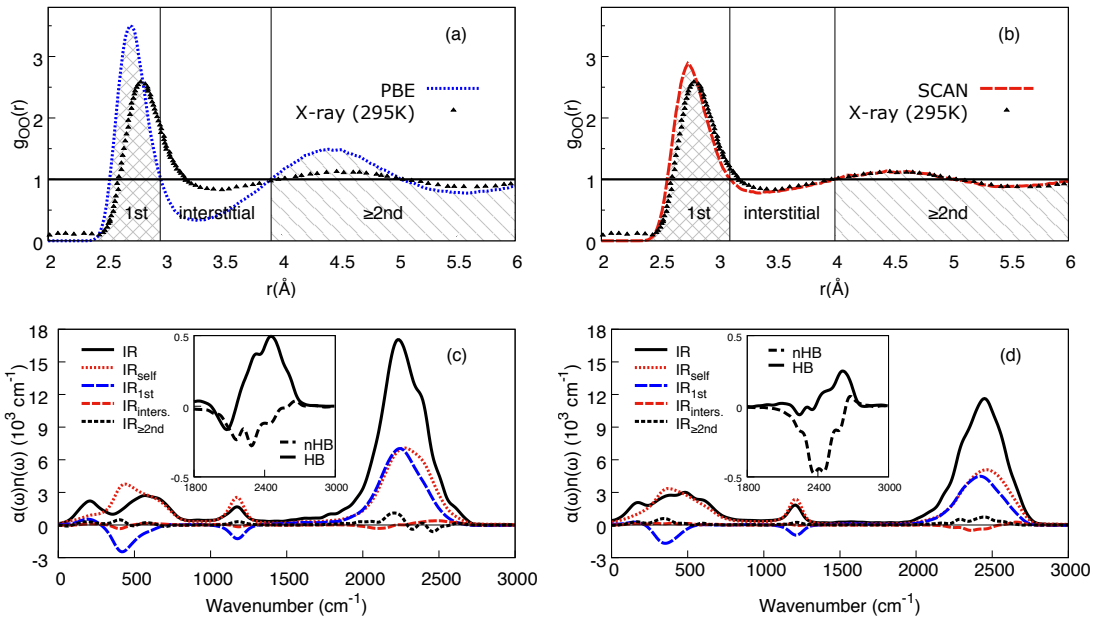

Figure 3.3: Oxygen-oxygen pair distribution functions and the corresponding spacial decompositions by (a) PBE and (b) SCAN functionals compared with X-ray diffraction experiment [Skinner et al., 2013]. Intramolecular IR_{self} (red dotted lines) and spacial intermolecular IR_{1st} $IR_{inters.}$, and $IR_{\geq 2nd}$ (colored dashed lines) contributions to the calculated IR spectra (black solid lines) using (c) PBE and (d) SCAN in the NVT ensemble. Decompositions of $IR_{inters.}$ into non H-bonded (dashed lines) and H-bonded (solid lines) water contributions are shown as insets in (c) and (d).

is predicted to be ∼500 cm^{-1} lower than that of water in vapor phase. The artificially strengthened H-bond by PBE also leads to the overestimated dipole-dipole correlation in the H-bond network as evidenced by the much greater IR spectral intensity than the experimental spectrum in Figure 3.1. In sharp contrast, the IR spectrum computed by SCAN functional shows a significantly better agreement in the above aspects. We attribute this improvement to the more accurate H-bond structure as well as dynamical correlation described by SCAN functional.

In order to elucidate the spectral signatures of liquid structure, we further decompose the overall spectrum into contributions from different ranges in the H-bond network. Based on the method introduced by Chen et al. [Chen et al., 2008], the total dipole correlation function in the temporal domain of Eq.(3.1) can

be rewritten as the sum of a correlation function of any pair of water molecules as $\langle M(0)M(t)\rangle(r_1, r_2) = \langle \sum_{i,j} \mu_i(0)\mu_j(t)\rangle$. In the above, the electronic and ionic contributions of dipole moment μ_i and μ_j of water molecules at any time t are rigorously determined by the Wannier centers and the ionic coordinates respectively, both of which are generated on the fly in the AIMD simulation. Therefore, the spectrum can be divided into intramolecular $\mathrm{IR_{self}}$ $(i = j)$ and intermolecular $(i \neq j)$ parts [Sharma et al., 2005]. In current work, we further divide the intermolecular part into spectral contributions from the first coordination shell $\mathrm{IR_{1st}}$, water in the interstitial region $\mathrm{IR_{inters.}}$, and water from the second shell and beyond $\mathrm{IR_{\geq 2nd}}$[1], respectively based on the distance r_{ij} between the molecule pairs as illustrated in Figure 3.3 (a) and (b). The criterion for interstitial region is chosen to be 3.10 Å $\leq r_{ij} <$ 4.00 Å in SCAN and 2.96 Å $\leq r_{ij} <$ 3.91 Å in PBE, where the oxygen-oxygen pair distribution function $\mathrm{g_{OO}}(r)$ is less than 1 between the first and second peaks. In the decomposition, water molecules are considered as H-bonded if the O-O distance is less than 3.5 Å and the OOD angle is less than 30°[Luzar and Chandler, 1996]. The resulting spectral decompositions and the corresponding $\mathrm{g_{OO}}(r)$ are shown in Figure 3.3 for both PBE and SCAN functionals.

Dynamically, the stretching mode not only modifies the electric dipole of the water molecule under vibration, but also strongly polarizes the surrounding water molecules via the H-bonds. Therefore, the stretching band of IR spectrum is dominated by both $\mathrm{IR_{self}}$ and $\mathrm{IR_{1st}}$ contributions. Such effect has been well captured by both SCAN and PBE functionals which can be seen by the large and

[1]In order to sample the angular distribution uniformly while calculating the IR spectra of second shell and beyond region. We apply an upper limit of the correlated distance as half of the box length.

comparable intensities from these two decompositions. In the above, the IR_{self} has a slightly higher frequency than that of IR_{1st}. It is not surprising since the IR_{1st} is more sensible to the H-bond network, while the IR_{self} is instead more affected by the intrinsic vibration of water monomer. However, the IR spectrum from PBE functional suffers from clear drawbacks. Compared to the experimental measurement, the $g_{OO}(r)$ is significantly over-structured with a shorter first peak position than experimental measurement, indicating the overestimated H-bond strength, as shown in Figure 3.3 (a). As a result, the stretching band of IR spectrum computed at the PBE level is centered at a much lower frequency of 2233 cm^{-1} with a much higher intensity in comparison to experimental measurements. It is consistent with the fact that PBE predicts the proton to be more delocalized and easier to be donated to the neighboring water molecules than it should be. Such a severely overestimated directional H-bond strength is largely improved by SCAN functional, which can be seen by the less structured coordination shell and increased distance of the first peak in $g_{OO}(r)$, as shown in Figure 3.3 (b). The softer H-bond network towards the experimental direction also generates a less polarizable liquid water, as indicated by the predicted average electric dipole by SCAN (2.95 $\pm$ 0.28 D) being much closer to the experimental reference (2.9 $\pm$ 0.6 D) [Badyal et al., 2000] than that of PBE (3.22 $\pm$ 0.29 D). As expected, the stretching mode in the less polarizable medium becomes harder and shifts the stretching band center to a higher frequency at 2448 cm^{-1} as well as reduces intensities mainly from both IR_{self} and IR_{1st}.

The dynamical polar correlation from stretching vibration decays rather rapidly for water molecules separated by a distance further away from the first coordina-

tion shell, which are qualitatively similar for both PBE and SCAN predictions as shown in Figs. 3.3 (c)(d). Indeed, it is consistent with the weaker structural correlations in the radial distribution $g_{OO}(r)$ beyond the first peak in Figs. 3.3 (a)(b). However, the drawbacks can be still identified due to the over-structured liquid water by PBE functional. On the one hand, the spectral contribution from water in the second shell and beyond $IR_{\geq 2nd}$ is predicted to have a higher intensity in PBE than that from SCAN. On the other hand, due to the artificially strengthened H-bond strength, most water molecules in the interstitial region are still H-bonded to the central molecule under stretching motion, giving rise to the positively spectral intensity in the insert of Figure 3.3 (c). However, the opposite trend is observed in the prediction by SCAN functional, in which the water molecules in the interstitial region are mostly non-bounded with the observed anti-correlation as seen by the negative spectral intensity in the insert of Figure 3.3 (d). It should be noted that the increasingly populated water molecules in the interstitial region should be attributed to the intermediate range vdW interactions captured by SCAN function, which is found to be the key physical effect in predicting a higher mass density of water than that of ice [Chen et al., 2017]. With the weaker dipole correlations from water molecules beyond the first coordination shell that correctly predicted by SCAN functional, the overestimated IR spectral intensity by PBE is further reduced towards the experimental direction.

3.3.2 Bending mode

Among the four spectral features, the bending band has the second largest frequency centered at around 1200 cm^{-1}, which originates from the bending mode of

water monomer. Under the bending mode, the DOD bonding angle is modulated, which in turn changes the electric dipole of the molecule, but with a much weaker coupling strength than stretching mode. Not surprisingly, the resulting spectral intensity is also smaller than the stretching band. In vapor phase, the frequency of the bending mode is underestimated by ∼4% at PBE level, while the calculation by SCAN functional gives rise to a much more accurate value with an error of ∼1% compared to experiment at 1206 cm^{-1} in Table 3.1 and Figure 3.2 (b). Clearly, such a significant improvement should be again attributed to the better description of the covalency by SCAN. Indeed, the bonding angle and bonding length of water monomer are respectively found to be 104.4° (104.5°) and 0.961 Å (0.957 Å) by SCAN, showing a large improvement over the PBE functional of 104.2° and 0.970 Å as compared to the experimental values in the parenthesis [Sun et al., 2016].

In condensed phase, the bending band instead of discrete levels is formed by the disordered liquid structure. According to the spectral decompositions in Figs. 3.3 (c)(d), the bending band is mainly contributed by the intramolecular contribution and the first coordination shell. In particular, the water molecules in the first coordination shell provide a large negative spectral intensity resulting from its anti-correlation in nature. It is not surprising since the protons under bending mode move along the normal direction of H-bond. Therefore, the development of bending vibration needs to overcome the energy to break the H-bond and generate out-of-phase dynamical dipole correlation [Chen et al., 2008]. As a result, unlike the stretch band, the presence of H-bond network in liquid water impedes the bending mode resulting in a slightly increased frequency relatively to that in

water vapor in experiment. Such a feature has been qualitatively predicted in both PBE and SCAN functionals. Clearly, the frequency difference is still overestimated by roughly the similar magnitude for both functionals. The deficiency is likely due to the self-interaction error inherited in both GGA and meta-GGA functionals resulting in the delocalized protons that are more easily to be donated to neighboring oxygen atom.

3.3.3 Far-infrared modes

In the far-infrared region in Figure 3.1, the two spectral features in a rather broad distribution are associated with the collective vibrations on the H-bond network, which emerge in the condensed phases such as ice and water. The feature at the higher frequency branch around $\sim$500 cm^{-1} is attributed to the libration mode. Depicted by water libration, the water molecules undergo hindered rotational motions restricted by the presence of H-bond network. Therefore, such spectral signal is absent in the water vapor since it is free to rotate an isolated molecule. Like the bending motion, water molecules under libration also needs to overcome the energy barrier by breaking H-bonds. Consistently, the spectral decomposition from intramolecular and first coordination contributions are dominant, in which the latter is characterized by the anti-correlation with negative spectral intensities as shown in Figs. 3.3 (c)(d). Because of the over-structured H-bond network, the frequency of the libration motion is exaggerated $\sim$20% by PBE functional, centered at 572 cm^{-1}. The softer liquid structure modeled by the SCAN functional eases the water libration at 483 cm^{-1}, matching accurately the experimental data at 486 cm^{-1}. Because the direction of water polarity aligns

along HOH angular bisector, the hindered water rotation is also highly associated with dynamical properties such as the rotational diffusion constant and rotational relaxation time which is accessible to experiments. The relaxation time τ_n is obtained by fitting with $e^{-t/\tau}$ to the nth order rotational correlation functions, which are defined by the time correlation function $C_n(t) = \langle P_n[\hat{\boldsymbol{u}}(0)\hat{\boldsymbol{u}}(t)]\rangle$. Here P_n is the nth Legendre polynomial and $\hat{\boldsymbol{u}}$ is the in plane unit vector along the symmetry axis of a water molecule. To this end, we compute the first order rotational correlation function $C_1(t)$ and the corresponding relaxation time τ_1 based on trajectories from both PBE and SCAN functionals as shown in Figure 3.4. It should be noted that features at the beginning of rotational correlation function around 0.066 and 0.062 ps, magnified in the inserts of Figure 3.4, are corresponding to the libration motion that have been observed in the frequency domain in Figure 3.3. As time passes, the rotational correlation decays in both trajectories giving rise to the relaxation time τ_1. Under the Debye's model, the relation between relaxation time τ_n and the rotational diffusion constant D_R takes the form of $\tau_n = 1/[n(n+1)D_R]$. In the above, the rotational diffusion constant D_R is given by the inverse of τ_1, which is measured to be 2.0-7.5 ps [Laage and Hynes, 2008]. Clearly, the over-structured water model by PBE functional hampers the rotation motion and predicts an unphysically long relaxation time τ_1=20.91($\pm$0.22) ps with the corresponding small rotational diffusion constant D_R=0.047 ps^{-1}. In sharp contrast, the softer water modeled by SCAN functional largely facilitates the water rotation and gives rise to much more reasonable values of τ_1=4.08($\pm$0.02) ps and D_R=0.24 ps^{-1}, respectively. The result consists with previous studies on diffusion coefficient[Zheng et al., 2018]. As a conclusion, the modified libration

peak from the SCAN functional indicates an improved description of the diffusion related dynamics in liquid water.

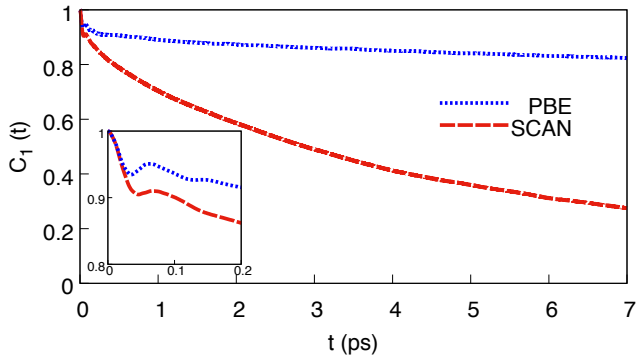

Figure 3.4: First order rotational correlation functions of liquid water obtained from AIMD simulations with SCAN (red dashed line) and PBE (blue dotted line) in the NVT ensembles. The inset shows enlarged rotational correlation functions in the first 0.2 ps.

In the gas phase, the water molecule is free to undergo a translation motion in space. In liquid, water molecules however undergo hindered translation constrained by the H-bond network, which is depicted by the lower branch feature of the far-infrared band centered at ∼200 cm^{-1} in Figure 3.1. Similar to the stretching mode, the spectral decomposition in Figure 3.3 shows that the IR signals are mainly contributed by the dynamical correlation from intramolecular contribution and molecules in the first coordination shell, which is consistent with the first-principles studies of Chen et al [Chen et al., 2008]. Unlike the stretching mode that is directly coupled to the electric dipole, the dynamical correlation here is generated by the induced dipole-dipole interaction under the hindered translation motion [Guillot, 1991]. Therefore, the intensities of hindered translation are much weaker than those in the stretching band as shown in Figure 3.3. Not surprisingly, the artificially overstructured liquid water predicted by PBE functional overestimates the energy barrier cost of hindered translation, which is evidenced by an

overestimated peak position at 207 cm^{-1}, compared to the experimental value of 186 cm^{-1}. On the other hand, the softer liquid structure model by SCAN functional facilitates the water translation with a slightly underestimated value of 172 cm^{-1}.

It is well accepted that the liquid water structure under PBE prediction is ice-like which is not only over structured but also sluggish that barely diffuses in space. As a result, the overall shape of the libration and hindered translation band is also ice like under the PBE prediction as shown in Figure 3.1. In the above, the distinction between the two modes is exaggerated by the rather deep minimum with a frequency gap around 370 cm^{-1}. Indeed, in the crystalline ice, the libration and hindered translation are two distinct spectral bands, which are separated completely with frequencies of 640 cm^{-1} and 222 cm^{-1} in experiment [Eisenberg and Kauzmann, 2005], respectively. Strikingly, the above ice-like error is mostly corrected in the spectrum modeled by SCAN functional. For a liquid water structure that is more softened and disordered towards the experimental direction, the distinction between libration and hindered translation is also smeared as shown in Figure 3.1.

3.4 Conclusion

In conclusion, we have performed careful and comparative first-principles molecular dynamics studies on the IR spectra of liquid water obtained by SCAN meta-GGA and PBE GGA functionals. Our results showed the SCAN meta-GGA functional provides significant improvements on all four peaks in the IR spectra, compared to those obtained by PBE. Our analysis demonstrate that the SCAN

functional models water more precisely on both molecular and liquid levels, and gives better descriptions of electronic structure, range dependent correlations, and dynamical properties. On one hand, SCAN reaches the accuracy level of the IR spectra obtained by PBE0 hybrid functional [Zhang et al., 2011a], with a relatively low computational cost. On the other hand, one may expect that the hybrid functional SCAN0 mitigates the self-interaction error in DFT, and brings the calculated IR spectra closer to the experiments. Furthermore, recent studies [Ceriotti et al., 2013; Sun et al., 2018; Hunter et al., 2018] suggested that nuclear quantum effects due to light protons play a crucial role in obtaining accurate liquid water properties. The role played by quantum nuclei awaits further investigation which is likely to broaden the spectral features and slightly reduce the frequencies of stretching band due to the delocalized protons.

CHAPTER 4

NUCLEAR QUANTUM EFFECTS AND ISOTOPE EFFECTS ON LIQUID WATER

4.1 Introduction

Due to the light mass of hydrogen atoms, nuclear quantum effects (NQEs) induce nontrivial impacts on the H-bond network [Morrone and Car, 2008; Ceriotti et al., 2016; Soper and Benmore, 2008]. NQEs are indispensable for any water model to have quantitative agreement with the experimental observations as well. Experimentally, NQEs can be identified in the water system by isotope substitution of hydrogen by deuterium. In the joint x-ray/neutron diffraction experiments by Soper *et al.* [Soper and Benmore, 2008], distinct isotope effects, such as covalent bond contractions from H_2O to D_2O, are observed. In AIMD simulations, quantum effects of nuclei can be included through the Feynman path-integral (PI)

method [Feynman and Hibbs, 1965]. Recent PI-AIMD simulations [Morrone and Car, 2008; Ceriotti et al., 2013; Ko et al., 2019; Cheng et al., 2019] show that NQEs altered the simulated structural properties by a considerable extent. Moreover, as the zero-point energy enables atoms to explore classically inaccessible regions of the PES, the structural changes caused by NQEs highly depend on the description of the underlying PES, i.e., the choice of XC functionals. Previous PI-AIMD studies employing various functionals [Marsalek and Markland, 2016; Gasparotto et al., 2016; Ko et al., 2019; Yao and Kanai, 2020; Zhang et al., 2020] show highly fluctuating results. Yao *et al.* [Yao and Kanai, 2020] studied the NQEs of liquid water using the SCAN functional in the canonical ensemble at different temperatures. They showed that the NQEs brought the OH and HH RDFs much closer to the experimental values but the OO RDFs changed very little from its classical counterpart.

Based on the proper treatment of NQEs, the isotope effects on liquid water is anther crucial topic that is worth stressing. light water (H_2O) and heavy water (D_2O) only differ slightly in the H-bond network [Soper and Benmore, 2008; Zeidler et al., 2012]; however, the former is essential for a living cell, while the latter can be harmful in many ways [Franks, 2007; Thomson, 2006; Kushner et al., 1999]. Moreover, minute distortions in the H-bond network can cause noticeable changes in functionalities of numerous biological processes occurring in aqueous environments [Fersht et al., 1985; Ohtaki and Radnai, 1993; Leberman and Soper, 1995; Tarek and Tobias, 2002; Chen et al., 2018]. Therefore, a precise picture of the isotope effect of liquid water is crucial, which also serves as an important milestone to accurately understand the intensely discussed microscopic structure

of water [Wernet et al., 2004; Nilsson et al., 2010; Tse et al., 2008; Smith et al., 2006; Nilsson and Pettersson, 2015; Fransson et al., 2016; Amann-Winkel et al., 2016; Smith and Saykally, 2017]. As such, a systematic study of isotope effects employing the state-of-the-art SCAN meta-GGA functional at ambient condition would be consequential on the path of the theoretical modeling of liquid water, which has not been fully addressed.

In PI-AIMD simulations, physical systems are represented by ring-polymers composed of several replicas (beads), which largely increase the computational costs. Even with advanced methods [Ceriotti et al., 2009b; Ceriotti and Manolopoulos, 2012] that reduce the required number of beads, the computational burden is still a vital issue that limits the application of PI-AIMD. The rise of machine-learning-based approaches, e.g., the deep potential molecular dynamics (DPMD) method [Zhang et al., 2018a], has enabled overcoming this computational barrier. With the DPMD method, one can train a deep neural network with a small amount of *ab initio* data and perform extensive molecular dynamics simulations for an extended system with a linear-scaling computational cost which is orders of magnitude cheaper than traditional AIMD. At the same time, DPMD is able to provide similar accuracy ($\sim$1 meV/molecule) as *ab initio* approaches for water systems [Zhang et al., 2018a]. The DPMD model has been used to study the isotope effect in liquid water with the PBE0+TS XC functional [Ko et al., 2019], where quantitative agreements with experiment is achieved.

In this chapter we focuses on studying NQEs and isotope effects in liquid water via DPMD and PI-DPMD based on the PES provided by the SCAN XC functional within the isothermal–isobaric (NpT) ensemble. With the inclusion of

NQEs, quantum fluctuations that can either strengthen or weaken the H-bond [Yao and Kanai, 2020; Li et al., 2011] are observed. Remarkable changes are illustrated in structural properties of liquid water such as RDFs, statistics of H-bond information, oxygen-oxygen-oxygen ADF, and local tetrahedrality. Besides, we present quantum effects on electronic properties such as the density of state and the distribution of dipole moments of liquid water. Both structural and electronic properties obtained from our simulations agree better with the experimental observations as a result of NQEs. Furthermore, isotope effects are well reproduced.

4.2 Methods

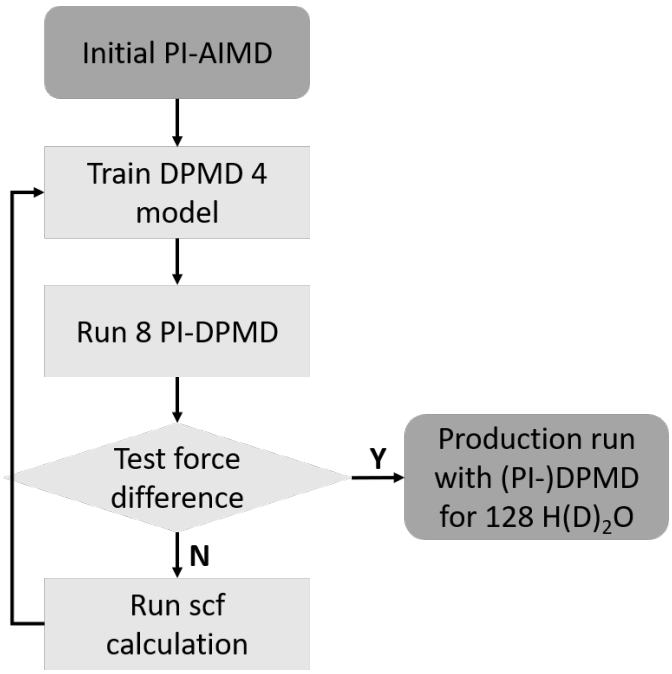

Figure 4.1: Flow diagram of DP-GEN active learning procedure

In order to generate an accurate neural network force field based on the SCAN functional, we adopted the active learning procedure called deep potential generator (DP-GEN) [Zhang et al., 2019]. The procedures are shown in Figure 4.1

and summarized as follows. First, a PI-AIMD simulation is performed to provide initial training data set for the DPMD model. Second, four independent DPMD models are trained based on the same training data set but different initialization of the deep potential parameters. Third, based on the trained DPMD models, eight separated PI-DPMD simulations are performed to explore the PES. Configurations, where the four independent DPMD models give diverse predictions, are marked as unexplored configurations. Fourth, we generate energies and forces from *ab initio* calculations for the selected configurations. Then, these newly generated data are added to the training data set and go back to the second step until the satisfactory accuracy is reached. The final DPMD model is used to generate the DPMD and PI-DPMD trajectories of liquid water.

For generating initial training data set, a Born-Oppenheimer Feynman path-integral [Feynman and Hibbs, 1965] AIMD simulation of a periodically replicated cubic box containing 64 H_2O molecules was performed within NpT ensemble at ambient conditions (300 K and 1.0 bar). The PES was calculated based on the SCAN meta-GGA functional [Sun et al., 2015] with the Quantum ESPRESSO (QE) package [Giannozzi et al., 2009, 2017]. Hamann-Schlüter-Chiang-Vanderbilt (HSCV) norm-conserving pseudopotentials [Vanderbilt, 1985] were used to model the core level electrons. Valence electrons were represented by a plane-wave basis (with a 130 Ry effective cutoff and a 12.66 Å reference cell) as implemented in the QE package. Only the gamma point was used to sample the Brillouin zone of the supercell. In PI-AIMD, the integration time step was set to 0.48 fs. An 8-bead ring-polymer with a colored-noise generalized Langevin equation thermostat [Ceriotti et al., 2009b; Ceriotti and Manolopoulos, 2012] was adopted to model

quantum nuclei using the i-PI package [Kapil et al., 2019]. To expand the region that light protons are able to explore on the PES, light water was adopted in the simulation. The simulation cell was propagated using the Parrinello-Rahman method [Parrinello and Rahman, 1980] and thermostatted by another colored noise Langevin thermostat with a fictitious mass consistent with a 200 fs timescale. The total length of our final PI-AIMD production run is over 10 ps. This provides a rough exploration for the PES of the SCAN functional.

Atomic coordination, energy (E), ionic force ($\boldsymbol{F}_i$), and stress tensor ($\boldsymbol{\Xi}$) were extracted from the PI-AIMD trajectory as the initial training data set. These data were used as the input PES data to train four independent DPMD models using the DeePMD-kit package [Wang et al., 2018] as described in Ref. [Zhang et al., 2018a]. First, the input data were transformed to a local coordinate frame $\{D_{ij}\}$ for each atom and its neighbors within 6 Å, in order to preserve the translational, rotational, and permutational symmetries of the system. Then $\{D_{ij}\}$ was used as input of a deep neural network (DNN), which includes five hidden layers with 240, 120, 60, 30, 10 nodes and returns the energy of atom i. During the training process, the Adam method [Kingma and Ba, 2014] was used to optimize the DNN parameters with a set of loss functions defined as:

$$L(p_\epsilon, p_f, p_\xi) = p_\epsilon \Delta\epsilon^2 + \frac{p_f}{3N}\sum_i |\Delta \boldsymbol{F}_i|^2 + \frac{p_\xi}{9}||\Delta\boldsymbol{\xi}||^2, \tag{4.1}$$

where N stands for the number of atoms, $\epsilon = E/N$, $\boldsymbol{\xi} = \boldsymbol{\Xi}/N$, and $\Delta\epsilon$, $\Delta\boldsymbol{F}_i$, $\Delta\boldsymbol{\xi}$ denote the difference between the input data and current DPMD predictions. p_ϵ, p_f, p_ξ are preset tunable parameters. For efficiency, p_ϵ, p_f, and p_ξ were adjusted from 0.02 to 8, 1000 to 1, and 0.02 to 8, respectively, throughout the training procedure, while the learning rate decayed exponentially. After training for 10^6

steps, we obtained four DPMD models. As the training data set may not cover the full PES, these four DPMD models will show different performances for unexplored configurations.

After obtaining the first generation of DPMD models, the DP-GEN iterations began. To further explore the PES, eight additional PI-DPMD simulations were performed using the DeePMD-kit and the i-PI packages. The driving force was provided by one of the four DPMD models. We adopted exactly the same i-PI parameters as used in the generation of the initial training data set and initialize the simulations from independent starting configurations. All trajectories lasted for around 1 ns. Along the PI-DPMD trajectories, all four DPMD models were used to predict forces. The differences between forces predicted by the four DPMD models were recorded for each configuration. Configurations with maximum force differences greater than 0.2 eV/Å were selected and marked as unexplored configurations. If the proportion of marked configurations along the trajectory is less than 1%, the four DPMD models were considered as converged. Otherwise, we performed self-consistent *ab initio* calculations using the QE package to calculate the ground state of the selected configurations. All related parameters were kept the same as the initial PI-AIMD simulation. *Ab initio* energies and forces were extracted and added to the training data set. Four new independent DPMD models were generated based on the updated training data set. Then, we repeated the PES exploration step. After 9 iterations, the DPMD model converged. The final DPMD model was tested to have a root mean square error of 0.6 meV/atom for energy prediction.

With the DPMD model, the simulation size was expanded to include 128 water

molecules in order to reduce the finite-size effects and optimize statistical sampling of the molecular dynamics trajectories. Three simulations adopting the DPMD model were presented in this work. First, a single classical DPMD simulation of liquid water within NpT ensemble at ambient conditions was performed using the combination of the DeePMD-kit and the LAMMPS package [Plimpton, 1995]. Nosé-hoover thermostat and barostat [Tuckerman et al., 2006] were used to control the temperature and pressure of the system. The integration time step was set to 0.5 fs. The resulting DPMD trajectory lasted for 5 ns. The other two PI-DPMD simulations of liquid H_2O and D_2O were performed adopting similar parameters as the training process. For heavy water, the nuclear mass of hydrogen was set to 2.01 u. The length of both PI-DPMD trajectories is 960 ps, which ensures that the computed properties are statistically converged. Moreover, in order to study electronic properties, *ab initio* level electron ground state as well as the Maximally localized Wannier Functions (MLWFs) [Marzari and Vanderbilt, 1997; Marzari et al., 2012] centers were computed for 4000 selected snapshots uniformly distributed along each trajectories using the QE package.

4.3 Proton transfer coordinates

Quantum fluctuations result in two competing effects that either strengthen or weaken the H-bond in liquid water [Ceriotti et al., 2016]. The proton fluctuations along the stretching direction of O-H covalent bond can facilitate H-bond formations. On the contrary, the fluctuations along proton libration direction, which are perpendicular to the H-bond, tend to weaken the H-bond network. The former effects dominate in relatively strong hydrogen bonds, whereas the latter

ones dominate in relatively weak hydrogen bonds [Li et al., 2011]. These two competing nuclear quantum effects are well captured by the SCAN functional as shown by the previous study [Yao and Kanai, 2020]. The overall NQEs depend on the delicate balance between the two opposite effects.

To illustrate fluctuations of protons under NQEs, we resort to the proton transfer coordinates ν, which is defined as $\nu = d(\mathrm{O_1\text{-}H}) - d(\mathrm{O_2\text{-}H})$, where $\mathrm{O_1}$ and H denote the oxygen (O) atom and any of the two hydrogen (H) atoms in one water molecule and $\mathrm{O_2}$ represents other oxygen atoms within the first coordination shell of the water molecule, as shown in the inset of Figure 4.2 [Ceriotti et al., 2013; Sun et al., 2018]. As defined, ν characterizes the location of H atoms between the two O atoms within two adjacent water molecules. For example, $\nu = 0$ means that the H atom is precisely in the middle of two O atoms. This configuration forms a strong H-bond and shows a high tendency to facilitate a proton transfer event. The distribution of proton transfer coordinate ν generally exhibits two peaks. The peak at lower ν (< -1.3) originates from H atoms that have $\mathrm{O_1}$-H covalent bond pointed away from $\mathrm{O_2}$. The other peak ($\nu > -1.3$) comes from the H atoms located in between $\mathrm{O_1}$ and $\mathrm{O_2}$, which are likely to form H-bond.

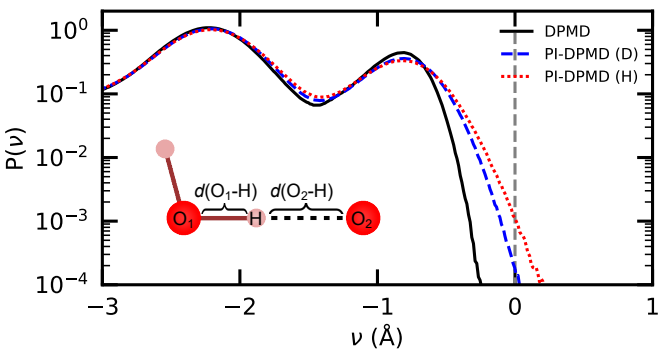

Figure 4.2: Log scale distribution of proton transfer coordinate ν of liquid water obtained from DPMD (black solid line), $\mathrm{D_2O}$ PI-DPMD (blue dashed line) and $\mathrm{H_2O}$ PI-DPMD (red dotted line) simulations. The inset shows the definition of $\nu = d(\mathrm{O_1\text{-}H}) - d(\mathrm{O_2\text{-}H})$.

The proton delocalization along the direction of the acceptor oxygen, which induces stronger hydrogen bonds, can be seen by the wider distribution of ν. Figure 4.2 shows that the distributions of ν become broader from classical DPMD to D_2O and H_2O PI-DPMD simulations. Moreover, a small amount of positive ν appears in both the PI-DPMD simulations, while only negative ν can be found in classical DPMD simulations. The positive ν is more pronounced in the light water than the heavy water. This is consistent with the finding in previous works [Ceriotti et al., 2013; Sun et al., 2018]. Under NQEs, the zero-point energy (ZPE) enables the proton to overcome potential barriers and explore configurations that are hard to access in classical simulations. As H_2O has larger ZPE than D_2O, light water shows over an order of magnitude more positive ν compared to heavy water in PI-DPMD simulations. It is worth mentioning that these extreme H-bond fluctuations only last on a time scale of femtoseconds and no proton transfer event is observed on the time scale of the entire simulation; a similar observation that has been reported by Ceriotti *et al.* [Ceriotti et al., 2013].

The proton delocalization along the libration direction, which weakens the hydrogen bonds, is revealed by the height of the H-bond peak and the position of the minimum between two peaks in Figure 4.2. In quantum simulations, the height of the H-bond peak is reduced from its classical counterpart by a larger extent than that of the none-bonded peak. Also, the position of the minimum between two peaks shifts to the right by about 0.04 Å. The isotope substitution from D_2O to H_2O shows a similar trend with less extent in regard to the peak changes. These facts indicate that more water molecules originally H-bonded to each other in classical simulations become non-bonded under the libration fluctuations caused

by NQEs.

As a summary, both kinds of quantum fluctuations, that can either facilitate or weaken the H-bond network in liquid water, have been observed through the comparison of PI-DPMD simulations with DPMD simulations. In the following sections, more properties will be discussed to determine how the above mentioned NQEs change the overall structure of liquid water.

4.4 Radial distribution functions

Radial distribution functions are widely adopted tools to study the structure of water, which show the probability to find a given atom pair as a function of distance in real space. In this section, O-O, O-H, and H-H RDFs from DPMD and PI-DPMD trajectories are shown in Figs. 4.3, 4.4, and 4.5. For comparison, the EPSR data based on joint x-ray and neutron diffraction experiments by Soper *et al.* [Soper and Benmore, 2008] are plotted as well. The positions of maxima and minima of $g_{\mathrm{OO}}(r)$, $g_{\mathrm{OH}}(r)$, and $g_{\mathrm{HH}}(r)$ obtained from the simulations and experimental measurements are summarized in Table 4.1. In general, one observes broadening effects in all O-O, O-H, and H-H RDFs when NQEs are included through the path-integral method. PI-DPMD simulations slightly soften water structures and yield better agreements with the experimental data as compared to the classical DPMD simulation. Moreover, the RDFs show that D_2O is slightly more structured than H_2O due to the weaker zero-point motions. The differences between the RDF of H_2O and that of D_2O qualitatively agree with experimental results, indicating that the experimentally observed delicate isotope effects are reproduced by our PI-DPMD simulations.

Table 4.1: Tabulated summaries of positions of maxima, minima for $g_{\mathrm{OO}}(r)$, $g_{\mathrm{OH}}(r)$ and $g_{\mathrm{HH}}(r)$ obtained from classical DPMD, D_2O PI-DPMD and H_2O PI-DPMD. The experiment data are extracted from Ref. [Soper and Benmore, 2008]

System	g_{OO}			g_{OH}		g_{HH}	
	r_{max1}(Å)	r_{min1}(Å)	r_{max2}(Å)	r_{max1}(Å)	r_{max2}(Å)	r_{max1}(Å)	r_{max2}(Å)
DPMD	2.73(9)	3.27(5)	4.40(4)	0.98(0)	1.77(3)	1.56(0)	2.30(0)
PI-DPMD (D_2O)	2.72(5)	3.26(0)	4.38(9)	0.98(2)	1.75(5)	1.57(1)	2.28(8)
PI-DPMD (H_2O)	2.72(1)	3.26(5)	4.38(0)	0.97(9)	1.75(4)	1.57(4)	2.29(6)
Expr. (D_2O)	2.76	3.35	4.45		1.81		2.37
Expr. (H_2O)	2.75	3.40	4.44		1.74		2.42

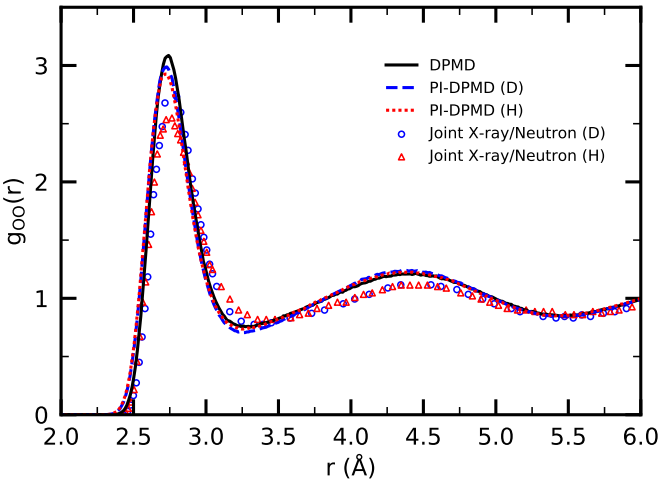

Figure 4.3: O-O RDFs of liquid water obtained from DPMD (black solid line), D_2O PI-DPMD (blue dashed line) and H_2O PI-DPMD (red dotted line). The heavy water (blue circle) and light water (red triangle) joint x-ray/neutron experimental data are extracted from Ref. [Soper and Benmore, 2008].

Figure 4.3 shows the O-O RDFs, $g_{\mathrm{OO}}(r)$, which reflect the overall structures of liquid water. The $g_{\mathrm{OO}}(r)$ obtained by PI-DPMD agrees better with the EPSR predictions as compared to DPMD results. The classical DPMD trajectory has a relatively more rigid first coordination shell and exhibits an over-structured first peak as compared to the PI-DPMD trajectories of light and heavy water. Specifically, the height of the first maximum of $g_{\mathrm{OO}}(r)$ goes from 3.08 in DPMD down to 2.99 in heavy water and 2.93 in light water. On the other hand, NQEs slightly strengthen the long range correlations between water molecules. The second peak is brought up by around 3%, while the first minimum is brought

down by around 5% from DPMD to PI-DPMD. Therefore, the aforementioned two competing NQEs are well reflected in $g_{\mathrm{OO}}(r)$. The above observations show that water structures go through minor but complicated overall structure changes under NQEs which agrees well with the conclusion of Yao *et al.* [Yao and Kanai, 2020]. In terms of isotope effects, heavy water shows a slightly higher first peak (by ∼0.06) than that of light water in PI-DPMD simulations; a result qualitatively agrees with the EPSR predictions (from 2.84 to 2.59). Moreover, the experimentally predicted ∼0.01 Å shift of the first $g_{\mathrm{OO}}(r)$ peak position upon isotope substitution is quantitatively reproduced. From D_2O to H_2O, the broadening of the first peak and slight height (from 0.71 to 0.74) and position (from 3.26 Å to 3.27 Å) increase of the first minimum can also be identified in PI-DPMD. This indicates H_2O has slightly more non-bonded water molecules and shows softer structures as compared to D_2O. As a result, the configurations of light water become more compact, which leads to a larger number density 0.10679 (0.10007) atom/Å^3 than that of D_2O 0.10619 (0.10000) atom/Å^3 in PI-DPMD simulations, where the number in parentheses denote the experiment value [Soper and Benmore, 2008]. Furthermore, in both PI-DPMD simulation and the referenced experimental data, substituting D by H shows negligible effects on $g_{\mathrm{OO}}(r)$ beyond the second peak ($r > 4.5$ Å). This indicates NQEs have insignificant impact on the long-range ordering of the H-bond network.

The O-H RDFs, $g_{\mathrm{OH}}(r)$, are shown in Figure 4.4, where a similar quantum nuclei induced systematic softening effect can be distinguished. The first peak of $g_{\mathrm{OH}}(r)$ corresponds to the O-H covalent bond, which is sensitive to the aforementioned quantum fluctuation along the stretching directions. As listed in Table 4.1,

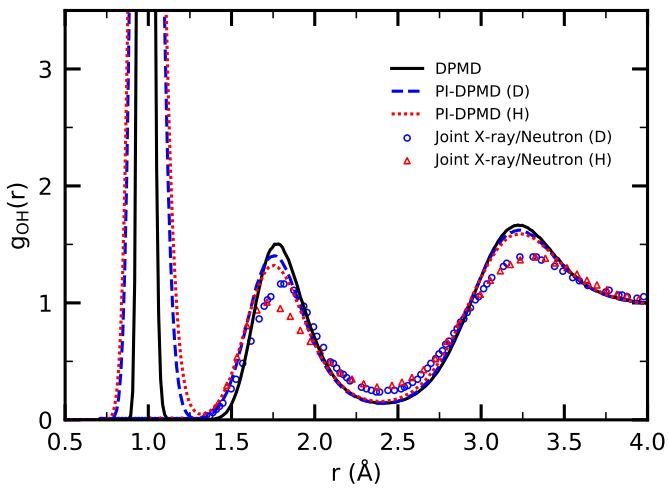

Figure 4.4: O-H RDFs of liquid water obtained from DPMD (black solid line), D_2O PI-DPMD (blue dashed line) and H_2O PI-DPMD (red dotted line). The heavy water (blue circle) and light water (red triangle) joint x-ray/neutron experimental data are extracted from Ref. [Soper and Benmore, 2008], which does not present the first peak around 1 Å.

peak positions are almost the same at around 0.98 Å in all simulations. However, as shown in Figure 4.4, the first peak exhibits an asymmetric distribution, where more H atoms tend to locate at the right side of the peak and form longer O-H covalent bonds, especially in the PI-DPMD simulations. This can be understood by that the H atom experiences an asymmetric potential, where the potential barrier at the covalent bond side is steeper than that at the H-bond side. Quantum fluctuations enables the H atom to explore more towards the less steep potential barrier direction, i.e. the H-bond side. Thus, the peak position is not a good indicator of the averaged O-H covalent bond length. In our simulations the averaged O-H covalent bond length for classical DPMD, heavy water, and light water are calculated to be 0.985, 1.000, and 1.006 Å, respectively. The 1.5% O-H covalent bond elongation from DPMD to PI-DPMD confirms the proton delocalization effect under NQEs. In PI-DPMD simulations, H_2O shows a ∼0.5% longer covalent bond length than D_2O, which is relatively small as compared to the 3% elonga-

tion from the EPSR results. However, our PI-DPMD simulations yields similar result to the 0.4% O-H and O-D covalent bond difference in gas phase measured by infrared spectroscopy [Cook et al., 1974] as well as a ∼0.5% difference of O-H and O-D covalent bond predicted by Zeidler *et al.* via neutron scattering data applying different analytical techniques [Zeidler et al., 2011]. The second peak of $g_{\mathrm{OH}}(r)$ reveals the distribution of H-bonds in liquid water. Similar to the covalent peak, the position of the second maximum of $g_{\mathrm{OH}}(r)$ is located at ∼1.76 Å and barely changes in all simulations. The integrated average H-bond length decrease from 1.88(1) in classical DPMD to 1.85(7) in D_2O PI-DPMD and 1.85(6) in H_2O. The reduction in height of the H-bonding peak indicates the increased amount of breaking H-bonds in liquid water under NQEs. Although the decrease of peak height from heavy water to light water are well reproduced in PI-DPMD simulations, the large position shit of 0.07 Å of the second peak that found in EPSR studies are not obtained in PI-DPMD simulations. The observed changes of the H-bond peak highly relate to the variation of local tetrahedral ordering in liquid water under NQEs which will be discussed in the next section. As for the third peak of $g_{\mathrm{OH}}(r)$, the inclusion of NQEs slightly softens the structure and improves both the peak height and peak position towards the experimental directions. The observed isotope effects beyond the second peak of $g_{\mathrm{OH}}(r)$ ($r > 2.5$ Å) are negligible in both PI-DPMD simulations and EPSR results.

The H-H RDFs, $g_{\mathrm{HH}}(r)$, are given in Figure 4.5. The first peak of $g_{\mathrm{HH}}(r)$ represents the distance between two H atoms in the same water molecule. The peak positions increase from 1.56 Å in classical DPMD to 1.57Å in both PI-DPMD simulations. However, the averaged H-O-H covalent bond angle are calculated to be

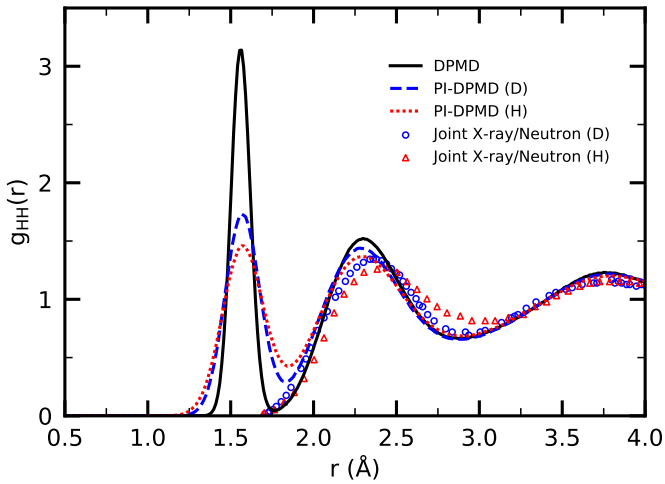

Figure 4.5: H-H RDFs of liquid water obtained from DPMD (black solid line), D_2O PI-DPMD (blue dashed line) and H_2O PI-DPMD (red dotted line). The heavy water (blue circle) and light water (red triangle) joint x-ray/neutron experimental data are extracted from Ref. [Soper and Benmore, 2008], which does not present the first peak around 1.5 Å.

the same (105.4 °) in all simulations. Thus, the increase of peak positions can be attributed to the elongation of O-H covalent bond length caused by NQEs. Moreover, the first peak of $g_{\mathrm{HH}}(r)$ is broadened under NQEs. This can be interpreted as that water molecules shows more spread configurations along both its libration and stretching directions. With regard to the second and third peaks, the changes due to the inclusion of NQEs and isotope effects are similar as discussed before in the case of $g_{\mathrm{OO}}(r)$. Quantum fluctuations slightly soften the liquid structures so that the curves obtained from PI-DPMD are flattened and fit the EPSR observations better compared with classical DPMD results. Isotope effects on peak shapes, such as the asymmetric changes on two sides of the second peak, and peak positions are qualitatively captured but with less extent than the EPSR data.

In summary, both proton elongation along the O-H covalent bond stretching direction and the fluctuations along proton libration direction are confirmed in $g_{\mathrm{OO}}(r)$, $g_{\mathrm{OH}}(r)$, and $g_{\mathrm{HH}}(r)$ RDFs. NQEs induce minor but complicated structural

changes in liquid water. As to isotope effects, the overall changes in the RDFs indicate that the quantum fluctuations weakening H-bonds dominate over the quantum effects that facilitate H-bonds. Therefore, the structure of light water becomes more disordered than heavy water.

4.5 Statistics of H-bond ordering

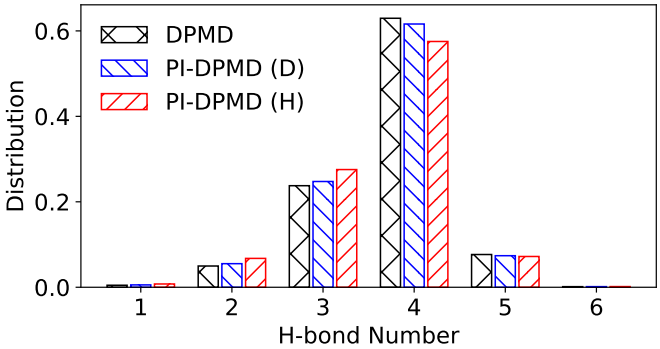

Figure 4.6: Distributions of average H-bond numbers per water molecule in liquid water obtained from DPMD (black solid), D_2O PI-DPMD (blue dashed) and H_2O PI-DPMD (red dotted).

To further understand the local arrangement of H-bonds in water, the average H-bond numbers formed by each water molecule are analyzed. We adopted the H-bond definition by Chandler *et al.* [Luzar and Chandler, 1996], where two water molecules are considered H-bonded if the O-O distance is smaller than 3.5 Å and O-O-H angle (the angle between O-O direction and O-H covalent bond direction) is less than 30°. In an ideal tetrahedral structure, each water molecules accept two and donate two hydrogen atoms, forming four H-bonds. In our DPMD, D_2O PI-DPMD, and H_2O PI-DPMD simulations the average H-bonds per molecule are 3.73, 3.70, and 3.64, respectively. H-bond tends to break slightly more with the increase of quantum fluctuations. To show the detailed information of the

H-bonds, the distributions of averaged H-bond numbers are given in Figure 4.6. Without NQEs, 63.0% water molecules form standard tetrahedral structures, i.e. four H-bonds with its neighbouring water molecules. This proportion goes down to 61.6% and 57.5% in PI-DPMD simulated heavy and light water. Accordingly, the ratio of water molecules with less than four H-bonds rises in quantum simulations. The isotope effect follows the same trend as the inclusion of NQEs. This trend illustrates that with H-bond fluctuations under NQEs, some water molecules that form tetrahedral structures have one or more H-bond broken and squeeze into the interstitial region of other water molecules, leading to a weakened overall liquid structure. Meanwhile, it is worth mentioning that other than a simple weakening effect of H-bond distribution, the proportion of water molecules with five H-bonds barely changes under NQEs. It can be explained by that NQEs have different effects on H-bonds with different strength [Li et al., 2011]. In other words, typical water-water H-bond are weakened but some strong ones are unchanged or even strengthened. The above serves as another evidence of the fact that the result of NQEs is a subtle balance among different competing effects, which leads to overall weakened structures in liquid water.

To further explore the changes of H-bond arrangements upon isotope substitution, the three-body oxygen-oxygen-oxygen (O-O-O) ADF $P_{OOO}(\theta)$ and the tetrahedral order parameter q of light and heavy water are studied and compared with EPSR results. The O-O-O ADF gives the probability of finding the triplet angle θ_{123} formed by oxygen atoms O_1, O_2, and O_3 in a local environment. O_1 and O_3 are located within a cutoff distance d from O_2, and d is chosen to yield an average O-O coordination number of 4.0 [Soper and Benmore, 2008]. In D_2O

PI-DPMD and H_2O PI-DPMD, the values of d are set to 3.205 and 3.210 Å, respectively. The tetrahedral order parameter q is defined as

$$q = 1 - \frac{3}{8}\langle\sum_{j=1}^{3}\sum_{k=j+1}^{4}(cos\theta_{jik} + \frac{1}{3})^2\rangle, \tag{4.2}$$

where for one water molecule i four nearest neighbors are considered and the bracket represents an average over all water molecules. It is important to note that q has a value between 0 and 1, where 1 represents the perfect tetrahedral structure and smaller values stand for distorted tetrahedral structures.

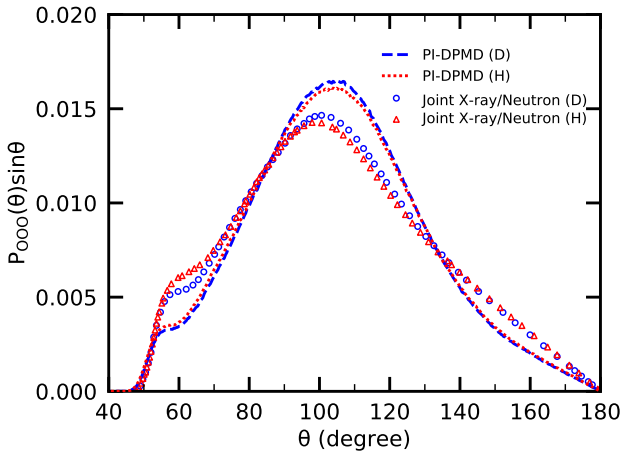

Figure 4.7: Triplet angular distribution of liquid water obtained from D_2O PI-DPMD (blue dashed line) and H_2O PI-DPMD (red dotted line) as well as the heavy water (blue circle) and light water (red triangle) joint x-ray/neutron experimental data [Soper and Benmore, 2008].

The triplet ADFs $P_{OOO}(\theta)$ are shown in Figure 4.7. Generally, $P_{OOO}(\theta)$ exhibits a principle maximum centered around 100° and a shoulder at around 60°. The main-peak angle around 100° is slightly smaller than the perfect tetrahedral angle 109.5°, depicting a liquid structure with majority of water molecules forms tetrahedral structures with slight distortions. The shoulder arises as a result of water molecules in the interstitial regions that have partially broken H-bonds [Guillot and Guissani, 1998; Chen et al., 2017]. Isotope effects observed in the

EPSR studies are qualitatively reproduced in our PI-AIMD simulations. Going from heavy to light water, one notices that the main peak is broadened, the peak position is slightly shifted from to 104.8° and 104.0° and the peak height decreases by around 3%. Moreover, the side peak becomes more prominent in light water as compared to heavy water. Both effects indicate the growth of the population of partially bonded water molecules, that donate either 0 or 1 H-bond to their neighbors and tend to form small-angle configurations, from D_2O to H_2O. The changes of local structures under NQEs can be further confirmed by the tetrahedral order parameter. From D_2O PI-DPMD to H_2O PI-DPMD, the values of q changes from 0.714 (0.593) to 0.707 (0.576), with the values in the parenthesis representing the experiment/EPSR results. Therefore, light water forms less local H-bonds and exhibits softer liquid structures.

4.6 Electronic properties

The strength of H-bond in liquid water is closely associated with the electronic properties of water molecules. In this section, electronic properties such as density of states (DOS) of valence electrons and molecular dipole moments (μ) are studied. Even though *ab-initio*-level electronic properties highly depend on the description of the underlying PES, which is determined here from the SCAN functional, the resulting electronic structures are modified under NQEs due to the changes of characteristic geometry as described in previous sections. Here we show that the PI-DPMD simulations improve the description of electronic properties in liquid water compared to the classical DPMD simulations.

Figure 4.8 shows the DOS of liquid water obtained from the DPMD and PI-

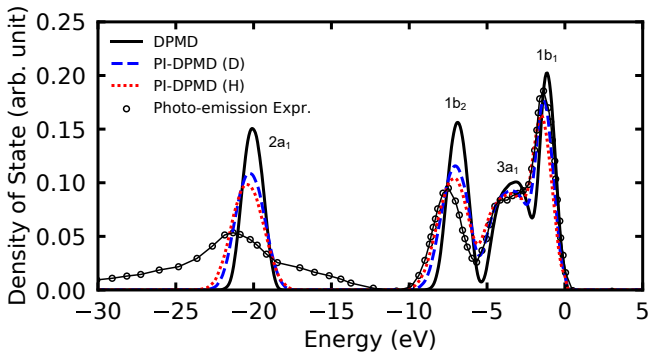

Figure 4.8: Density of state of liquid water obtained from DPMD (black solid), D_2O PI-DPMD (blue dashed) and H_2O PI-DPMD (red dotted). The density of state extracted from photoemission spectroscopy (black triangle) [Winter et al., 2004] is plotted as a reference.

DPMD simulations as well as photoemission spectroscopy [Winter et al., 2004]. A 0.1 eV Gaussian broadening factor [Prendergast et al., 2005] is adopted for the computed *ab initio* eigenstates. All DOS are aligned by the energy of the highest occupied states which is set to 0 eV. The DOS exhibits 4 peaks, that can be assigned to the $2a_1$, $1b_2$, $3a_1$, and $1b_1$ valence orbitals of water. These four orbitals are named by their spacial symmetries in the gas phase and labeled in Fig 4.8. On the one hand, as all our simulations are based on the SCAN DPMD model, the calculated binding energies of $2a_1$, $1b_2$, $3a_1$ peaks with respect to the $1b_1$ molecular orbitals are respectively around -2.0, -5.7, and -18.9 eV for all DPMD and PI-DPMD simulations, which is consistent with previous *ab initio* studies adopting the SCAN functional [Chen et al., 2017; Zheng et al., 2018] and fairly reproduces the result form the photoemission experiment (-2.3, -6.2, and -19.7 eV, respectively). On the other hand, one finds the peak width of the DOS is sensitive to NQEs [Chen et al., 2016]. In PI-DPMD simulations, all peak widths, especially the $1b_2$ and $3a_1$ orbital that are associated with the covalent bond, get broadened by a large extent towards the experiment. Also, the minima between

peaks is better reproduced as well compared to experiments.

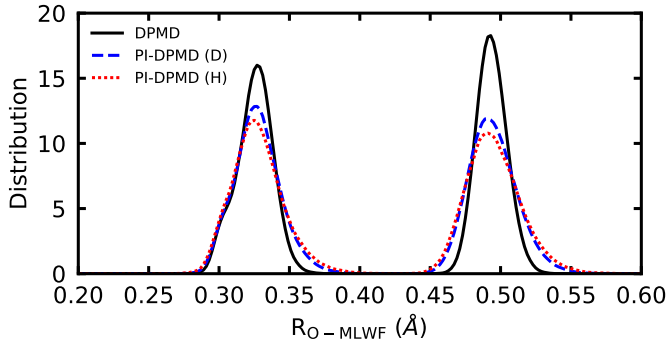

Figure 4.9: Distributions of the centers of MLWFs with respect to the oxygen position obtained from DPMD (black solid), D_2O PI-DPMD (blue dashed) and H_2O PI-DPMD (red dotted).

These four valance orbitals are correlated to four pairs of electrons in a water molecule. Two of the electron pairs distribute along water covalent bond and are labeled as bonding pairs. The other two electron pairs correspond to the lone pair of the oxygen atom. These four electron pairs can be represented by a unitary transformation of the Kohn-Sham eigenstates with the spread minimized in real space, i.e. the MLWFs. The distributions of distances between the four MLWFs centers and the oxygen atoms are shown in Figure 4.9. The figure exhibits two peaks. The peak located closer to the oxygen atom is originated from the lone pair electrons and the other peak represents the distribution of two bonding pairs. Lone pair electrons are sensitive to the altering of the H-bond network, as the formation of H-bond directly relates to the attraction force between positively charged H atom and the lone pair electrons with negative charges. In the classical simulation, the lone pair electrons show a subsidiary summit at 0.3 Å. This is attributed to the broken H-bonds in liquid water, where lone pair electrons experience less attractive force from the H-bond and move closer to the oxygen atom [Gaiduk and Galli, 2017]. Adding NQEs results in more broken H-bonds, as a result, the subsidiary

summit is pushed to a slightly higher probability in both PI-DPMD simulations. At the same time, more lone pair electrons move further away from oxygen to ∼0.37 Å, which reveals the H-bond facilitated effect in NQEs. In general, the lone pair peak moves from 0.328 Å in DPMD to 0.326 Å (heavy water) and 0.325 Å (light water) in PI-DPMD. The bonding pair peak locates at 0.492 Å and barely shifts when NQEs are included, while the distribution of bonding pairs becomes more asymmetric and shows bias towards elongation. These observations accord with the asymmetry of the O-H covalent bond distribution as described in $g_{\mathrm{OH}}(r)$.

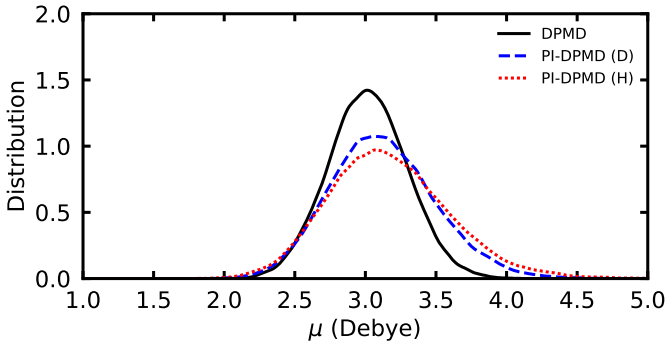

Figure 4.10: Distributions of dipole moments of water molecules obtained from DPMD (black solid), D_2O PI-DPMD (blue dashed) and H_2O PI-DPMD (red dotted).

The dipole moment of water molecules is an electronic property highly affected by the H-bond network in liquid water, which can be evaluated by the MLWFs center as:

$$\mu = \overrightarrow{\mathrm{R}}_{\mathrm{OH}_1} + \overrightarrow{\mathrm{R}}_{\mathrm{OH}_2} - 2\sum_{i=1}^{4} \overrightarrow{\mathrm{R}}_{\mathrm{OW}_i}, \tag{4.3}$$

where $\overrightarrow{\mathrm{R}}_{\mathrm{OX}}$ is the vector pointing from O atom to X which denotes either H atoms (H_1, H_2) or the ith MLWFs centers (W_i). In the gas phase, the dipole moment of a single water molecule is measured to be 1.885 D [Company and Lide, 2003]. Due to H-bonds, the value increases to 2.9 ± 0.6 D in liquid water [Badyal et al., 2000]. The calculated average dipole moments in DPMD and D_2O, H_2O simulations are

3.01 ± 0.03, 3.12 ± 0.04, and 3.17 ± 0.05 D, respectively. The polarization of water molecule increases with the growth of quantum fluctuations, which is due to the delocalized protons under the NQEs effects. As shown in Fig 4.10, a fraction of water molecules with extremely large dipole moment ($\mu > 3.5$ D) can be identified in PI-AIMD result. Once again, this result fits the aforementioned observation of the O-H covalent bond elongation and the increased probability of proton transfers under NQEs. However, the calculated dipole moments in our simulations are slighter larger than the experimental measurements. One may expect that minimizing the self-interaction error by adopting higher level hybrid functionals would localize the distribution of electrons and reduce the calculated dipole moment of liquid water towards the experimental direction.

4.7 Conclusion

In conclusion, we have systematically studied the NQEs and isotope effects in liquid water employing SCAN functional. Machine learning based DPMD and PI-DPMD simulations are performed at ambient conditions within the NpT ensemble. NQEs are shown to alter the structures of liquid water in different aspects. Specifically, the quantum fluctuations can either strengthen or weaken the H-bond depending on the local configurations. The predicted light water computed via SCAN PI-DPMD shows slightly softer structure as compared to the predicted heavy water. Both light and heavy water structures predicted by SCAN PI-DPMD are in good agreement with experiments. In particular, isotope effects on radial distribution functions, O-O-O triplet angular distribution as well as density found in experiment are qualitatively reproduced. Descriptions of electronic structure

by PI-DPMD are closer to experimental data than that of classical simulation. Therefore, the combination of machine learning based model (DPMD), high-level *ab initio* PES (SCAN) and quantum treatment of nuclei (PI) provides a promising approach for the modeling of liquid water with considerable time efficiency. In future work, we expect to alleviate the remaining discrepancies by adopting a higher-level exchange-correlation functional, such as hybrid SCAN functional (SCAN0), to reduce the self-interaction error in DFT and provide more accurate structures for the study of isotope effect.

CHAPTER 5

ISOTOPE EFFECTS ON X-RAY ABSORPTION SPECTRA OF LIQUID WATER

5.1 Introduction

The last decade has witnessed a rapid emergence of the x-ray absorption spectroscopy (XAS) being applied to probing the H-bond network of water [Wernet et al., 2004; Nilsson et al., 2010; Tse et al., 2008; Smith et al., 2006; Nilsson and Pettersson, 2015; Fransson et al., 2016; Amann-Winkel et al., 2016; Smith and Saykally, 2017]. In the XAS process, the time scale of the electron-hole interaction is much shorter than that of the molecular relaxation [Bernath, 2015]. Therefore, XAS carries out an instantaneous local fingerprint of water structure, which is complementary to the averaged structural information obtained in diffraction experiments [Soper and Benmore, 2008; Zeidler et al., 2011, 2012; Soper, 2019].

Light and heavy water have been extensively studied by various experimental techniques, however their differences in XAS only became available very recently by the increased spectral resolution in the transmission-mode spectroscopy technique [Schreck and Wernet, 2016]. It revealed that they are similar but not identical. The discernible spectral difference suggests H-bond networks in H_2O and D_2O are affected differently by nuclear quantum effects (NQEs) [Schreck and Wernet, 2016].

With the significant advances in XAS experiment, the theoretical exploration of XAS spectra is urgently needed to unambiguously associate spectral features to specific structural motifs of water, which requires both an accurate molecular structure and a proper treatment of electron-hole interaction. Based on density functional theory (DFT) [Hohenberg and Kohn, 1964], Feynman path-integral *ab initio* molecular dynamics (PI-AIMD) [Car and Parrinello, 1985; Marx and Parrinello, 1996; Ceriotti et al., 2013, 2014, 2016] provide an ideal platform to predict the liquid structure by including the NQEs. However, for decades, simulation of water has been a formidable task. Extensive studies have identified that the van der Waals interaction and exact exchange are key ingredients to differentiate between water and ice [Wernet et al., 2004; Zhang et al., 2011b; Wang et al., 2011; Møgelhøj et al., 2011; DiStasio et al., 2014; Gaiduk et al., 2015; Miceli et al., 2015; Del Ben et al., 2015; Chen et al., 2017]. To accommodate these fine effects, a non-local exchange-correlation functional should be adopted in functional construction that requires higher rungs [Sun et al., 2015; Perdew et al., 1996b; Adamo and Barone, 1999] in the metaphorical Jacob's ladder [Perdew, 2001]. In this regard, the modeling of water by SCAN functional [Sun et al., 2015] has shown great

accuracy in comparison to experiment [Chen et al., 2017]. In parallel, the modeling of electron excitation in the optical process stands as another major challenge that has been under active development for years [Hybertsen and Louie, 1986; Hetényi et al., 2004; Prendergast and Galli, 2006; Kang and Hybertsen, 2010; Rohlfing and Louie, 2000; Chen et al., 2010; Kong et al., 2012; Sun et al., 2017, 2018]. The excited electrons need to be treated as quasiparticles to solve the Bethe-Salpeter equation (BSE) [Vinson et al., 2011; Fransson et al., 2016], whose Coulomb interactions are screened by the electron sea in water. The proper treatments of the electronic screening, such as the Slater's transition state theory [Slater et al., 1969; Slater and Wood, 1970] or the more rigorous Hedin's GW approximation [Hedin, 1965; Hedin and Lundqvist, 1970] for the self-energy approach, is found to be crucial to qualitatively reproducing experimental XAS spectra. However, due to the significantly increased computational burden in solving BSE as well as in the PI-AIMD simulation, such theoretical studies so far remain elusive.

To address the above issues, we compute the XAS spectra of both H_2O and D_2O at oxygen K edge based on the self-energy approximation to the BSE. In particular, the liquid structures are generated from path-integral deep potential molecular dynamics (PI-DPMD) using a deep neural network-based potential energy model [Wang et al., 2018; Zhang et al., 2018a, 2019, 2018b; Ko et al., 2019] as introduced in chapter 4. The PI-DPMD scheme preserves the accuracy of SCAN-DFT with a computational cost comparable to that of empirical force fields. The resulting isotope effects in XAS spectra are in good agreement with experiment [Schreck and Wernet, 2016], which shows a stronger influence by NQEs in light water than in heavy water. The pre-edge of the XAS spectra, a signature of short-range or-

dering of H-bond network, shows a blueshift in the excitation energies and weaker spectral intensities in D_2O compared to H_2O, which originates from the shorter covalent bond but a stronger H-bonding environment in D_2O. For intermediate-range ordering, the light water exhibits an enhanced degree of inhomogeneity as revealed by local structure index analysis [Shiratani and Sasai, 1996; Duboué-Dijon and Laage, 2015; Santra et al., 2015]. Therefore, a more pronounced main-edge at lower energy is identified in H_2O because a softer liquid structure promotes the localization and stabilization of the excitons. The post-edge of XAS as an indicator of long-range ordering, however, has a negligible isotope effect. This is consistent with the nearly identical structures beyond second shell coordination as observed in chapter 4 and in the diffraction experiment [Soper and Benmore, 2008]. Our approach, combining accurate molecular dynamics simulations and the electron-hole theory, provides an important theoretical lens to understand the fine structures and quantum fluctuations of water by XAS.

5.2 Methods to compute XAS in liquid water

Similar to what is shown in chapter 4 the PI-DPMD simulations in this chapter were conducted in an isobaric-isothermal ensemble at 330 K and 1 bar for 0.3 ns with a 128-molecule supercell. For both H_2O and D_2O, one representative snapshot was selected from PI-DPMD trajectories and was adopted for the calculation of XAS spectra using our recently developed enhanced static Coulomb-hole and screened exchange approximation [Kang and Hybertsen, 2010; Sun et al., 2017]. The XAS spectra of H_2O and D_2O were aligned according to the position of the post-edge because the post-edges of H_2O and D_2O coincide in experiment [Schreck

and Wernet, 2016]. More details about PI-DPMD simulations and method to compute XAS are discussed in Appendix B.

5.3 Simulated x-ray absorption spectra

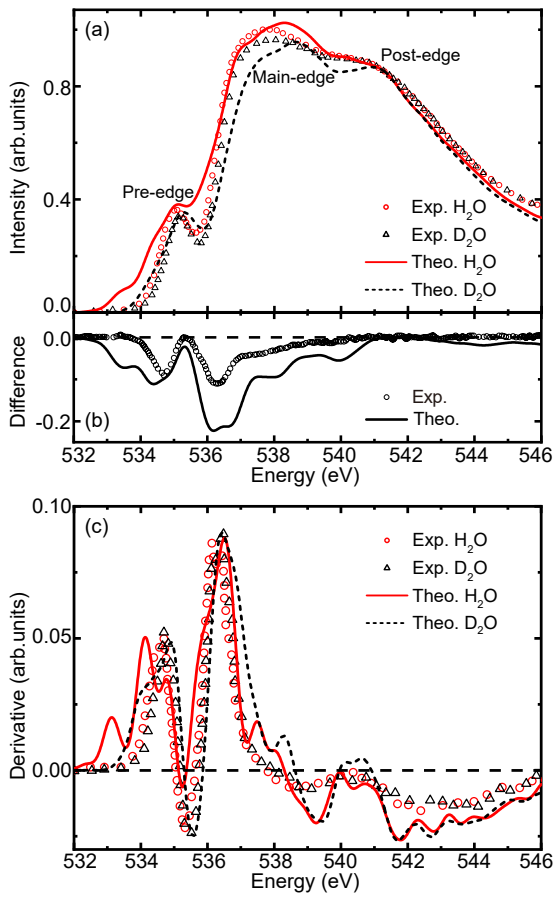

Figure 5.1: (a) XAS spectra of H_2O (red) and D_2O (black) from theory (solid and dashed lines) and experiment [Schreck and Wernet, 2016] (circles and triangles). (b) D_2O-H_2O difference of the XAS spectra from theory (line) and experiment [Schreck and Wernet, 2016] (circles). (c) First-order derivatives of the XAS spectra with respect to the energy of H_2O (red) and D_2O (black) from theory (solid and dashed lines) and experiment (circles and triangles).

The theoretical XAS spectra of both liquids H_2O and D_2O are presented in Figure 5.1(a) together with the experimental spectra [Schreck and Wernet, 2016]. A good agreement can be seen between the theory and experiment, not only on overall spectral shapes and all three features of pre-edge (∼535 eV), main-edge

($\sim$538 eV), and post-edge ($\sim$541 eV) in Figure 5.1(a), but also on the more delicate spectral differences between the two isotopes in Figure 5.1(b). (The small peak at $\sim$ 533.5 eV in the theoretical results in Figure 5.1 is caused by nuclear quantum fluctuation, which can be eliminated by averaging over more snapshots.) Within the same excitation energy scale, the spectrum of light water is slightly broader than that of the heavy water. In particular, the blueshifts of the peaks of pre- and main-edge are about 160 and 320 meV, which are close to the experimental values of 120$\pm$20 and 200$\pm$20 meV [Schreck and Wernet, 2016], respectively. A close inspection of the spectral difference between H_2O and D_2O in Figure 5.1(b) further reveals that the isotope effect in XAS is most significant in the pre- and main-edges, which decays rapidly and is negligible at the higher excitation energies in the post-edge. Apart from the XAS spectra and difference spectra, the first-order derivatives of the XAS spectra obtained in this work also agree well with experimental results [Schreck and Wernet, 2016] as shown in Figure 5.1(c). The successful prediction of the experimental measurement indicates that the H-bond structures and their signatures in electronic excitations of H_2O and D_2O are both accurately modeled.

In experiment, heavy water is characterized as a more structured liquid than light water [Soper and Benmore, 2008]. The subtle structural differences are accurately predicted as displayed in Figure 5.2(a). The oxygen-oxygen pair distribution functions, $g_{OO}(r)$, show more prominent first and second coordination shells in D_2O than those in H_2O, which agrees well with the diffraction measurement by Soper *et al.* [Soper and Benmore, 2008]. Since both heavy and light water share the same electronic configuration, their structural difference arises entirely from

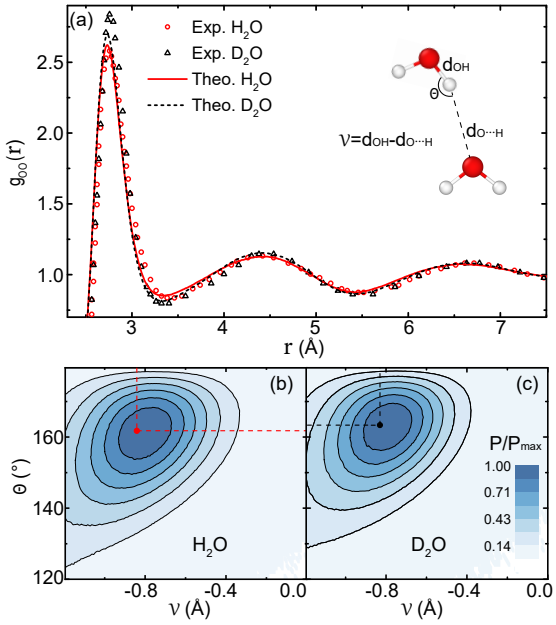

Figure 5.2: (a) $g_{\mathrm{OO}}(r)$ of liquids H_2O (red) and D_2O (black) from theory (solid and dashed lines) and experiment [Soper and Benmore, 2008] (circles and triangles). The inset shows definitions of proton transfer coordinate ν and OH$\cdots$O angle θ. Joint probability distributions of θ as a function of ν for (b) H_2O and (c) D_2O. The red dot located at $(-0.84, 161.80)$ in (b) and the black dot located at $(-0.83, 163.34)$ in (c) show the θ and ν values with the highest probability.

the NQEs that restructure their H-bond networks by different magnitudes. Under the influence of NQEs, the protons are more delocalized and are able to probe the configuration space that is inaccessible to the classical nuclei. The delocalized protons along the direction of the stretching mode promote the formation of H-bonds. As shown by the proton transfer coordinate [Wang et al., 2014] in Figure 5.2, the tendency of a proton to approach the acceptor molecule is increased under the larger NQEs in H_2O than in D_2O. On the contrary, the delocalized proton along the direction of the libration mode facilitates the breaking of H-bonds by perturbing the OH$\cdots$O angle, θ, further away from 180°. The overall NQEs resulting from the two competing effects are dependent on the anharmonicity of the potential energy surface [Li et al., 2011; Ceriotti et al., 2016]. In liquid water, recall from chapter 4, NQEs actually soften the liquid structure of light water

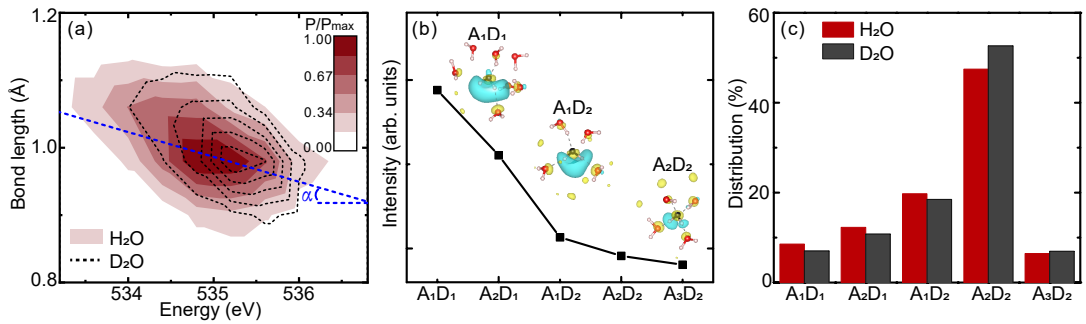

Figure 5.3: (a) Joint probability distribution of O-H/O-D covalent bond lengths as a function of excitation energies of states with $4a_1$ character of liquids H_2O (red shadows) and D_2O (dashed black lines). (b) Averaged intensities of states with $4a_1$ character as a function of A_iD_j in H_2O. A_iD_j indicates the number of acceptor-type (A_i) and donor-type (D_j) H-bonds, respectively. Insets show representative H-bond environments and distributions of quasiparticle wavefunctions (QWs). The excited oxygen atom is shown in black. QWs with opposite signs are depicted in blue and yellow. (c) Distributions of A_iD_j in liquids H_2O (red) and D_2O (grey).

with more broken H-bonds [Morrone and Car, 2008; Cheng et al., 2019]. Because of the heavier deuteron than proton, NQEs are suppressed in heavy water, which can be identified by the narrower distribution of deuteron as functions of ν and θ comparing to that in light water as shown in Figure 5.2(b) and (c). The slightly stronger H-bond of D_2O can be seen by the more parallelly aligned OH$\cdots$O angle and a proton transfer coordinate that is closer to zero than those of H_2O as shown by the red and black dots in Figure 5.2 (b) and 5.2 (c). The less perturbed H-bond network of D_2O than H_2O by NQEs is captured by distinct edge features in XAS spectra.

5.3.1 Pre-edge

The pre-edge is attributed to a bound exciton with a_1 characteristic whose origin can be traced back to the first electronic excitation in water vapor [Chen et al., 2010; Sun et al., 2017]. Once the water molecule is excited, a positive oxygen core-hole is left behind. The core-hole generates a strong potential that

traps excitonic states that are well localized within the molecule. Therefore, the pre-edge carries out a signature of short-range ordering of the H-bond network [Chen et al., 2010; Sun et al., 2017]. The excitation energies are sensitive to the relative position between proton and oxygen as determined by the covalent bond length, which is under constant thermal and quantum fluctuations. When the bond length becomes longer, the proton moves away from the excited oxygen. As a result, the enhanced electropositivity around the oxygen atom makes the core-hole Coulomb potential effectively stronger, which stabilizes the exciton with lower energy. The opposite trend is true when the bond length becomes shorter. The above effect gives rise to a negative correlation between pre-edge excitation energies and covalent bond lengths as shown by the red areas and dashed black lines in Figure 5.3(a). Moreover, the above negative correlation matches well with the anticorrelation between average covalent bond lengths and pre-edge energies of H_2O and D_2O as shown by the dashed blue line in Figure 5.3(a) which has a negative slope with $\tan\alpha$=0.006 Å/160 meV, where 160 meV is the blue-shift of the pre-edge and 0.006 Å is the bond length contraction when going from H_2O (1.005 Å) to D_2O (0.999 Å). The 0.6% covalent bond contraction ratio is close to the ratio of 0.5% found in the neutron diffraction experiment of Zeidler *et al.* [Zeidler et al., 2011] (the 3% contraction found in the experiment of Soper *et al.* [Soper and Benmore, 2008] is likely to overestimate the bond contraction as stated in Ref. [Ko et al., 2019]). At the same time, pre-edge of D_2O has a narrower spectral width than that of H_2O as observed in Figure 5.1, which is consistent with the suppressed quantum delocalization in D_2O as shown in Figure 5.2.

Besides the excitation energy, the spectral intensity is also affected by the

isotope substitution. According to the selection rule, the transition matrix element is determined by the p character in the excitation [Nilsson et al., 2010]. Based on symmetry analysis, the intensity of the pre-edge is weak, but not vanishing even for an intact H-bonding environment in crystalline ice [Wernet et al., 2004; Nilsson et al., 2010]. Moreover, the pre-edge intensity is rather sensitive to local distortions of the H-bond. As shown in our analysis in Figure 5.3(b), the spectral intensity in pre-edge is largely increased as the water structure is deviated from the ideal tetrahedron by more broken H-bonds, which enhances the p character of quasiparticle exciton. As aforementioned in chapter 4, the NQEs weaken the H-bonding strength in light water as compared to heavy water. The heavy water, therefore, shows a stronger H-bonding environment as displayed in Figure 5.3(c). Consistently, a slightly weaker pre-edge intensity of D_2O as compared to H_2O is seen in both experiment and theory.

5.3.2 Main-edge

The main-edge has been assigned to exciton resonance of b_2 characteristic, which originates from the second excited state in a water monomer [Chen et al., 2010; Sun et al., 2017]. Because it is unbound, its quasiparticle can no longer be confined within excited water molecules. Nevertheless, main-edge is relatively low in energy, and a certain degree of localization remains. As schematically plotted in the inset of Figure 5.4(b), quasiparticles of main-edge are largely distributed on the water molecules in first and second coordination shells, which gives rise to notable spectral intensities determining the main-edge feature. As a result, the main-edge serves as a probe of intermediate-range ordering of water [Chen et al.,

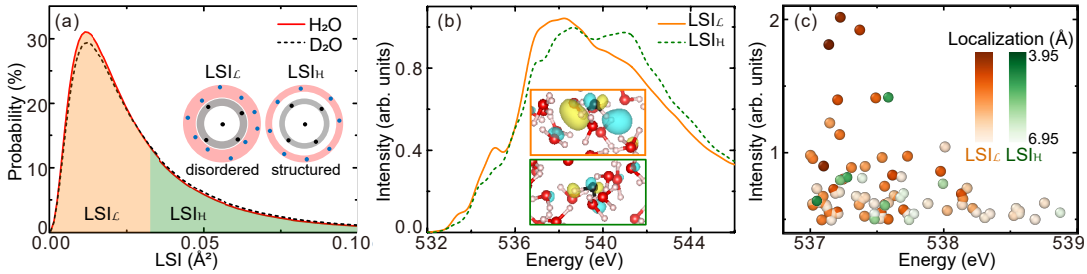

Figure 5.4: (a) Probability distributions of LSI of liquids H_2O (solid red line) and D_2O (dashed black line). The yellow and green shadows divide H_2O molecules into two parts: $\mathrm{LSI}_{\mathcal{L}}$ and $\mathrm{LSI}_{\mathcal{H}}$. Insets illustrate molecular configurations schematically, with each dot represents a water molecule. The grey and red areas show the first and second coordination shells, respectively. (b) XAS spectra of liquid H_2O contributed by water molecules in part $\mathrm{LSI}_{\mathcal{L}}$ (solid orange line) and part $\mathrm{LSI}_{\mathcal{H}}$ (dashed green line). The XAS spectra of D_2O contributed by $\mathrm{LSI}_{\mathcal{L}}$ and $\mathrm{LSI}_{\mathcal{H}}$ molecules have the same trend and are presented in Appendix B. Insets show representative QWs of excited water molecules in part $\mathrm{LSI}_{\mathcal{L}}$ (upper panel) and part $\mathrm{LSI}_{\mathcal{H}}$ (lower panel). (c) Intensities and excitation energies of excitons in the part $\mathrm{LSI}_{\mathcal{L}}$ (yellow circles) and part $\mathrm{LSI}_{\mathcal{H}}$ (green circles). Colors of the circles show the localization distance of QWs, which is defined as the radial distance from the excited oxygen atom that includes 80% of QWs. Excitons with excitation energy $\in$ [537, 539] eV and intensity larger than 0.5, which contribute to the formation of the main-edge, are presented.

2010; Sun et al., 2017].

In the intermediate-range, the softer liquid structure in H_2O is evidenced by both the less structured first and second coordination shells in the $g_{\mathrm{OO}}(r)$ [Figure 5.2(a)] and the slightly larger density of 0.10623 (0.10007) atom/Å^3 of H_2O than 0.10581 (0.10000) atom/Å^3 of D_2O. In the above, the number outside (within) parentheses denotes the theoretical (experimental [Soper and Benmore, 2008]) values. Therefore, more nonbonded water molecules in H_2O will flow into interstitial regions. Indeed, the light water has a slightly less deep first minimum in the $g_{\mathrm{OO}}(r)$, which is observed in both experiment and theory in Figure 5.2(a). With its denser interstitial regions, the light water is more disordered. In order to quantify the degree of inhomogeneity, we resort to the local structure index (LSI) analysis [Shiratani and Sasai, 1996; Duboué-Dijon and Laage, 2015; Santra et al.,

2015]. The resulting distributions of LSI are shown in Figure 5.4(a). Based on the average LSI value (0.0326 Å^2) of H_2O, we further decompose the LSI distributions into low LSI ($LSI_{\mathcal{L}}$) and high LSI ($LSI_{\mathcal{H}}$) regions in Figure 5.4(a), which are used to qualitatively describe the disordered and structured configurations, respectively. As expected, H_2O shows itself as a more disordered liquid through the more prominent peak in $LSI_{\mathcal{L}}$ as compared to D_2O. This structural difference is responsible for the observed isotope effect in XAS spectra at the main-edge.

Relative to the structured liquid in $LSI_{\mathcal{H}}$, the magnitude of disorder increases significantly in $LSI_{\mathcal{L}}$, whose quasiparticle wavefunctions become more localized in real space simultaneously as shown in Figure 5.4(c). The disorder-promoted excitation localization is a well-known effect in semiconductors due to the enhanced backscattering processes [Klingshirn, 2005; Tongay et al., 2013]. The similar mechanism applies in water; the surrounding water molecules, similar to defects in semiconductors, serve as the scattering center. Besides, the enhanced localizations also stabilize the excitonic states and give rise to larger transition matrix elements. The above can be clearly seen by the systematically red-shifted energies and much stronger spectral intensities at the main-edge of $LSI_{\mathcal{L}}$ than those of $LSI_{\mathcal{H}}$ in Figure 5.4(b). The light water is composed of a slightly larger fraction of $LSI_{\mathcal{L}}$, therefore, the resulting main-edge of XAS in H_2O is located at lower energy with higher amplitude relative to that of D_2O in Figure 5.1(a).

5.3.3 Post-edge

The electronic excitations at the post-edge are exciton resonant states as well, which share the same b_2 in orbital characteristic [Chen et al., 2010; Sun et al.,

2017]. However, they are much higher in energy than those in the main-edge. Not surprisingly, the remaining localization in the main-edge is completely absent. At post-edge, the exciton resonances become Bloch-like states that distribute over the entire space of liquids [Chen et al., 2010; Sun et al., 2017]. The above delocalized nature makes the post-edge an indicator of the long-range ordering of the H-bond network of water. It can be seen in Figure 5.1 that the isotope effect at post-edge is almost negligible, which is consistent with the almost identical $g_{OO}(r)$ beyond the second coordination shell [Schreck and Wernet, 2016] [Figure 5.2 (a)].

5.4 Conclusion

In conclusion, we have studied the isotope effect in XAS spectra of water by advanced theoretical methods. The electron-hole excitation was modeled by quasiparticle approach to solving the Bethe-Salpeter equation approximately. Facilitated by machine learning techniques, the liquid structures were generated from PI-DPMD simulations with the accuracy of the SCAN meta-generalized gradient approximation functional. Our theoretical simulations have reproduced the isotope effect in XAS spectra of water semi-quantitatively, with the isotopic XAS spectral differences slightly larger than experimental results, which are expected to be improved in future studies with more accurate methods in the description of molecular structure and electron-hole interactions. The observed blueshifts of spectral energies with weaker intensities, on pre- and main-edge, indicate that the heavy water has a slightly more structured H-bond network in short- and intermediate-range than light water. This is due to the intricate competing effects from NQEs that affect the heavy water slightly less than light water. The success-

ful theoretical modeling of the delicate isotope effect on XAS spectra will provide an important means for further exploration of the delicate nature of the H-bond network of water.

CHAPTER 6

NUCLEAR QUANTUM EFFECTS ON THE HYDRATION OF CHLORIDE ION

6.1 Introduction

Hydrated chloride ions (Cl^-) are ubiquitous in nature. The precise nature of the interaction between hydrated chloride (Cl^-) anions and the hydrogen-bond network is of fundamental importance for a broad range of fields such as biochemistry [Bezanilla, 2008], atmospheric chemistry [Knipping, 2000; Spicer et al., 1998; Foster et al., 2001], and geological processes [Beekman et al., 2011]. For example, Cl^- ions are essential components in the electrolytes of living systems [Jentsch et al., 2002]. Also, Cl^- is a member of the Hofmeister series of ions [Hofmeister,

1888], with important effects on protein solubility and folding. Moreover, chloride ion channels are a diverse group of anion-selective channels involved in the excitability of skeletal, cardiac, and smooth muscle cells [Hofmeister, 1888]. These important biochemical and physiological roles all involve Cl^- in an aqueous environment. Not surprisingly, the hydration structure of Cl^-, and its impact on the hydrogen (H)-bonding network of water have been the subject of intense scientific research for decades [Cummings et al., 1980; Ohtaki and Radnai, 1993; Leberman and Soper, 1995; Knipping, 2000; Ghosal, 2005; Marcus, 2009; Piatkowski et al., 2014].

The arrangement of water around Cl^- can be probed by scattering experiments [Neilson et al., 2001; Mancinelli et al., 2007b,a], and the perturbed H-bond structure is inferable from spectroscopic measurements[Dang et al., 2006; Smith et al., 2007; Kulik et al., 2010; Migliorati et al., 2014]. But most experiments typically yield only time-averaged structural information. At molecular level, the solvation structure of Cl^- is constantly fluctuating on a sub-picosecond time scale. In this regard, *ab initio* molecular dynamics (AIMD) simulation [Car and Parrinello, 1985] has already proven to be a valuable theoretical tool. In AIMD, forces needed to propagate the dynamics are generated from the instantaneous ground state of density functional theory [Kohn and Sham, 1965]. AIMD can directly model the fast exchange of water molecules within the anion's hydration shell, as well as the H-bond fluctuations in water solvent. AIMD simulations of chloride in solution, Cl^-(aq), have been carried out since the 1990s [Laasonen and Klein, 1997; Tobias et al., 2001; Heuft and Meijer, 2003; Kulik et al., 2010; Ge et al., 2013; Zhang et al., 2013; Bankura et al., 2013; Gaiduk et al., 2014; Bankura et al., 2015; Pham

et al., 2016; Gaiduk and Galli, 2017]. Consensus has been reached on the fact that the water structure in the first hydration shell is strongly distorted. The chloride anion, as a H-bond acceptor, is polarized in solution due to its large size [Perera and Berkowitz, 1992; Ohtaki and Radnai, 1993; Tobias et al., 2001; Ge et al., 2013; Migliorati et al., 2014; DelloStritto et al., 2020]. Therefore, the distribution of water molecules in its first coordination shell is rather inhomogeneous [Ge et al., 2013]. Such a defect-like solvation pattern around Cl^- is incompatible with the tetrahedral structure of water and disrupts the H-bond network in the solution. Beyond the first solvation shell, recent AIMD simulations [Gaiduk and Galli, 2017] carried out using the PBE functional [Perdew et al., 1996a] at an elevated temperature of 400K found a well-structured second solvation shell for Cl^- and weakened H-bonds as far as the third solvation shell. These previous studies have provided important insights on Cl^-(aq), but some issues remain unresolved. For example, one might expect that the water structure in saltwater is noticeably different from that of pure water. However, an analysis based on neutron scattering data surprisingly suggested that the disruption of the water structure by solvated Cl^- is negligible beyond the first shell [Mancinelli et al., 2007b,a].

Rationalization of the neutron scattering data requires atomic details on the solvation structure of Cl^-. In order to tackle this problem quantitatively with AIMD, one needs to employ an accurate exchange-correlation functional. Moreover, as shown in previous chapters, proper treatment of nuclear quantum effects (NQEs) associated with the system's protons is not optional, but indispensable in order to produce a liquid water structure compatible with the experimental observation [Tuckerman, 1997; Morrone and Car, 2008; Ceriotti et al., 2013; Sun

et al., 2018]. Notably, the role of NQEs varies significantly among different types of H-bonds [Li et al., 2011]. This new twist elevates the level of complexity in the computations. Two distinct types of H-bonds exist simultaneously in Cl^-(aq), namely the water-water (W-W) and anion-water (A-W) H-bonds. The former tends to build an extended tetrahedral network [Chen et al., 2017], while the latter tends to form a tight A-W cluster surrounded by additional solvent water molecules. The resulting Cl^- hydration structure reflects a delicate balance between these two competing effects. NQEs tilt the balance between these competing H-bonding forces, which in turn lead to a different hydration structure than is modeled using classical nuclei.

In this chapter we focus on probing the structure of Cl^-(aq) via Feynman path integral [Feynman and Hibbs, 1965] *ab initio* molecular dynamics (PI-AIMD) simulations, and traditional AIMD with classical nuclei. The nuclear potential energy surface is generated by employing the SCAN functional [Sun et al., 2015]. Surprisingly, NQEs tilt the balance between the competing W-W and A-W H-bonding and give rise to important changes to the anion's hydration structure. Under the influence of NQEs, both types of H-bonds are weakened. However, the A-W H-bond is weakened to a greater extent than the corresponding W-W H-bond. As a result, water molecules in the first hydration shell are relatively less tightly bound by the anion, and thus more amenable to accommodating the water solvent structure. While the first hydration shell still disrupts the water structure, surprisingly the solvent partially recovers its tetrahedral order. When compared to results based on classical nuclei, the PI-AIMD simulation shows that the influence of Cl^- on the water structure, beyond the first shell, is much weaker and, importantly,

the solvent H-bond network is seemingly rapidly restored to its bulk-like behavior. The PI-AIMD result shows excellent agreement with the experiments by Soper [Mancinelli et al., 2007a,b]. In particular, the satellite peak of the H-Cl-H angular distribution derived from neutron scattering data only appears in the PI-AIMD simulations, and is absent in conventional AIMD. Thus, NQEs give important corrections to the computed Cl^-(aq) hydration structure, yielding more consistent results when compared to experiments. The present findings strongly suggest that NQEs should be included in future studies of the Hofmeister series.

6.2 Method

All AIMD and PI-AIMD calculations were performed in the canonical ensemble at T=300K using a periodically replicated cubic box with edge length 12.42 Å. One Cl^- ion and 63 H_2O molecules were included in the 0.87 M Cl^- aqueous solution. AIMD and PI-AIMD pure water simulations with 64 water molecules were performed. Maximally localized Wannier Function (MLWF) [Marzari and Vanderbilt, 1997; Marzari et al., 2012] centers were computed to study electronic properties. More simulations details are discussed in appendix C.

6.3 Competing NQEs on H-bond

As already mentioned, a water molecule in the first hydration shell of Cl^- is subjected to competing forces provided by A-W and W-W H-bonds. Thus, one proton in the water molecule points towards Cl^-, while the other points to lone pair electrons of solvent water, as illustrated in the inset of Figure 6.1 (See

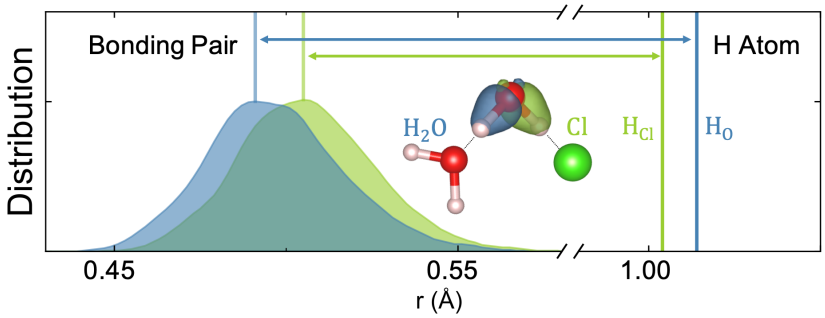

Figure 6.1: In PI-AIMD, the distribution of distances from the intramolecular oxygen to the MLWF centers for bonding pair electrons; vertical lines denote average positions of two types of protons bonded to solvent water or to Cl^-, as shown in the inset together with density isosurfaces of MLWF for bonding pair electrons.

appendix C for more details). Furthermore, this hydration shell water molecule is polarized by this special H-bonding configuration. Under its polarizing effect, the electropositive proton and the electronegative bonding pairs are separated further apart from each other generating a larger electric dipole in the condensed phase than that in water vapor [Badyal et al., 2000; Eisenberg and Kauzmann, 2005]. However, the abilities to polarize water are different for these two types of H-bonds as determined by the electronic structural properties. The A-W H-bond has a weaker bonding strength than that of W-W, as evidenced by the shorter distance between the bonding electron pairs and the proton in Figure 6.1 [Chen et al., 2018]. The relative weaker A-W bond also reduces the electric dipole of water molecules in the first hydration shell by ∼3% compared to that in bulk water; an effect which has been reported [Schmidt et al., 2009a; Guardia et al., 2009].

Besides its impact on the electronic structure, H-bonding also affects the proton position [Tuckerman, 1997]. The above effect is explored via the proton transfer coordinate (ν) [Ceriotti et al., 2013; Sun et al., 2018]. The resulting distribution functions, $P_{OH\cdots O}(\nu)$ and $P_{OH\cdots Cl}(\nu)$ are shown in Figure 6.2(a) and (b) for water

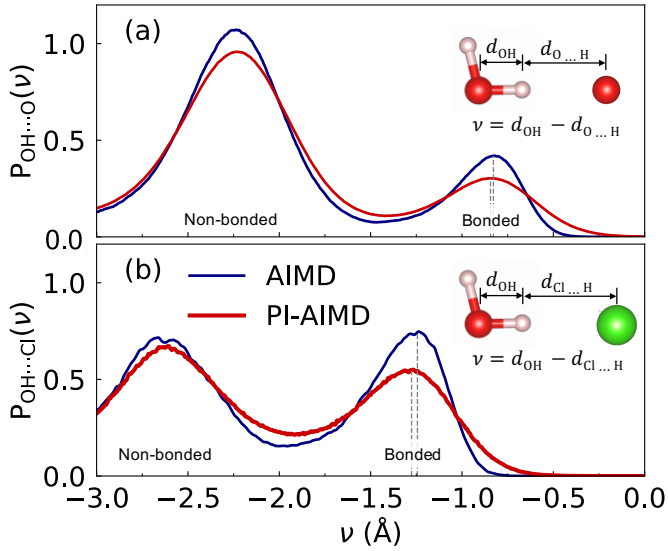

Figure 6.2: Spatial distributions of proton transfer coordinate ν for water molecules in Cl^-(aq) within (a) the solvent (b) anion's first hydration shell from AIMD and PI-AIMD.

molecules in the bulk solvent as well as in the first hydration shell of Cl^-, respectively. In general, two distinct features can be identified in $P(\nu)$. The feature at more negative ν (around −2.2 Å in $P_{OH\cdots O}(\nu)$ and −2.7 Å in $P_{OH\cdots Cl}(\nu)$) is contributed by the non-bonded hydrogen. Whereas, the other feature (around −0.8 Å in $P_{OH\cdots O}(\nu)$ and −1.2 Å in $P_{OH\cdots Cl}(\nu)$, denoted as $P^B_{OH\cdots O}(\nu)$ and $P^B_{OH\cdots Cl}(\nu)$) originates from the bonded hydrogen atoms via the W-W or the A-W H-bonds in Figure 6.2(a) and (b), respectively. The shorter distance in the bonded peaks is attributed to the fact that protons are more likely to approach the acceptors, i.e. an enhanced tendency of proton transfer [Ceriotti et al., 2013; Chen et al., 2018], under the attractive H-bond force. As expected, peak positions of $P^B_{OH\cdots O}(\nu)$ and $P^B_{OH\cdots Cl}(\nu)$ are the equilibrium positions of protons determined by the average strength of H-bonds under thermal fluctuations. The different peak positions of $P^B_{OH\cdots O}(\nu)$ and $P^B_{OH\cdots Cl}(\nu)$ are mainly caused by the size difference between Cl^- anion and oxygen atom [Shannon, 1976].

Both types of H-bonds undergo notable changes when protons are treated with NQEs in PI-AIMD simulations. On the one hand, the zero-point motion significantly expands the region that protons are able to explore on the potential energy surface, which is inaccessible to classical nuclei. Therefore, both $P_{OH\cdots O}(\nu)$ and $P_{OH\cdots Cl}(\nu)$ show a broader distribution in PI-AIMD trajectories. On the other hand, centers of $P^{B}_{OH\cdots O}(\nu)$ and $P^{B}_{OH\cdots Cl}(\nu)$ move further away from its acceptors, which suggests that both H-bonds are weakened in PI-AIMD. The fact that H-bonding is weakened by NQEs has been recognized recently in pure water [Ko et al., 2019; Cheng et al., 2019], which yields an important refinement to theoretical descriptions of water structure. More importantly, H-bonding strength varies among different types of H-bonds. The protons are more delocalized by NQEs. However, while delocalization of the proton along the stretching direction facilitates H-bond formation, delocalization due to proton libration tends to weaken the H-bond. The result represents a delicate balance of the aforementioned opposing NQEs. A rule of thumb proposed by Michaelides *et al.* states that the relatively weak H-bond will become even weaker by NQEs and *vice versa* [Li et al., 2011]. Indeed, a close inspection reveals that the peak position of $P^{B}_{OH\cdots O}(\nu)$ has a much larger shift moving away from acceptors than that of $P^{B}_{OH\cdots Cl}(\nu)$. Importantly, this means that the A-W H-bond becomes even weaker than the W-W H-bond under NQEs.

6.4 NQEs on the first hydration shell of Cl^- ion

Figure. 6.3(a) and (b), present the Cl-O radial distribution functions (RDFs) $g_{ClO}(r)$ from the Cl^-(aq) trajectories for both AIMD and PI-AIMD. For compar-

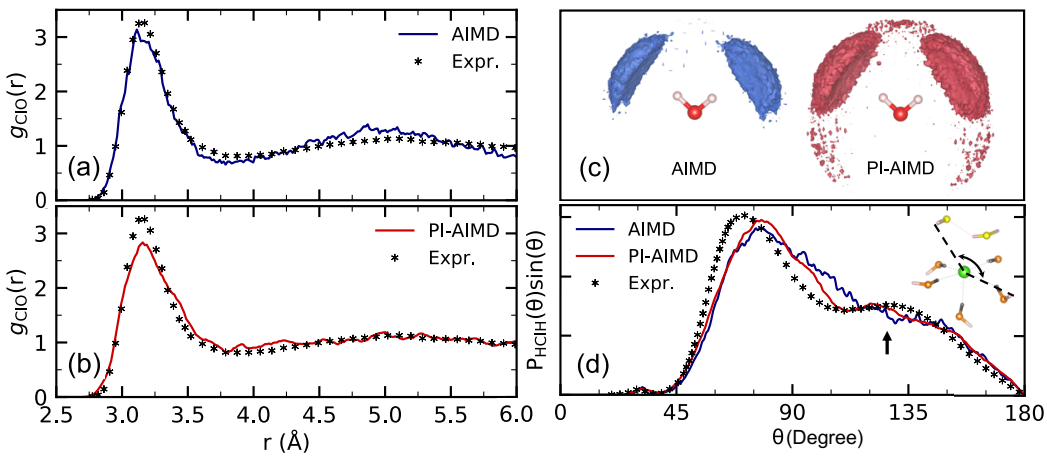

Figure 6.3: Cl-O RDFs in Cl^-(aq) from (a) AIMD and (b) PI-AIMD simulations, with neutron diffraction result [Mancinelli et al., 2007a]. (c) Isosurface of probability of finding a Cl^- ion first neighbor of a water molecule in AIMD and PI-AIMD simulations. The contrast level of the isosurface is set to 0.70. (d) Probability distribution of H-Cl-H angles in the first hydration shell of Cl^- from AIMD, PI-AIMD simulation, and neutron diffraction experiment [Mancinelli et al., 2007a]. The inset shows polarized Cl^- hydration structures, where water molecules in the first hydration shell are classified by bonded (orange) and non-bonded (yellow) to Cl^-.

ison, the experimental $g_{\mathrm{ClO}}(\mathrm{r})$ derived from neutron scattering is shown. Clearly, the Cl-O interaction is overly structured in the AIMD simulation, Figure 6.3(a). The artificially strengthened Cl-O attraction with classical nuclei brings the first (at 3.14 Å) and second hydration shells (at 4.91 Å) closer to the anion, relative to the experimental peaks, at 3.16 Å and 5.09 Å (See appendix C for more details). Moreover, the first minimum and second maximum are more prominent than those in experiment. In contrast, the more weakened A-W H-bond due to NQEs should loosen the anion's hydration shell. Indeed, the Cl-O interaction is weakened in the PI-AIMD simulation, as shown in Figure 6.3(b). Consistently, the center position of both first (at 3.16 Å) and second hydration shells (at 5.00 Å) increases and yields better agreements with the experiment. At the same time, the overall $g_{\mathrm{ClO}}(\mathrm{r})$ from PI-AIMD becomes much less structured, which then shows quantitative agreement with the experiment.

Because Cl^- is polarized in solution, bonded water molecules tend to preferentially populate one side of the anion while leaving the other half-space relatively empty, with sporadic residence of non-bonded molecules (See appendix C for more details). To accept a H-bond, Cl^- is located close to a proton along the bonding direction. The AIMD trajectory shows Cl^- distributes within a narrow region with a double *dome-like* shape in Figure 6.3(c). The overall solvation cage, composed of both bonded and non-bonded water molecules in the first hydration shell, can be described by a polyhedron with ∼7 vertices, as illustrated in the inset of Figure 6.3(d). Consistent with the polyhedral geometry under thermal fluctuations, the H-Cl-H triple angular distribution $P_{\mathrm{HClH}}(\theta)$ as plotted in Figure 6.3(d) is centered at ∼70° in AIMD, which is in qualitative agreement with experiment. However, a second broader peak that appears clearly in experiment around 130° is absent in the AIMD simulation.

In PI-AIMD, the solvation cage changes its geometry accordingly as a result of NQEs. Due to the weakened A-W H-bond, the average distance between the chloride ion and its bonded water molecules slightly increases from 3.235 Å to 3.249 Å. And the *dome-like* distribution of Cl^- spreads out over a larger area due to quantum fluctuations, as shown in Figure 6.3(c). Again, because of the weaker A-W bonding, Cl^- can no longer bond as many water molecules as it does in the AIMD trajectory. As a consequence, the population of non-bonded water molecules largely increases by ∼50% from ∼1.6 in AIMD to ∼2.4 in PI-AIMD (See appendix C for more details). The increased number of non-bonded water in the first hydration shell can be further confirmed by the significantly increased distribution of Cl^- in the region around the oxygen. With more vertices

occupied by non-bonded water molecules, the solvation cage predicted by PI-AIMD has geometric characteristics different from that of AIMD. Because the bonded and non-bonded water molecules are located on opposite sides of Cl^-, the triplet angular distribution $P_{HClH}(\theta)$ that involves a non-bonded water molecule mostly contributes to an obtuse angle as demonstrated in the insert of Figure 6.3(d). As a result, the second broad peak in $P_{HClH}(\theta)$ centered around 130° emerges in the PI-AIMD simulation, as seen in Figure 6.3(d); a finding which is in excellent agreement with experiment.

6.5 NQEs on the perturbed liquid water structure

The presence of Cl^- disrupts the H-bond network, and distortions are expected around the solvated ion. Figure 6.4(a) presents the normalized tetrahedral structure order parameter, $\bar{Q}$ [Chau and Hardwick, 1998] of water solvent in different hydration shells, as computed from both AIMD and PI-AIMD trajectories. Noting that $\bar{Q}$ shows the anion's disruptive effect on the tetrahedral structure of pure water (See appendix C for more details). Not surprisingly, the most abrupt distortion takes place in the first hydration shell because the solvation cage polyhedron is intrinsically different from a tetrahedron. Consistently, the first peak of $g_{OO}^{1st}(r)$, the O-O RDF computed by only water molecules in the first hydration shell, is also drastically different from bulk water as shown in Figure 6.4(b). Away from the solvated anion, the degree of distortion on H-bond network decays, and the tetrahedral water structure gradually recovers to its bulk value in the second hy-

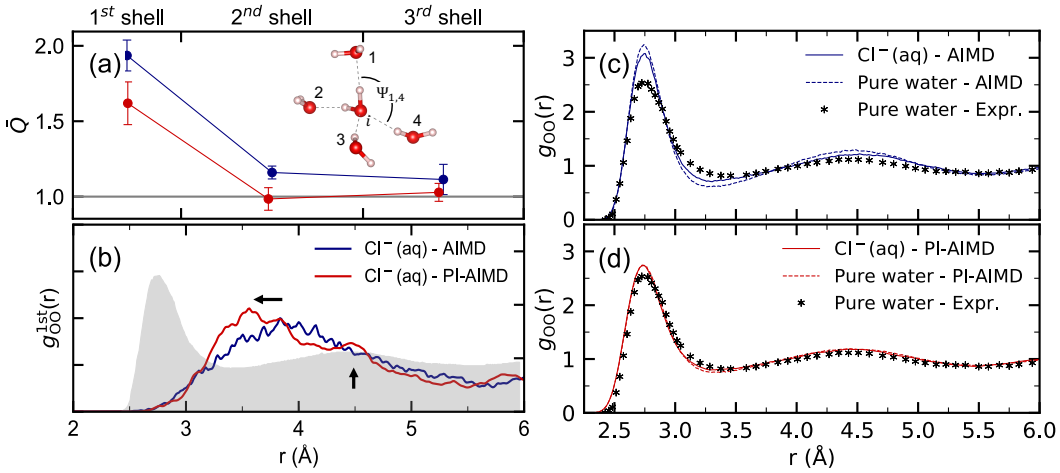

Figure 6.4: (a) Normalized tetrahedral structure order parameter $\bar{Q}$ decay as a function of the distance to Cl^- from AIMD and PI-AIMD. For water molecule i, $Q_i = \frac{3}{32}\sum_{j=1}^{3}\sum_{k=j+1}^{4}(\cos\psi_{\mathrm{j,k}} + \frac{1}{3})^2$, where j and k are the jth and kth nearest neighbor of water molecule i, and $\psi_{j,k}$ is the angle between molecule i, j and i, k. $\bar{Q}$ defined by $\langle Q_i\rangle_{\mathrm{solution}}/\langle Q_i\rangle_{\mathrm{water}}$, is the averaged and normalized Q. (b) AIMD and PI-AIMD O-O RDFs within the first Cl^- hydration shell computed by water bonded to Cl^-, along with regular O-O RDFs of bulk water. And O-O RDFs of (c) AIMD and (d) PI-AIMD Cl^-(aq) simulations, with AIMD and PI-AIMD pure water simulations, and diffraction experiment [Soper and Benmore, 2008].

dration shell and beyond as shown in Figure 6.4(a). In AIMD, the remaining distortion is non-negligible for solvent structure in the second and third hydration shells. As a result, the overall g_{OO}(r) of AIMD is softened as compared to that in bulk water modeled by AIMD. This effect has been attributed to a long-range structural disturbance on the underlying H-bond network by Cl^- [Gaiduk et al., 2014; Gaiduk and Galli, 2017].

Interestingly, the inclusion of NQEs in PI-AIMD lessens the impact of anion on the underlying H-bond network. A water molecule in Cl^-(aq) is attracted by two competing forces from the Cl^- anion and the solvent water. The aforementioned more weakened A-W H-bond makes it easier for water molecules to attract each other and restore the tetrahedral liquid structure. Indeed, the facilitated water structure can already be seen in the first hydration shell (See appendix C for more

details). As shown in Figure 6.4(b), the H-bond network is still largely disrupted in the first coordination shell. However, it becomes more structured; this can be seen by the decreased distance of the first peak, as well as the appearance of a second peak around 4.5 Å, which coincides with the peak position of the second hydration shell of g_{OO}(r) in bulk water. Clearly, this indicates a partial recovery of the solvent water structure. By the same token, the normalized structural order parameter $\bar{Q}$ recovers more quickly its bulk value in the PI-AIMD simulation in Figure 6.4(a). The resulting overall g_{OO}(r) of the solvent in PI-AIMD is also very close to that in bulk water in Figure 6.4(d). The relatively small impact on the water structure caused by Cl^-, as modeled by including NQEs, agrees well with the conclusions based on analysis of neutron scattering data [Mancinelli et al., 2007a] and terahertz absorption spectroscopy [Funkner et al., 2012]. Notably, inclusion of NQEs not only gives a more accurate description of Cl^-(aq) but also play an essential role in describing the bulk water structure more accurately. The computed g_{OO}(r) via PI-AIMD greatly helps to improve the agreement between theory and experiment.

6.6 Conclusion

In conclusion, NQEs have a surprisingly large influence on the hydration structure of Cl^-(aq). Specifically, the interaction between water and Cl^- is weakened, so that the anion's disruptive effect on the solvent H-bond network of solvent water is reduced. The predicted hydration properties computed via PI-AIMD agree well with experiments. In particular, the emergence of the satellite peak in the H-Cl-H triangular distribution function in the PI-AIMD trajectory is a clear signature of

NQEs. The present results highlight the important role played by NQEs in ionic solutions involving the Hofmeister series. Complementary studies of NQEs on hydration of cations, such as Na^+(aq) and K^+(aq), should be interesting. Unlike Cl^-, these cations are not H-bonded to water in solution, and only the underlying water solvent will be affected by NQEs. Therefore, distinct corrections by NQEs are expected.

CHAPTER 7

NUCLEAR QUANTUM EFFECTS ON THE ELECTRONIC STRUCTURE OF CHLORIDE SOLUTION

7.1 Introduction

As discussed in chapter 6, the interaction between the solvated Cl^- anion and the surrounding aqueous environment has been studied by various experimental methods such as x-ray and neutron scattering [Cummings et al., 1980; Copestake et al., 1985; Yamagami et al., 1995; Megyes et al., 2008] as well as x-ray absorption (XAS) spectroscopies [Tongraar et al., 2010; Dang et al., 2006]. These techniques provide structural information about the hydration of ions, such as the Cl-O and Cl-H radial distribution functions (RDFs), $g_{\mathrm{ClO}}(\mathrm{r})$ and $g_{\mathrm{ClH}}(\mathrm{r})$, as well as the sol-

vation coordination numbers within the first hydration shell of the Cl^- anion. Complementary to the molecular structure probed by the scattering experiment, the electronic structure of the ionic solution can be directly obtained by photoelectron spectroscopy [Gaiduk et al., 2016; Delahay, 1982; Winter et al., 2005, 2006; Seidel et al., 2011], which further allows one to determine the accurate positions of energy levels of the aqueous solution. Recent photoelectron experimental results using the microjet technique reveal that the valence $3p$ band of the solvated Cl^- anion is approximate 1.71 eV above the H_2O $1b_1$ band [Gaiduk et al., 2016].

During the process of the optical photoelectron spectroscopy experiment, a valence electron is excited to the vacuum by absorbing energy of an incident photon. The electronic levels of the solvated anion can be determined by the electron binding energy, which is equal to the difference between the excitation photon energy and the kinetic energy of the emitted electron. In theory, the electronic structure of the solvated anion can also be computed from *ab initio* methods, which requires both accurate descriptions of molecular structures and precise modeling of electronic interactions to obtain energy levels of the given molecular configurations. The calculation of energy levels demands a theory of electronic excitations. The GW approximation for the electron self-energy has proved to be an excellent tool to study the energy levels of single-particle excitations [Gaiduk et al., 2016; Hedin and Lundqvist, 1970; Chen et al., 2016; Swartz and Wu, 2013; Hybertsen and Louie, 1986] leading to more accurate energy levels in comparison with density functional theory (DFT), which is in principle a ground-state theory. The energy separation between the valence $3p$ band of the Cl^- anion and the H_2O $1b_1$ band reflects the interaction strength between the Cl^- anion and H_2O water molecules

in the solution, as the interaction depends on the hybridization of the $3p$ orbitals of the Cl^- anion with the $1b_1$ band of the H_2O water molecules. As far as the molecular structure is concerned, *ab initio* molecular dynamics (AIMD) simulation has proven to be a powerful tool to study the structure of pure water [Laasonen et al., 1993b; Tuckerman et al., 1995] and aqueous ionic solutions [Laasonen and Klein, 1997; Tobias et al., 2001; Ikeda et al., 2003; Heuft and Meijer, 2003; Kulik et al., 2010; Adriaanse et al., 2012; Ge et al., 2013; Zhang et al., 2013; Bankura et al., 2013; DelloStritto et al., 2020]. In AIMD, the atomic forces, which are needed to propagate the dynamics, are computed using DFT without the need for any empirical input. However, the DFT method faces its own challenges. The general gradient approximation (GGA) exchange-correlation (XC) functional generally gives an overstructured liquid water due to the self-interaction error [Perdew et al., 1996a; Sa\lek et al., 2005; Cohen et al., 2008, 2012]. The overestimated interaction between the Cl^- anion and the water molecules predicted by the PBE XC functional exaggerates the hybridization between the $3p$ orbital of the Cl^- anion with surrounding water molecules as well. In order to accurately determine the structure at the molecular level, one needs to employ higher level XC functionals. Hybrid functionals [Becke, 1993a], which include a fraction of exact exchange, reduce the self-interaction error presenting in GGAs. It has been proven that hybrid functionals, like PBE0 (containing 25% of exact exchange) [Perdew et al., 1996b; Adamo and Barone, 1999], lower the probability of hydrogen atoms being donated to the neighboring water molecules. Furthermore, the covalency of the water molecules is strengthened with the PBE0 functional, leading to a shorter OH bond with weakened directional hydrogen bonds [DiStasio et al., 2014]. Thus,

the PBE0 functional can give a more physical molecular structure, which predicts a larger Cl-O distance and weaker interaction between the Cl^- anion and water molecules, than that in PBE [Gaiduk et al., 2014; Bankura et al., 2015]. Moreover, it is found that van der Waals interactions are crucial to obtain accurate aqueous molecular structure as these non-directional attractive forces not only soften the water structure but also yield the qualitatively correct density [Bankura et al., 2015; DiStasio et al., 2014]. Finally, meta-GGA functionals, like SCAN [DelloStritto et al., 2020; Sun et al., 2015; Chen et al., 2017], can predict an accurate molecular structure, comparable to hybrid functionals [Bankura et al., 2015; Sun et al., 2016; Horn et al., 2016], at less computational cost, since it reduces the self-interaction error and includes intermediate range interactions. In the work of Galli and coauthors [Gaiduk et al., 2016], the molecular structures are provided by the hybrid XC PBE0 functional, while the electronic structure uses a one-shot G_0W_0 method on top of self-consistent hybrid wavefunction. In their calculation, the valence $3p$ band of the Cl^- anion is around 1.52 eV above the H_2O $1b_1$ band, while the corresponding experimental value is 1.71 eV. However, the Cl-O distance predicted by PBE0 [Gaiduk et al., 2014; Bankura et al., 2015] is still smaller than the experimental value, indicating the interaction between the hydrated ion and water is likely still overestimated. This leads to a smaller energy separation between the Cl^- ($3p$) and H_2O $1b_1$ bands compared to the experimental value [Gaiduk et al., 2016].

The remaining discrepancy between experiment and theory indicates that molecular modeling of the aqueous Cl^- anion solution is still not accurate enough. As discussed in chapter 6, we find that NQEs introduce non-trivial changes to the

hydrogen bonding between the chloride anion and the water molecules, as well as to the chloride hydration structure, resulting in a better fit to experimental observations [Xu et al., 2020]. Therefore, we would expect that a proper treatment of NQEs in the Cl^- anion aqueous solution will further soften the solvation structure and weaken the interactions between the Cl^- anion and water molecules, thus increasing the energy separation between the Cl^- ($3p$) and H_2O ($1b_1$) bands and pushing it closer to the experimental values.

In this chapter, we present a comprehensive computational study combining the molecular structure and electronic structure of chloride aqueous solutions. Beyond DFT, the electronic structure calculation is performed by using the GW approximation for the electron self-energy in the static limit, i.e. the static COHSEX level of theory [Hybertsen and Louie, 1986; Deslippe et al., 2012]. Our results show that NQEs significantly improve accuracy of the computed energy levels, and we find that the solvation pattern changes induced by NQEs are strongly correlated with the hybridization between the Cl^- ($3p$) and H_2O ($1b_1$) orbitals, shifting the energy separation between Cl^- ($3p$) and H_2O ($1b_1$) peaks to a larger value, which is closer to the experimental data.

7.2 Method

We adopted the same AIMD trajectories as discussed in previous section (chapter 6) Also it is important to note that previous result suggested that the absence of the Na+ cation does not change the structure of the Cl^- aqueous solution [Gaiduk et al., 2014]. The G_0W_0 calculations were performed in the static limit (static-COHSEX)[Hybertsen and Louie, 1986] on top of a PBE ground state, were the

molecular structure was obtained from either AIMD or PI-AIMD. The subsequent static-COHSEX calculations are done with the BerkeleyGW package [Hybertsen and Louie, 1986; Deslippe et al., 2012]. The details of the static-COHSEX calculation could be found in Appendix D.

7.3 Computed quasiparticle density of states

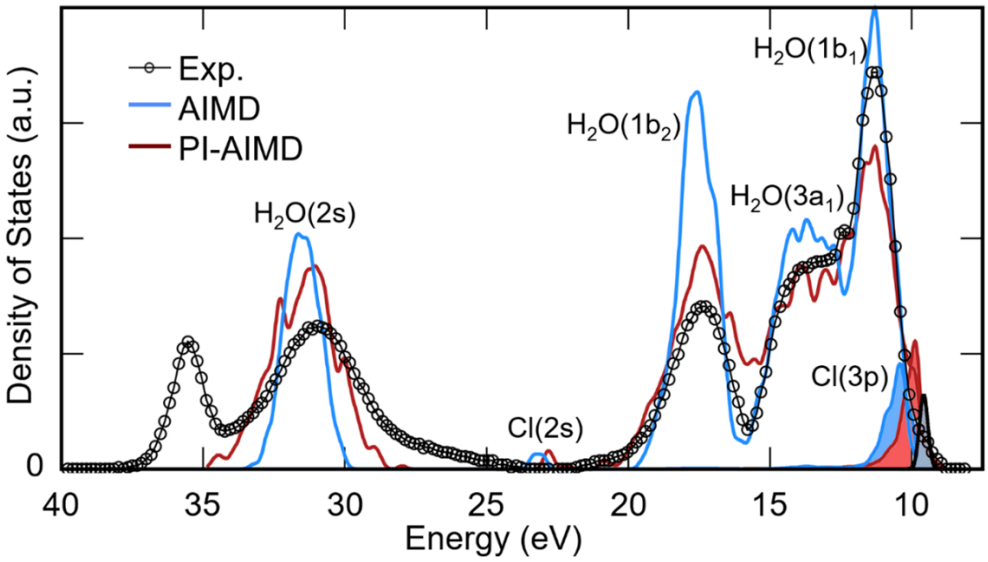

Figure 7.1: The electronic qDOS and Cl^- anion projected qDOS from AIMD (blue) and PI-AIMD (red) trajectories calculated at the static COHSEX level of theory. Experimental data (black empty circles) is taken from Ref. [Gaiduk et al., 2016]. The shaded peaks are the qDOS projected onto the Cl^- anion orbitals. Note that the experimental position of the qDOS projected onto the Cl^- anion orbital is taken from Ref. [Gaiduk et al., 2016] and the projected qDOS (grey) was constructed by a Gaussian function for comparing the position. The Cl^- anion-projected qDOS has been multiplied by a factor of 5 to be more visible. Both AIMD and PI-AIMD spectra are aligned at H_2O ($1b_1$) peak of the experimental data. All three qDOS spectra are normalized by using the peak area.

To understand the relation between molecular structure and electronic structure of the Cl^- anion aqueous solution, we computed the quasiparticle density of states (qDOS) of the Cl^- anion aqueous solution which is directly comparable to the experimental photoelectron spectrum, shown in Figure 7.1. We computed the

qDOS at the static COHSEX level of theory. The qDOS and projected qDOS for Cl^- are averaged over 8 snapshots of the molecular structure (8 independent snapshots for AIMD, 1 snapshot with 8 beads for PI-AIMD). The orbital energies of each peak in the qDOS, taken at the peak maximum, are reported in Table 7.1 along with the experimental data. Overall, the qDOS shows four main peaks related to H_2O, the lowest one is associated with the $2s$ orbital of H_2O while the other three peaks in the higher energy valence region are associated with the $1b_2$, $3a_1$, and $1b_1$ characteristics. The qDOS for the averaged structures calculated from PI-AIMD is much broader than that from classical AIMD, which is consistent with previous observations of the computed XAS spectra [Sun et al., 2018] as well as the photoemission spectroscopy qDOS spectra in pure water [Chen et al., 2016]. The PI-AIMD peak positions are also closer to the experimental values. While there is almost no difference between the peak positions of the liquid water computed from the AIMD simulation and the ones obtained from the PI-AIMD simulation, consistent with previous reports [Chen et al., 2016], surprisingly, the peak positions of the Cl^- anion, $2s$ and $3p$ orbitals, shift to higher energies, which indicates that NQEs change the hydration structure of the solvated anions. The static COHSEX calculation based on PI-AIMD trajectory predicts the energy sep-

Table 7.1: The energy separation ΔE between the peaks of H_2O ($1b_1$) and Cl^- ($3p$) in the qDOS of a 0.87 M Cl^- solution computed using many-body perturbation theory at the static COHSEX level of theory. The units are eV. The experimental data are taken from the peak positions of the photoelectron spectrum in the Ref. [Gaiduk et al., 2016]. Note that the peak energy of AIMD, PIMD are aligned at H_2O ($1b_1$) peak of the experimental data.

	$H_2O(2s)$	$H_2O(1b_2)$	$H_2O(3a_1)$	$H_2O(1b_1)$	$Cl(3p)$	ΔE
AIMD	31.57	17.62	13.69	11.31	10.42	0.89
PI-AIMD	31.08	17.40	13.86	11.31	9.90	1.41
Experimental	30.90	17.41	13.78	11.31	9.60	1.71

aration ΔE between the peak position of the Cl^- anion ($3p$) and the H_2O ($1b_1$) state to be 1.41 eV, which is much closer to the experimental value of ΔE = 1.71 eV compared to the AIMD case, which predicts $\Delta E = 0.89$ eV. To further identify where the improved prediction comes from, we compare our results with Ref. [Gaiduk et al., 2016], in which uses a G_0W_0 calculation on top of a PBE ground state, where the molecular structure was obtained from a PBE0 MD calculation. In Ref. [Gaiduk et al., 2016], they find a ΔE of 1.13 eV, which is larger than $\Delta E = 0.89$ eV obtained from our AIMD but still significantly smaller than the $\Delta E = 1.41$ eV predicted from our PI-AIMD calculation. This suggests that while using hybrid functionals to describe the molecular dynamics improves the molecular structure, NQE corrections are still necessary to obtain agreement with experiment.

7.4 Connections between molecular and electronic structures

Under the influence of NQEs, the largest change occurs in the peak position of the Cl^- state in Table 7.1, while the position of the peaks associated with water remain relatively unchanged. It raises the question of how the NQEs change the electronic structure of the solvated Cl^- anions. Previous studies have suggested that the relative positions of the orbitals associated with the solvated Cl^- anion with respect to the $1b_1$ orbital of H_2O shows a strong dependence on the corresponding hydration configurations[Bankura et al., 2015]. In other words, the spatial distances between Cl-O and Cl-H pairs shifting to slightly larger values will

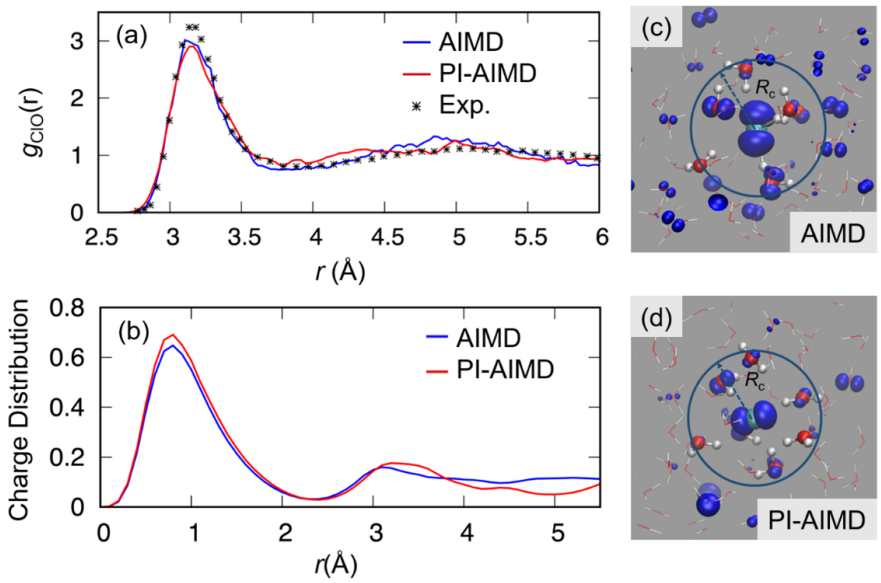

Figure 7.2: (a) The computed Cl-O radial distribution functions (RDFs) in Cl^- anion solution obtained from AIMD, PI-AIMD and the experimental neutron diffraction results [Mancinelli et al., 2007a]. (b) The charge distribution of the Cl^- $3p$ orbital in the AIMD and PI-AIMD where zero is the position of the Cl^- nucleus. The spatial distribution of the Cl^- $3p$ orbital hybridization within the anion's first hydration shell is shown in (c) at the AIMD level and in (d) at the PI-AIMD. R_c is the cutoff distance for the anion's first hydration shell. The charge density is in blue color. Note that we highlight the water molecules within the first hydration shell.

increase the energy separation between the Cl^- ($3p$) and H_2O ($1b_1$) molecules. To remind the reader, we show the Cl-O RDFs $g_{ClO}(r)$ based on the AIMD and PI-AIMD trajectories in Figure 7.2(a). In the AIMD trajectory, the center positions of both the first (3.14 Å) and second (4.91 Å) hydration shells are closer to the Cl^- anion, compared to the experimental values of 3.16 Å and 5.09 Å, respectively. With NQEs, in the PI-AIMD data, the center positions of both the first and second hydration shells are located at 3.16 Å and 5.06 Å. Thus, the PI-AIMD predicts better agreement with experimental data, in terms of both electronic structure and molecular structure.

Furthermore, we have computed the spatial distribution of the Cl^- $3p$ orbital density and plotted the results in the Figure 7.2(c) and (d). It shows that the $3p$

orbital is slightly more localized in the PI-AIMD structure than that in the AIMD structure. The computed charge distribution of the projected Cl^- $3p$ orbital in AIMD and PI-AIMD are shown in Figure 7.2(b). One can find that within the range from 0 Å to 2.3 Å, the orbital density distribution comes from the Cl^- anion itself, as evidenced by the onset of the Cl-O radial distribution function (Figure 7.2(a)). Within the 1st hydration shell (2.3 Å to 3.8 Å), the charge distribution of the $3p$ orbital is more localized in the PI-AIMD structure than in the AIMD structure. Beyond 1st hydration shell (¿ 3.8 Å), the density distribution of the $3p$ orbital decays quickly in the PI-AIMD structure, while it does not change in the AIMD structure (Figure 7.2(b)). This fast decay behavior in the PI-AIMD structure further indicates that the hybridization of $3p$ orbital is less favorable in the PI-AIMD structure than in the AIMD structure, leading to a larger energy separation between H_2O ($1b_1$) band and Cl^- ($3p$) band.

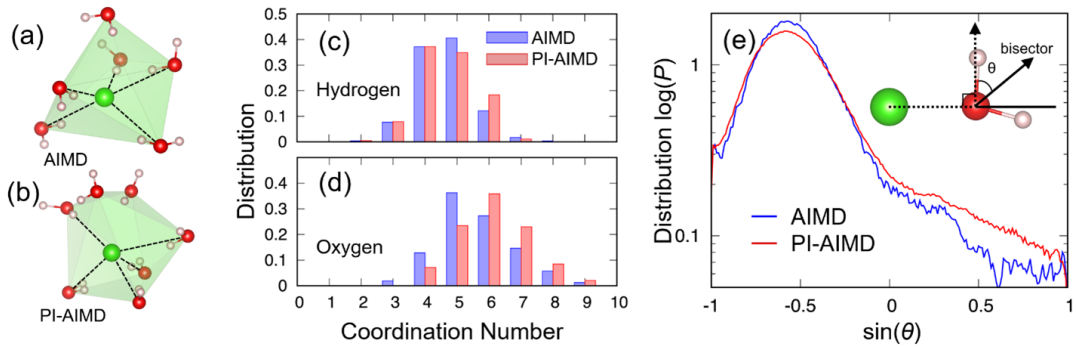

Figure 7.3: Schematics of the bonded (dashed line) and non-bonded water molecules within the first hydration shell in AIMD (a) and PI-AIMD (b). The coordination number of hydrogen (c) and oxygen (d) atoms within the first hydration shell of AIMD (blue) and PI-AIMD (red). (e) The angle distribution (P) of water molecules within the first hydration shell. The angle is defined between the bisector and the perpendicular of the line from the Cl to O atoms. Note that $sin\theta$ <0 means hydrogen atoms point towards to Cl^- anions while $sin\theta$ >0 means hydrogen atoms point away from Cl^- anions.

The energy separation resulting from the hybridization of the Cl^- $3p$ electron

with water comes from the weakened anion-water interaction under the increased distance between the Cl and O atoms, but how do the changes of the solution pattern around the Cl^- anions due to NQEs increase the distance? The polarizable Cl^- anion in the solution makes the surrounding water molecules tend to populate one side of the anion and leave the other side relatively empty [Ohtaki and Radnai, 1993; Tobias et al., 2001; Ge et al., 2013; DelloStritto et al., 2020; Xu et al., 2020; Migliorati et al., 2014; Perera and Berkowitz, 1992]. We calculated the number of water molecules that are either bonded or non-bonded to the Cl^- anion in both the AIMD and PI-AIMD structures. The average number of bonded water molecules within the first hydration shell of the Cl^- anion decreases from 4.89 in the AIMD structure to 4.71 in the PI-AIMD structure, while the average number of the non-bonded water molecules increases from 1.73 in AIMD to 2.37 in PI-AIMD. Typically, we find that within the 1st hydration shell, the most common configuration is 5 bonded water molecules with 1 non-bonded water molecule in the AIMD structure, and 5 bonded water molecules with 2 non-bonded water molecules in the PI-AIMD structure. In Figure 7.3(a) and (b), we present the schematics for the typical configurations in AIMD and PI-AIMD structures. The increase of the non-bonded water molecules observed in PI-AIMD indicates that water molecules are less bonded with the Cl^- anion than with other water molecules, which leads to further configuration changes. We computed the coordination number distribution of O and H in the first hydration shell of the Cl^- anion based on AIMD and PI-AIMD trajectories. The results are shown in Figure 7.3(c) and (d). The center of the distribution of the oxygen coordination number is 5 in AIMD and shifts to 6 in PI-AIMD, while both PI-AIMD and AIMD

share a similar hydrogen coordination number of 5. This indicates that under the influence of NQEs, more oxygen sites of water molecules tend to stay in the first hydration shell, with the hydrogen atoms pointing away from Cl^- anion. These behaviors are further revealed by the angle distribution of the water molecules as shown in Figure 7.3(e), where the angle θ is defined between the bisector and the perpendicular of the line from Cl to O atoms. Note that $sin\theta$ <0 means hydrogen atoms point towards the Cl^- anions while $sin\theta$ >0 means hydrogen atoms point away from Cl^- anions. One can tell that the population of water molecules with hydrogen pointing away from the Cl is more prominent in the PI-AIMD structure than in the AIMD structure.

Finally, in order to understand how the aforementioned solvation pattern changes influence the energy separation between the Cl^- ($3p$) and H_2O ($1b_1$) orbitals, we computed the energy separation between the projected qDOS peak positions of the Cl^- anion and the H_2O ($1b_1$) orbitals coming from water molecules bonded to the Cl^- anion, $\Delta E_{\text{bonded}} = E(\text{H}_2\text{O}_{(\text{bonded}}(1b_1))$ - $E(\text{Cl}^-(3p))$, verses non-bonded water molecules, $\Delta E_{\text{bonded}} = E(\text{H}_2\text{O}_{(\text{non-bonded}}(1b_1))$ - $E(\text{Cl}^-(3p))$. Both calculations consider only water molecules within the 1st hydration shell of Cl^- anion based on the AIMD and PI-AIMD trajectories. We find that on average, in the AIMD case, $\Delta E_{\text{non-bonded}} = 0.7 \pm 0.3$ eV and $\Delta E_{\text{bonded}} = 0.6 \pm 0.2$ eV; however, under the influence of NQEs, the energy separation between the non-bonded water and Cl^- anion increases to $\Delta E_{\text{non-bonded}} = 1.2 \pm 0.3$ eV, while $\Delta E_{\text{bonded}} = 0.6 \pm 0.3$ eV. It is clear that the increased energy separation between the $3p$ states of hydrated Cl^- and the $1b_1$ states of liquid water comes from two aspects: first, the energy separation for the non-bonded water molecules and Cl^- anion

in the PI-AIMD simulation is larger than the one in the AIMD simulation due to the NQEs; second, the fraction of non-bonded water molecules within the 1st hydration shell increases in the PI-AIMD simulation comparing to that in the AIMD simulation. The connection between the structural change and electronic structure of the Cl^- anion can be summarized as follows: hydrogen atoms are less attracted by the Cl^- anion and tend to point away from the Cl^- anion under the influence of NQEs. Thus, NQEs increase the distance between the Cl and O atoms, as well as the number of non-bonded water molecules to the Cl anion and the energy separation $\Delta E_{\text{non-bonded}}$. Furthermore, more water molecules are able to bond with other water molecules instead of the Cl^- anion. All these lead to less hybridization of the $3p$ orbital of the Cl^- anion with the water molecules and increases the energy separation between the Cl^- ($3p$) band and the H_2O ($1b_1$) band.

7.5 Conclusion

In conclusion, we present a comprehensive computational study and investigate the connection between molecular structure and electronic structure of an aqueous solution of Cl^- anions. NQEs have a strong influence on the hydration structure of the Cl^- anion. The computed energy levels of the aqueous solution of Cl^- anions based on a PI-AIMD trajectory show good agreement with the photoemission spectroscopy experimental data. The energy separation between the Cl^- $3p$ orbital and the H_2O $1b_1$ orbital predicted by a PI-AIMD simulation with electronic structure treated at the static COHSEX level of theory is 1.41 eV, which is in good agreement with the experimental value of 1.71 eV [Gaiduk et al.,

2016]. Our results show that NQEs play an important role not only in modeling the molecular structure but also in capturing the electronic structure of Cl^- anion solution. This result again emphasizes the importance of including NQEs in the further study on the Hofmeister series ionic solution.

BIBLIOGRAPHY

Abadi, M., Barham, P., Chen, J., Chen, Z., Davis, A., Dean, J., Devin, M., Ghemawat, S., Irving, G., Isard, M., and *et al.* (2016). TensorFlow: A System for Large-Scale Machine Learning. pages 265–283.

Adamo, C. and Barone, V. (1999). Toward reliable density functional methods without adjustable parameters: The PBE0 model. *J. Chem. Phys.*, 110(13):6158–6170.

Adriaanse, C., Cheng, J., Chau, V., Sulpizi, M., Vandevondele, J., and Sprik, M. (2012). Aqueous redox chemistry and the electronic band structure of liquid water. *J. Phys. Chem. Lett.*, 3(23):3411–3415.

Amann-Winkel, K., Bellissent-Funel, M.-C., Bove, L. E., Loerting, T., Nilsson, A., Paciaroni, A., Schlesinger, D., and Skinner, L. (2016). X-ray and Neutron Scattering of Water. *Chem. Rev.*, 116(13):7570–7589.

Auer, B., Kumar, R., Schmidt, J. R., and Skinner, J. L. (2007). Hydrogen bonding and Raman, IR, and 2D-IR spectroscopy of dilute HOD in liquid D2O. *Proc. Natl. Acad. Sci. U.S.A.*, 104(36):14215–14220.

Bader, J. S. and Berne, B. J. (1994). Quantum and classical relaxation rates from classical simulations. *J. Chem. Phys.*, 100(11):8359–8366.

Badyal, Y. S., Saboungi, M.-L., Price, D. L., Shastri, S. D., Haeffner, D. R., and Soper, A. K. (2000). Electron distribution in water. *J. Chem. Phys.*, 112(21):9206–9208.

Ball, P. (2008). Water as an Active Constituent in Cell Biology. *Chem. Rev.*, 108(1):74–108.

Bankura, A., Carnevale, V., and Klein, M. L. (2013). Hydration structure of salt solutions from *ab initio* molecular dynamics. *J. Chem. Phys.*, 138(1):014501.

Bankura, A., Santra, B., DiStasio, R. A., Swartz, C. W., Klein, M. L., and Wu, X. (2015). A systematic study of chloride ion solvation in water using van der Waals inclusive hybrid density functional theory. *Mol. Phys.*, 113(17-18):2842–2854.

Becke, A. D. (1988). Density-functional exchange-energy approximation with correct asymptotic behavior. *Phys. Rev. A*, 38(6):3098–3100.

Becke, A. D. (1993a). Density-functional thermochemistry. III. The role of exact exchange. *J. Chem. Phys.*, 98(7):5648–5652. ISBN: 0021-9606.

Becke, A. D. (1993b). A new mixing of Hartree–Fock and local density-functional theories. *The Journal of Chemical Physics*, 98(2):1372–1377.

Beekman, H. E., Eggenkamp, H. G., and Appelo, C. A. (2011). An integrated modelling approach to reconstruct complex solute transport mechanisms - Cl and δ37Cl in pore water of sediments from a former brackish lagoon in The Netherlands. *Appl. Geochemistry*, 26(3):257–268. Publisher: Elsevier Ltd.

Bellissent-Funel, M.-C., Hassanali, A., Havenith, M., Henchman, R., Pohl, P., Sterpone, F., van der Spoel, D., Xu, Y., and Garcia, A. E. (2016). Water Determines the Structure and Dynamics of Proteins. *Chem. Rev.*, 116(13):7673–7697.

Benedict, W. S., Gailar, N., and Plyler, E. K. (1956). Rotation-Vibration Spectra of Deuterated Water Vapor. *J. Chem. Phys.*, 24(6):1139–1165.

Bernasconi, M., Chiarotti, G. L., Focher, P., Scandolo, S., Tosatti, E., and Parrinello, M. (1995). First-principle-constant pressure molecular dynamics. *J. Phys. Chem. Solids*, 56(3):501–505.

Bernath, P. F. (2015). *Spectra of Atoms and Molecules*. Oxford University Press.

Bezanilla, F. (2008). How membrane proteins sense voltage. *Nat. Rev. Mol. Cell Biol.*, 9(4):323–332.

Born, M. and Oppenheimer, R. (1927). Zur Quantentheorie der Molekeln. *Ann. Phys.*, 389(20):457–484.

Brubach, J.-B., Mermet, A., Filabozzi, A., Gerschel, A., and Roy, P. (2005). Signatures of the hydrogen bonding in the infrared bands of water. *J. Chem. Phys.*, 122(18):184509.

Cao, J. and Voth, G. A. (1994). The formulation of quantum statistical mechanics based on the Feynman path centroid density. II. Dynamical properties. *J. Chem. Phys.*, 100(7):5106–5117.

Car, R. and Parrinello, M. (1985). Unified approach for molecular dynamics and density-functional theory. *Phys. Rev. Lett.*, 55(22):2471.

Ceriotti, M., Bussi, G., and Parrinello, M. (2009a). Langevin Equation with Colored Noise for Constant-Temperature Molecular Dynamics Simulations. *Phys. Rev. Lett.*, 102(2):020601.

Ceriotti, M., Bussi, G., and Parrinello, M. (2009b). Nuclear Quantum Effects in Solids Using a Colored-Noise Thermostat. *Phys. Rev. Lett.*, 103(3).

Ceriotti, M., Bussi, G., and Parrinello, M. (2010a). Colored-Noise Thermostats à la Carte. *J. Chem. Theory Comput.*, 6(4):1170–1180.

Ceriotti, M., Cuny, J., Parrinello, M., and Manolopoulos, D. E. (2013). Nuclear quantum effects and hydrogen bond fluctuations in water. *Proc. Natl. Acad. Sci. U.S.A.*, 110(39):15591–15596.

Ceriotti, M., Fang, W., Kusalik, P. G., McKenzie, R. H., Michaelides, A., Morales, M. A., and Markland, T. E. (2016). Nuclear Quantum Effects in Water and Aqueous Systems: Experiment, Theory, and Current Challenges. *Chem. Rev.*, 116(13):7529–7550.

Ceriotti, M. and Manolopoulos, D. E. (2012). Efficient First-Principles Calculation of the Quantum Kinetic Energy and Momentum Distribution of Nuclei. *Phys. Rev. Lett.*, 109(10).

Ceriotti, M., More, J., and Manolopoulos, D. E. (2014). i-PI: A Python interface for ab initio path integral molecular dynamics simulations. *Comput. Phys. Commun.*, 185(3):1019–1026.

Ceriotti, M., Parrinello, M., Markland, T. E., and Manolopoulos, D. E. (2010b). Efficient stochastic thermostatting of path integral molecular dynamics. *J. Chem. Phys.*, 133(12):124104.

Chau, P.-L. and Hardwick, A. J. (1998). A new order parameter for tetrahedral configurations. *Mol. Phys.*, 93(3):511–518.

Chen, M., Ko, H.-Y., Remsing, R. C., Calegari Andrade, M. F., Santra, B., Sun, Z., Selloni, A., Car, R., Klein, M. L., Perdew, J. P., and Wu, X. (2017). Ab initio theory and modeling of water. *Proc. Natl. Acad. Sci. U.S.A.*, 114(41):10846–10851.

Chen, M., Zheng, L., Santra, B., Ko, H.-Y., Jr, R. A. D., Klein, M. L., Car, R., and Wu, X. (2018). Hydroxide diffuses slower than hydronium in water because its solvated structure inhibits correlated proton transfer. *Nat. Chem.*, 10(4):413.

Chen, W., Ambrosio, F., Miceli, G., and Pasquarello, A. (2016). *Ab initio* Electronic Structure of Liquid Water. *Phys. Rev. Lett.*, 117(18).

Chen, W., Sharma, M., Resta, R., Galli, G., and Car, R. (2008). Role of dipolar correlations in the infrared spectra of water and ice. *Phys. Rev. B*, 77(24):245114.

Chen, W., Wu, X., and Car, R. (2010). X-Ray Absorption Signatures of the Molecular Environment in Water and Ice. *Phys. Rev. Lett.*, 105(1).

Cheng, B., Engel, E. A., Behler, J., Dellago, C., and Ceriotti, M. (2019). Ab initio thermodynamics of liquid and solid water. *Proc. Natl. Acad. Sci. U.S.A.*, 116(4):1110–1115.

Cohen, A. J., Mori-Sánchez, P., and Yang, W. (2008). Insights into Current Limitations of Density Functional Theory. *Science*, 321(5890):792–794.

Cohen, A. J., Mori-Sánchez, P., and Yang, W. (2012). Challenges for density functional theory. *Chem. Rev.*, 112(1):289–320.

Company, C. R. and Lide, D. R., editors (2003). *CRC handbook of chemistry and physics: a ready-reference book of chemical and physical data*. CRC Press, Boca Raton, 84th ed edition. OCLC: 249116497.

Cook, R. L., De Lucia, F. C., and Helminger, P. (1974). Molecular force field and structure of water: Recent microwave results. *J. Mol. Spectrosc.*, 53(1):62–76.

Copestake, A. P., Neilson, G. W., and Enderby, J. E. (1985). The structure of a highly concentrated aqueous solution of lithium chloride. *J. Phys. C Solid State Phys.*, 18(22):4211–4216. Publisher: IOP Publishing.

Craig, I. R. and Manolopoulos, D. E. (2004). Quantum statistics and classical mechanics: Real time correlation functions from ring polymer molecular dynamics. *J. Chem. Phys.*, 121(8):3368–3373.

Cummings, S., Enderby, J. E., Neilson, G. W., Newsome, J. R., Howe, R. A., Howells, W. S., and Soper, A. K. (1980). Chloride ions in aqueous solutions. *Nature*, 287(5784):714–716.

Dang, L. X., Schenter, G. K., Glezakou, V.-A., and Fulton, J. L. (2006). Molecular Simulation Analysis and X-ray Absorption Measurement of Ca^{2+}, K^{+} and Cl^{-} Ions in Solution. *J. Phys. Chem. B*, 110(47):23644–23654.

Del Ben, M., Hutter, J., and VandeVondele, J. (2015). Probing the structural and dynamical properties of liquid water with models including non-local electron correlation. *J. Chem. Phys.*, 143(5):054506.

Delahay, P. (1982). Photoelectron Emission Spectroscopy of Aqueous Solutions. *Acc. Chem. Res.*, 15:40–45.

DelloStritto, M., Xu, J., Wu, X., and Klein, M. L. (2020). Aqueous solvation of the chloride ion revisited with density functional theory: impact of correlation and exchange approximations. *Phys. Chem. Chem. Phys.*

Deslippe, J., Samsonidze, G., Strubbe, D. A., Jain, M., Cohen, M. L., and Louie, S. G. (2012). BerkeleyGW: A massively parallel computer package for the calculation of the quasiparticle and optical properties of materials and nanostructures. *Computer Physics Communications*, 183(6):1269–1289.

Dirac, P. a. M. (1930). Note on Exchange Phenomena in the Thomas Atom. *Mathematical Proceedings of the Cambridge Philosophical Society*, 26(3):376–385. Publisher: Cambridge University Press.

DiStasio, R. A., Santra, B., Li, Z., Wu, X., and Car, R. (2014). The individual and collective effects of exact exchange and dispersion interactions on the *ab initio* structure of liquid water. *J. Chem. Phys.*, 141(8):084502.

Duboué-Dijon, E. and Laage, D. (2015). Characterization of the Local Structure in Liquid Water by Various Order Parameters. *J. Phys. Chem. B*, 119(26):8406–8418.

Eisenberg, D. S. and Kauzmann, W. (2005). *The structure and properties of water.* Oxford classic texts in the physical sciences. Clarendon Press; Oxford University Press, Oxford; New York.

Fecko, C. J., Eaves, J. D., Loparo, J. J., Tokmakoff, A., and Geissler, P. L. (2003). Ultrafast Hydrogen-Bond Dynamics in the Infrared Spectroscopy of Water. *Science*, 301(5640):1698–1702.

Fersht, A. R., Shi, J.-P., Knill-Jones, J., Lowe, D. M., Wilkinson, A. J., Blow, D. M., Brick, P., Carter, P., Waye, M. M. Y., and Winter, G. (1985). Hydrogen bonding and biological specificity analysed by protein engineering. *Nature*, 314(6008):235–238.

Feynman, R. P. (1939). Forces in Molecules. *Phys. Rev.*, 56(4):340–343.

Feynman, R. P. and Hibbs, A. R. (1965). *Quantum mechanics and path integrals*. International series in pure and applied physics. McGraw-Hill, New York, NY. OCLC: 987995.

Foster, K. L., Plastridge, R. A., Bottenheim, J. W., Shepson, P. B., Finlayson-Pitts, B. J., and Spicer, C. W. (2001). The role of Br2 and Brcl in surface ozone destruction at polar sunrise. *Science (80-.)*., 291(5503):471–474.

Franks, F. (2007). *Water: A Matrix of Life*. Royal Society of Chemistry.

Fransson, T., Harada, Y., Kosugi, N., Besley, N. A., Winter, B., Rehr, J. J., Pettersson, L. G. M., and Nilsson, A. (2016). X-ray and Electron Spectroscopy of Water. *Chem. Rev.*, 116(13):7551–7569.

Funkner, S., Niehues, G., Schmidt, D. A., Heyden, M., Schwaab, G., Callahan, K. M., Tobias, D. J., and Havenith, M. (2012). Watching the Low-Frequency Motions in Aqueous Salt Solutions: The Terahertz Vibrational Signatures of Hydrated Ions. *J. Am. Chem. Soc.*, 134(2):1030–1035.

Furness, J. W., Kaplan, A. D., Ning, J., Perdew, J. P., and Sun, J. (2020). Accurate and Numerically Efficient r2SCAN Meta-Generalized Gradient Approximation. *J. Phys. Chem. Lett.*, 11(19):8208–8215. Publisher: American Chemical Society.

Gaiduk, A. P. and Galli, G. (2017). Local and Global Effects of Dissolved Sodium Chloride on the Structure of Water. *J. Phys. Chem. Lett.*, 8(7):1496–1502.

Gaiduk, A. P., Govoni, M., Seidel, R., Skone, J. H., Winter, B., and Galli, G. (2016). Photoelectron Spectra of Aqueous Solutions from First Principles. *J. Am. Chem. Soc.*, 138(22):6912–6915.

Gaiduk, A. P., Gygi, F., and Galli, G. (2015). Density and Compressibility of Liquid Water and Ice from First-Principles Simulations with Hybrid Functionals. *J. Phys. Chem. Lett.*, 6(15):2902–2908.

Gaiduk, A. P., Zhang, C., Gygi, F., and Galli, G. (2014). Structural and electronic properties of aqueous NaCl solutions from ab initio molecular dynamics simulations with hybrid density functionals. *Chem. Phys. Lett.*, 604:89–96.

Gasparotto, P., Hassanali, A. A., and Ceriotti, M. (2016). Probing Defects and Correlations in the Hydrogen-Bond Network of ab Initio Water. *J. Chem. Theory Comput.*, 12(4):1953–1964.

Ge, L., Bernasconi, L., and Hunt, P. (2013). Linking electronic and molecular structure: insight into aqueous chloride solvation. *Phys. Chem. Chem. Phys.*, 15(31):13169.

Ghosal, S. (2005). Electron Spectroscopy of Aqueous Solution Interfaces Reveals Surface Enhancement of Halides. *Science*, 307(5709):563–566.

Giannozzi, P., Andreussi, O., Brumme, T., Bunau, O., Buongiorno Nardelli, M., Calandra, M., Car, R., Cavazzoni, C., Ceresoli, D., Cococcioni, M., Colonna, N., Carnimeo, I., Dal Corso, A., de Gironcoli, S., Delugas, P., DiStasio, R. A., Ferretti, A., Floris, A., Fratesi, G., Fugallo, G., Gebauer, R., Gerstmann, U., Giustino, F., Gorni, T., Jia, J., Kawamura, M., Ko, H.-Y., Kokalj, A., Küçükbenli, E., Lazzeri, M., Marsili, M., Marzari, N., Mauri, F., Nguyen, N. L., Nguyen, H.-V., Otero-de-la Roza, A., Paulatto, L., Poncé, S., Rocca, D., Sabatini, R., Santra, B., Schlipf, M., Seitsonen, A. P., Smogunov, A., Timrov, I., Thonhauser, T., Umari, P., Vast, N., Wu, X., and Baroni, S. (2017). Advanced capabilities for materials modelling with Quantum ESPRESSO. *J. Phys. Condens. Matter*, 29(46):465901.

Giannozzi, P., Baroni, S., Bonini, N., Calandra, M., Car, R., Cavazzoni, C., Ceresoli, D., Chiarotti, G. L., Cococcioni, M., Dabo, I., Corso, A. D., Gironcoli, S. d., Fabris, S., Fratesi, G., Gebauer, R., Gerstmann, U., Gougoussis, C., Kokalj, A., Lazzeri, M., Martin-Samos, L., Marzari, N., Mauri, F., Mazzarello, R., Paolini, S., Pasquarello, A., Paulatto, L., Sbraccia, C., Scandolo, S., Sclauzero, G., Seitsonen, A. P., Smogunov, A., Umari, P., and Wentzcovitch, R. M. (2009). QUANTUM ESPRESSO: a modular and open-source software project for quantum simulations of materials. *J. Phys. Condens. Matter*, 21(39):395502.

Gillan, M. J., Alfè, D., and Michaelides, A. (2016). Perspective: How good is DFT for water? *J. Chem. Phys.*, 144(13):130901. Publisher: American Institute of Physics.

Guardia, E., Skarmoutsos, I., and Masia, M. (2009). On Ion and Molecular Polarization of Halides in Water. *J. Chem. Theory Comput.*, 5(6):1449–1453. WOS:000266865000001.

Guillot, B. (1991). A molecular dynamics study of the far infrared spectrum of liquid water. *J. Chem. Phys.*, 95(3):1543–1551.

Guillot, B. and Guissani, Y. (1998). Quantum effects in simulated water by the Feynman–Hibbs approach. *J. Chem. Phys.*, 108(24):10162–10174.

Habershon, S., Manolopoulos, D. E., Markland, T. E., and Miller, T. F. (2013). Ring-Polymer Molecular Dynamics: Quantum Effects in Chemical Dynamics from Classical Trajectories in an Extended Phase Space. *Annu. Rev. Phys.*, 64(1):387–413.

Hamann, D. R. (2013). Optimized norm-conserving Vanderbilt pseudopotentials. *Phys. Rev. B*, 88(8):085117.

Hamann, D. R., Schlüter, M., and Chiang, C. (1979). Norm-Conserving Pseudopotentials. *Phys. Rev. Lett.*, 43(20):1494–1497.

Harris, F. J. (1978). On the use of windows for harmonic analysis with the discrete Fourier transform. *Proc. IEEE*, 66(1):51–83.

Hartree, D. R. and Hartree, W. (1935). Self-consistent field, with exchange, for beryllium. *Proceedings of the Royal Society of London. Series A - Mathematical and Physical Sciences*, 150(869):9–33. Publisher: Royal Society.

Hedin, L. (1965). New Method for Calculating the One-Particle Green's Function with Application to the Electron-Gas Problem. *Phys. Rev.*, 139(3A):A796–A823.

Hedin, L. and Lundqvist, S. (1970). Effects of electron-electron and electron-phonon interactions on the one-electron states of solids. In Seitz, F., Turnbull, D., and Ehrenreich, H., editors, *Solid State Physics*, pages 1–181. Academic Press.

Hermann, J., DiStasio, R. A., and Tkatchenko, A. (2017). First-Principles Models for van der Waals Interactions in Molecules and Materials: Concepts, Theory, and Applications. *Chem. Rev.*, 117(6):4714–4758.

Hetényi, B., De Angelis, F., Giannozzi, P., and Car, R. (2004). Calculation of near-edge x-ray-absorption fine structure at finite temperatures: Spectral signatures of hydrogen bond breaking in liquid water. *J. Chem. Phys.*, 120(18):8632–8637.

Heuft, J. M. and Meijer, E. J. (2003). Density functional theory based molecular-dynamics study of aqueous chloride solvation. *J. Chem. Phys.*, 119(22):11788–11791.

Hofmeister, F. (1888). Zur Lehre von der Wirkung der Salze. *Archiv für experimentelle Pathologie und Pharmakologie*, 25(1):1–30.

Hohenberg, P. and Kohn, W. (1964). Inhomogeneous Electron Gas. *Phys. Rev.*, 136(3B):B864–B871.

Hoover, W. G. (1985). Canonical dynamics: Equilibrium phase-space distributions. *Phys. Rev. A*, 31(3):1695–1697.

Horn, P. R., Mao, Y., and Head-Gordon, M. (2016). Probing non-covalent interactions with a second generation energy decomposition analysis using absolutely localized molecular orbitals. *Phys. Chem. Chem. Phys.*, 18(33):23067–23079. ISBN: 5106431255.

Hunter, K. M., Shakib, F. A., and Paesani, F. (2018). Disentangling Coupling Effects in the Infrared Spectra of Liquid Water. *J. Phys. Chem. B*, 122(47):10754–10761.

Hybertsen, M. S. and Louie, S. G. (1986). Electron correlation in semiconductors and insulators: Band gaps and quasiparticle energies. *Phys. Rev. B*, 34(8):5390–5413.

Ikeda, T., Hirata, M., and Kimura, T. (2003). Ab initio molecular dynamics study of polarization effects on ionic hydration in aqueous AlCl3 solution. *J. Chem. Phys.*, 119(23):12386–12392.

Jang, S. and Voth, G. A. (1999). A derivation of centroid molecular dynamics and other approximate time evolution methods for path integral centroid variables. *J. Chem. Phys.*, 111(6):2371–2384.

Jentsch, T. J., Stein, V., Weinreich, F., and Zdebik, A. A. (2002). Molecular Structure and Physiological Function of Chloride Channels. *Physiol. Rev.*, 82(2):503–568.

Kang, W. and Hybertsen, M. S. (2010). Enhanced static approximation to the electron self-energy operator for efficient calculation of quasiparticle energies. *Phys. Rev. B*, 82(19):195108.

Kapil, V., Rossi, M., Marsalek, O., Petraglia, R., Litman, Y., Spura, T., Cheng, B., Cuzzocrea, A., Meißner, R. H., Wilkins, D. M., Helfrecht, B. A., Juda, P., Bienvenue, S. P., Fang, W., Kessler, J., Poltavsky, I., Vandenbrande, S., Wieme, J., Corminboeuf, C., Kühne, T. D., Manolopoulos, D. E., Markland, T. E., Richardson, J. O., Tkatchenko, A., Tribello, G. A., Van Speybroeck, V., and Ceriotti, M. (2019). i-PI 2.0: A universal force engine for advanced molecular simulations. *Comput. Phys. Commun.*, 236:214–223.

Kim, K. H., Späh, A., Pathak, H., Perakis, F., Mariedahl, D., Amann-Winkel, K., Sellberg, J. A., Lee, J. H., Kim, S., Park, J., Nam, K. H., Katayama, T., and Nilsson, A. (2017). Maxima in the thermodynamic response and correlation functions of deeply supercooled water. *Science*, 358(6370):1589–1593.

King-Smith, R. D. and Vanderbilt, D. (1993). Theory of polarization of crystalline solids. *Phys. Rev. B*, 47(3):1651–1654.

Kingma, D. P. and Ba, J. (2014). Adam: A Method for Stochastic Optimization. *arXiv:1412.6980 [cs]*. arXiv: 1412.6980.

Kingma, D. P. and Ba, J. (2017). Adam: A Method for Stochastic Optimization. *arXiv:1412.6980*.

Klingshirn, C. F. (2005). *Semiconductor optics*. Springer, Berlin ; New York.

Knipping, E. M. (2000). Experiments and Simulations of Ion-Enhanced Interfacial Chemistry on Aqueous NaCl Aerosols. *Science*, 288(5464):301–306.

Ko, H.-Y., Zhang, L., Santra, B., Wang, H., E, W., DiStasio Jr, R. A., and Car, R. (2019). Isotope effects in liquid water via deep potential molecular dynamics. *Mol. Phys.*, 117(22):3269–3281.

Kohn, W. and Sham, L. J. (1965). Self-Consistent Equations Including Exchange and Correlation Effects. *Phys. Rev.*, 140(4A):A1133–A1138.

Kong, L., Wu, X., and Car, R. (2012). Roles of quantum nuclei and inhomogeneous screening in the x-ray absorption spectra of water and ice. *Phys. Rev. B*, 86(13).

Kulik, H. J., Marzari, N., Correa, A. A., Prendergast, D., Schwegler, E., and Galli, G. (2010). Local Effects in the X-ray Absorption Spectrum of Salt Water. *J. Phys. Chem. B*, 114(29):9594–9601.

Kushner, D. J., Baker, A., and Dunstall, T. G. (1999). Pharmacological uses and perspectives of heavy water and deuterated compounds. *Can. J. Physiol. Pharmacol.*, 77(2):79–88.

Laage, D. and Hynes, J. T. (2008). On the Molecular Mechanism of Water Reorientation. *J. Phys. Chem. B*, 112(45):14230–14242.

Laasonen, K., Csajka, F., and Parrinello, M. (1992). Water dimer properties in the gradient-corrected density functional theory. *Chem. Phys. Lett.*, 194(3):172–174.

Laasonen, K., Parrinello, M., Car, R., Lee, C., and Vanderbilt, D. (1993a). Structures of small water clusters using gradient-corrected density functional theory. *Chem. Phys. Lett.*, 207(2-3):208–213.

Laasonen, K., Sprik, M., Parrinello, M., and Car, R. (1993b). "Ab initio" liquid water. *J. Chem. Phys.*, 99(11):9080–9089. Publisher: American Institute of Physics.

Laasonen, K. E. and Klein, M. L. (1997). *Ab Initio* Study of Aqueous Hydrochloric Acid. *J. Phys. Chem. A*, 101(1):98–102.

Leberman, R. and Soper, A. K. (1995). Effect of high salt concentrations on water structure. *Nature*, 378(6555):364.

Lee, C., Yang, W., and Parr, R. G. (1988). Development of the Colle-Salvetti correlation-energy formula into a functional of the electron density. *Phys. Rev. B*, 37(2):785–789.

Li, X.-Z., Walker, B., and Michaelides, A. (2011). Quantum nature of the hydrogen bond. *Proc. Natl. Acad. Sci. U.S.A.*, 108(16):6369–6373.

Luzar, A. and Chandler, D. (1996). Hydrogen-bond kinetics in liquid water. *Nature*, 379(6560):55–57.

Mancinelli, R., Botti, A., Bruni, F., Ricci, M. A., and Soper, A. K. (2007a). Hydration of Sodium, Potassium, and Chloride Ions in Solution and the Concept of Structure Maker/Breaker. *J. Phys. Chem. B*, 111(48):13570–13577.

Mancinelli, R., Botti, A., Bruni, F., Ricci, M. A., and Soper, A. K. (2007b). Perturbation of water structure due to monovalent ions in solution. *Phys. Chem. Chem. Phys.*, 9(23):2959.

Marcus, Y. (2009). Effect of Ions on the Structure of Water: Structure Making and Breaking. *Chem. Rev.*, 109(3):1346–1370.

Marsalek, O. and Markland, T. E. (2016). Ab initio molecular dynamics with nuclear quantum effects at classical cost: Ring polymer contraction for density functional theory. *J. Chem. Phys.*, 144(5):054112.

Marx, D. and Parrinello, M. (1996). Ab initio path integral molecular dynamics: Basic ideas. *J. Chem. Phys.*, 104(11):4077–4082.

Marzari, N., Mostofi, A. A., Yates, J. R., Souza, I., and Vanderbilt, D. (2012). Maximally localized Wannier functions: Theory and applications. *Rev. Mod. Phys.*, 84(4):1419–1475.

Marzari, N. and Vanderbilt, D. (1997). Maximally localized generalized Wannier functions for composite energy bands. *Phys. Rev. B*, 56(20):12847–12865.

Max, J.-J. and Chapados, C. (2009). Isotope effects in liquid water by infrared spectroscopy. III. H2O and D2O spectra from 6000to0cm-1. *J. Chem. Phys.*, 131(18):184505.

McQuarrie, D. A. (2000). *Statistical mechanics*. University Science Books, Sausalito, Calif.

Megyes, T., Bálint, S., Grósz, T., Radnai, T., Bakó, I., and Sipos, P. (2008). The structure of aqueous sodium hydroxide solutions: A combined solution x-ray diffraction and simulation study. *J. Chem. Phys.*, 128(4):044501.

Miceli, G., de Gironcoli, S., and Pasquarello, A. (2015). Isobaric first-principles molecular dynamics of liquid water with nonlocal van der Waals interactions. *J. Chem. Phys.*, 142(3):034501.

Migliorati, V., Sessa, F., Aquilanti, G., and D'Angelo, P. (2014). Unraveling halide hydration: A high dilution approach. *J. Chem. Phys.*, 141(4):044509.

Morrone, J. A. and Car, R. (2008). Nuclear Quantum Effects in Water. *Phys. Rev. Lett.*, 101(1).

Møgelhøj, A., Kelkkanen, A. K., Wikfeldt, K. T., Schiøtz, J., Mortensen, J. J., Pettersson, L. G. M., Lundqvist, B. I., Jacobsen, K. W., Nilsson, A., and Nørskov, J. K. (2011). Ab Initio van der Waals Interactions in Simulations of Water Alter Structure from Mainly Tetrahedral to High-Density-Like. *J. Phys. Chem. B*, 115(48):14149–14160.

Neilson, G. W., Mason, P. E., Ramos, S., and Sullivan, D. (2001). Neutron and X–ray scattering studies of hydration in aqueous solutions. *Philos. Trans. Royal Soc. A*, 359(1785):1575–1591.

Nilsson, A., Nordlund, D., Waluyo, I., Huang, N., Ogasawara, H., Kaya, S., Bergmann, U., Näslund, L. r., Öström, H., Wernet, P., Andersson, K. J., Schiros, T., and Pettersson, L. G. M. (2010). X-ray absorption spectroscopy and X-ray Raman scattering of water and ice; an experimental view. *J Electron Spectros. Relat. Phenomena*, 177(2):99–129.

Nilsson, A. and Pettersson, L. G. M. (2015). The structural origin of anomalous properties of liquid water. *Nat. Commun.*, 6:8998.

Nosé, S. (1984). A unified formulation of the constant temperature molecular dynamics methods. *J. Chem. Phys.*, 81(1):511–519.

Ohtaki, H. and Radnai, T. (1993). Structure and dynamics of hydrated ions. *Chem. Rev.*, 93(3):1157–1204.

Parrinello, M. and Rahman, A. (1980). Crystal Structure and Pair Potentials: A Molecular-Dynamics Study. *Phys. Rev. Lett.*, 45(14):1196–1199.

Pehlke, E. and Scheffler, M. (1993). Evidence for site-sensitive screening of core holes at the Si and Ge (001) surface. *Phys. Rev. Lett.*, 71(14):2338–2341.

Perdew, J. P. (2001). Jacob's ladder of density functional approximations for the exchange-correlation energy. In *AIP Conference Proceedings*, volume 577, pages 1–20, Antwerp (Belgium). AIP. ISSN: 0094243X.

Perdew, J. P., Burke, K., and Ernzerhof, M. (1996a). Generalized Gradient Approximation Made Simple. *Phys. Rev. Lett.*, 77(18):3865–3868.

Perdew, J. P., Burke, K., and Ernzerhof, M. (1997). Generalized Gradient Approximation Made Simple [Phys. Rev. Lett. 77, 3865 (1996)]. *Phys. Rev. Lett.*, 78(7):1396–1396.

Perdew, J. P., Ernzerhof, M., and Burke, K. (1996b). Rationale for mixing exact exchange with density functional approximations. *J. Chem. Phys.*, 105(22):9982–9985.

Perdew, J. P. and Zunger, A. (1981). Self-interaction correction to density-functional approximations for many-electron systems. *Phys. Rev. B*, 23(10):5048–5079.

Perera, L. and Berkowitz, M. L. (1992). Structure and dynamics of $Cl^-(H_2O)_{20}$ clusters: The effect of the polarizability and the charge of the ion. *J. Chem. Phys.*, 96(11):8288–8294.

Pettersson, L. G. M., Henchman, R. H., and Nilsson, A. (2016). Water—The Most Anomalous Liquid. *Chem. Rev.*, 116(13):7459–7462.

Pham, T. A., Ogitsu, T., Lau, E. Y., and Schwegler, E. (2016). Structure and dynamics of aqueous solutions from PBE-based first-principles molecular dynamics simulations. *J. Chem. Phys.*, 145(15):154501.

Piatkowski, L., Zhang, Z., Backus, E. H. G., Bakker, H. J., and Bonn, M. (2014). Extreme surface propensity of halide ions in water. *Nat. Commun.*, 5(1).

Plimpton, S. (1995). Fast Parallel Algorithms for Short–Range Molecular Dynamics. *J. Comput. Phys.*, page 42.

Prendergast, D. and Galli, G. (2006). X-Ray Absorption Spectra of Water from First Principles Calculations. *Phys. Rev. Lett.*, 96(21):215502.

Prendergast, D., Grossman, J. C., and Galli, G. (2005). The electronic structure of liquid water within density-functional theory. *J. Chem. Phys.*, 123(1):014501.

Rohlfing, M. and Louie, S. G. (2000). Electron-hole excitations and optical spectra from first principles. *Phys. Rev. B*, 62(8):4927–4944.

Sa\lek, P., Helgaker, T., Vahtras, O., \AAgren, H., Jonsson, D., and Gauss, J. (2005). A comparison of density-functional-theory and coupled-cluster frequency-dependent polarizabilities and hyperpolarizabilities. *Mol. Phys.*, 103(2-3):439–450.

Santra, B., DiStasio, R. A., Martelli, F., and Car, R. (2015). Local structure analysis in *ab initio* liquid water. *Mol. Phys.*, 113(17-18):2829–2841.

Schmidt, D. A., Scipioni, R., and Boero, M. (2009a). Water Solvation Properties: An Experimental and Theoretical Investigation of Salt Solutions at Finite Dilution. *J. Phys. Chem. A*, 113(27):7725–7729.

Schmidt, J., VandeVondele, J., Kuo, I.-F. W., Sebastiani, D., Siepmann, J. I., Hutter, J., and Mundy, C. J. (2009b). Isobaric-Isothermal Molecular Dynamics Simulations Utilizing Density Functional Theory: An Assessment of the Structure and Density of Water at Near-Ambient Conditions. *J. Phys. Chem. B*, 113(35):11959–11964.

Schreck, S. and Wernet, P. (2016). Isotope effects in liquid water probed by transmission mode x-ray absorption spectroscopy at the oxygen K-edge. *J. Chem. Phys.*, 145(10):104502.

Seidel, R., Thürmer, S., and Winter, B. (2011). Photoelectron spectroscopy meets aqueous solution: Studies from a vacuum liquid microjet. *J. Phys. Chem. Lett.*, 2(6):633–641.

Shannon, R. D. (1976). Revised effective ionic radii and systematic studies of interatomic distances in halides and chalcogenides. *Acta Crystallogr. A*, 32(5):751–767.

Sharkas, K., Wagle, K., Santra, B., Akter, S., Zope, R. R., Baruah, T., Jackson, K. A., Perdew, J. P., and Peralta, J. E. (2020). Self-interaction error overbinds water clusters but cancels in structural energy differences. *Proc. Natl. Acad. Sci. U.S.A.*, 117(21):11283–11288. Publisher: National Academy of Sciences Section: Physical Sciences.

Sharma, M., Resta, R., and Car, R. (2005). Intermolecular Dynamical Charge Fluctuations in Water: A Signature of the H-Bond Network. *Phys. Rev. Lett.*, 95(18):187401.

Shiratani, E. and Sasai, M. (1996). Growth and collapse of structural patterns in the hydrogen bond network in liquid water. *J. Chem. Phys.*, 104(19):7671–7680.

Sholl, D. S. and Steckel, J. A. (2009). *Density functional theory: a practical introduction*. Wiley, Hoboken, N.J. OCLC: ocn245025462.

Skinner, L. B., Huang, C., Schlesinger, D., Pettersson, L. G. M., Nilsson, A., and Benmore, C. J. (2013). Benchmark oxygen-oxygen pair-distribution function of ambient water from x-ray diffraction measurements with a wide Q-range. *J. Chem. Phys.*, 138(7):074506.

Slater, J. C., Mann, J. B., Wilson, T. M., and Wood, J. H. (1969). Nonintegral Occupation Numbers in Transition Atoms in Crystals. *Phys. Rev.*, 184(3):672–694.

Slater, J. C. and Wood, J. H. (1970). Statistical exchange and the total energy of a crystal. *Int. J. Quantum Chem.*, 5(S4):3–34.

Smith, J. D., Cappa, C. D., Messer, B. M., Drisdell, W. S., Cohen, R. C., and Saykally, R. J. (2006). Probing the Local Structure of Liquid Water by X-ray Absorption Spectroscopy†. *J. Phys. Chem. B*, 110(40):20038–20045.

Smith, J. D., Saykally, R. J., and Geissler, P. L. (2007). The Effects of Dissolved Halide Anions on Hydrogen Bonding in Liquid Water. *J. Am. Chem. Soc.*, 129(45):13847–13856.

Smith, J. W. and Saykally, R. J. (2017). Soft X-ray Absorption Spectroscopy of Liquids and Solutions. *Chem. Rev.*, 117(23):13909–13934.

Soper, A. K. (2001). Tests of the empirical potential structure refinement method and a new method of application to neutron diffraction data on water. *Mol. Phys.*, 99(17):1503–1516.

Soper, A. K. (2005). Partial structure factors from disordered materials diffraction data: An approach using empirical potential structure refinement. *Phys. Rev. B*, 72(10):104204.

Soper, A. K. (2013). The Radial Distribution Functions of Water as Derived from Radiation Total Scattering Experiments: Is There Anything We Can Say for Sure? *Int. Sch. Res. Notices*, page 279463.

Soper, A. K. (2019). Is water one liquid or two? *J. Chem. Phys.*, 150(23):234503.

Soper, A. K. and Benmore, C. J. (2008). Quantum Differences between Heavy and Light Water. *Phys. Rev. Lett.*, 101(6).

Spicer, C. W., Chapman, E. G., Finlayson-Pitts, B. J., Plastridge, R. A., Hubbe, J. M., Fast, J. D., and Berkowitz, C. M. (1998). Unexpectedly high concentrations of molecular chlorine in coastal air. *Nature*, 394(6691):353–356.

Stillinger, F. H. (1980). Water Revisited. *Science*, 209(4455):451–457.

Sun, J., Remsing, R. C., Zhang, Y., Sun, Z., Ruzsinszky, A., Peng, H., Yang, Z., Paul, A., Waghmare, U., Wu, X., Klein, M. L., and Perdew, J. P. (2016). Accurate first-principles structures and energies of diversely bonded systems from an efficient density functional. *Nat. Chem.*, 8(9):831–836.

Sun, J., Ruzsinszky, A., and Perdew, J. P. (2015). Strongly Constrained and Appropriately Normed Semilocal Density Functional. *Phys. Rev. Lett.*, 115(3):036402.

Sun, Z., Chen, M., Zheng, L., Wang, J., Santra, B., Shen, H., Xu, L., Kang, W., Klein, M. L., and Wu, X. (2017). X-ray absorption of liquid water by advanced *ab initio* methods. *Phys. Rev. B*, 96(10).

Sun, Z., Zheng, L., Chen, M., Klein, M. L., Paesani, F., and Wu, X. (2018). Electron-Hole Theory of the Effect of Quantum Nuclei on the X-Ray Absorption Spectra of Liquid Water. *Phys. Rev. Lett.*, 121(13):137401.

Swartz, C. W. and Wu, X. (2013). Ab initio Studies of Ionization Potentials of Hydrated Hydroxide and Hydronium. *Phys. Rev. Lett.*, 111(8):087801.

Tao, J., Perdew, J. P., Staroverov, V. N., and Scuseria, G. E. (2003). Climbing the Density Functional Ladder: Nonempirical Meta–Generalized Gradient Approximation Designed for Molecules and Solids. *Phys. Rev. Lett.*, 91(14):146401.

Tarek, M. and Tobias, D. J. (2002). Role of Protein-Water Hydrogen Bond Dynamics in the Protein Dynamical Transition. *Phys. Rev. Lett.*, 88(13):138101.

Thomson, J. F. (2006). PHYSIOLOGICAL EFFECTS OF D2O IN MAMMALS*. *Ann. N. Y. Acad. Sci.*, 84(16):736–744.

Thämer, M., Marco, L. D., Ramasesha, K., Mandal, A., and Tokmakoff, A. (2015). Ultrafast 2D IR spectroscopy of the excess proton in liquid water. *Science*, 350(6256):78–82.

Tkatchenko, A. and Scheffler, M. (2009). Accurate Molecular Van Der Waals Interactions from Ground-State Electron Density and Free-Atom Reference Data. *Phys. Rev. Lett.*, 102(7):073005.

Tobias, D. J., Jungwirth, P., and Parrinello, M. (2001). Surface solvation of halogen anions in water clusters: An *ab initio* molecular dynamics study of the Cl-(H2O)6 complex. *J. Chem. Phys.*, 114(16):7036–7044.

Tongay, S., Suh, J., Ataca, C., Fan, W., Luce, A., Kang, J. S., Liu, J., Ko, C., Raghunathanan, R., Zhou, J., and *et al.* (2013). Defects activated photoluminescence in two-dimensional semiconductors: interplay between bound, charged and free excitons. *Sci. Rep.*, 3(1):2657.

Tongraar, A., T-Thienprasert, J., Rujirawat, S., and Limpijumnong, S. (2010). Structure of the hydrated Ca2+ and Cl-: Combined X-ray absorption measurements and QM/MM MD simulations study. *Phys. Chem. Chem. Phys.*, 12(36):10876–10887.

Tse, J. S., Shaw, D. M., Klug, D. D., Patchkovskii, S., Vankó, G., Monaco, G., and Krisch, M. (2008). X-Ray Raman Spectroscopic Study of Water in the Condensed Phases. *Phys. Rev. Lett.*, 100(9).

Tuckerman, M., Laasonen, K., Sprik, M., and Parrinello, M. (1995). *Ab initio* molecular dynamics simulation of the solvation and transport of hydronium and hydroxyl ions in water. *J. Chem. Phys.*, 103(1):150–161.

Tuckerman, M. E. (1997). On the Quantum Nature of the Shared Proton in Hydrogen Bonds. *Science*, 275(5301):817–820.

Tuckerman, M. E. (2002). *Ab initio* molecular dynamics: basic concepts, current trends and novel applications. *J. Phys. Condens. Matter*, 14(50):R1297–R1355.

Tuckerman, M. E., Alejandre, J., López-Rendón, R., Jochim, A. L., and Martyna, G. J. (2006). A Liouville-operator derived measure-preserving integrator for molecular dynamics simulations in the isothermal–isobaric ensemble. *J. Phys. A Math. Theor.*, 39(19):5629–5651.

Vanderbilt, D. (1985). Optimally smooth norm-conserving pseudopotentials. *Phys. Rev. B*, 32(12):8412–8415.

Verlet, L. (1967). Computer "Experiments" on Classical Fluids. I. Thermodynamical Properties of Lennard-Jones Molecules. *Phys. Rev.*, 159(1):98–103.

Vinson, J., Rehr, J. J., Kas, J. J., and Shirley, E. L. (2011). Bethe-Salpeter equation calculations of core excitation spectra. *Phys. Rev. B*, 83(11):115106.

Wang, H., Zhang, L., Han, J., and E, W. (2018). DeePMD-kit: A deep learning package for many-body potential energy representation and molecular dynamics. *Comput. Phys. Commun.*, 228:178–184.

Wang, J., Román-Pérez, G., Soler, J. M., Artacho, E., and Fernández-Serra, M.-V. (2011). Density, structure, and dynamics of water: The effect of van der Waals interactions. *J. Chem. Phys.*, 134(2):024516.

Wang, L., Ceriotti, M., and Markland, T. E. (2014). Quantum fluctuations and isotope effects in ab initio descriptions of water. *J. Chem. Phys.*, 141(10):104502.

Wang, Q., Suzuki, K., Nagashima, U., Tachikawa, M., and Yan, S. (2013). Geometric isotope effects on small chloride ion water clusters with path integral molecular dynamics simulations. *Chem. Phys.*, 426:38–47.

Wernet, P., Nordlund, D., Bergmann, U., Cavalleri, M., Odelius, M., Ogasawara, H., Naslund, L. A., Hirsch, T. K., Ojamae, L., Glatzel, P., Pettersson, L. G. M., and Nilsson, A. (2004). The structure of the first coordination shell in liquid water. *Science*, 304(5673):995–999. WOS:000221383300044.

Wiktor, J., Ambrosio, F., and Pasquarello, A. (2017). Note: Assessment of the SCAN+rVV10 functional for the structure of liquid water. *J. Chem. Phys.*, 147(21):216101.

Winter, B. and Faubel, M. (2006). Photoemission from liquid aqueous solutions. *Chem. Rev.*, 106(4):1176–1211. WOS:000236990300004.

Winter, B., Faubel, M., Hertel, I. V., Pettenkofer, C., Bradforth, S. E., Jagoda-Cwiklik, B., Cwiklik, L., and Jungwirth, P. (2006). Electron binding energies of hydrated H3O+ and OH-: Photoelectron spectroscopy of aqueous acid and base solutions combined with electronic structure calculations. *J. Am. Chem. Soc.*, 128(12):3864–3865.

Winter, B., Weber, R., Hertel, I. V., Faubel, M., Jungwirth, P., Brown, E. C., and Bradforth, S. E. (2005). Electron binding energies of aqueous alkali and halide ions: EUV photoelectron spectroscopy of liquid solutions and combined Ab initio and molecular dynamics calculations. *J. Am. Chem. Soc.*, 127:7203–7214.

Winter, B., Weber, R., Widdra, W., Dittmar, M., Faubel, M., and Hertel, I. V. (2004). Full Valence Band Photoemission from Liquid Water Using EUV Synchrotron Radiation. *J. Phys. Chem. A*, 108(14):2625–2632.

Xu, J., Chen, M., Zhang, C., and Wu, X. (2019). First-principles study of the infrared spectrum in liquid water from a systematically improved description of H-bond network. *Phys. Rev. B*, 99(20).

Xu, J., Sun, Z., Zhang, C., DelloStritto, M., Lu, D., Michael, L. K., and Wu, X. (2020). Importance of nuclear quantum effects on the hydration of chloride ion. *arXiv Prepr. arXiv2009.07304*. Publisher: APS.

Yamagami, M., Wakita, H., and Yamaguchi, T. (1995). Neutron diffraction study on chloride ion solvation in water, methanol, and N,N-dimethylformamide. *J. Chem. Phys.*, 103(18):8174–8178.

Yao, Y. and Kanai, Y. (2020). Temperature dependence of nuclear quantum effects on liquid water via artificial neural network model based on SCAN meta-GGA functional. *J. Chem. Phys.*, 153(4):044114.

Zeidler, A., Salmon, P. S., Fischer, H. E., Neuefeind, J. C., Simonson, J. M., Lemmel, H., Rauch, H., and Markland, T. E. (2011). Oxygen as a Site Specific Probe of the Structure of Water and Oxide Materials. *Phys. Rev. Lett.*, 107(14):145501.

Zeidler, A., Salmon, P. S., Fischer, H. E., Neuefeind, J. C., Simonson, J. M., and Markland, T. E. (2012). Isotope effects in water as investigated by neutron diffraction and path integral molecular dynamics. *J. Phys.: Condens. Matter*, 24(28):284126.

Zhang, C., Donadio, D., Gygi, F., and Galli, G. (2011a). First Principles Simulations of the Infrared Spectrum of Liquid Water Using Hybrid Density Functionals. *J. Chem. Theory Comput.*, 7(5):1443–1449.

Zhang, C., Pham, T. A., Gygi, F., and Galli, G. (2013). Communication: Electronic structure of the solvated chloride anion from first principles molecular dynamics. *J. Chem. Phys.*, 138(18):181102.

Zhang, C., Wu, J., Galli, G., and Gygi, F. (2011b). Structural and Vibrational Properties of Liquid Water from van der Waals Density Functionals. *J. Chem. Theory Comput.*, 7(10):3054–3061.

Zhang, C., Zhang, L., Xu, J., Tang, F., Santra, B., and Wu, X. (2020). Isotope effects in x-ray absorption spectra of liquid water. *Phys. Rev. B*, 102(11):115155. Publisher: American Physical Society.

Zhang, L., Han, J., Wang, H., Car, R., and E, W. (2018a). Deep Potential Molecular Dynamics: A Scalable Model with the Accuracy of Quantum Mechanics. *Phys. Rev. Lett.*, 120(14).

Zhang, L., Han, J., Wang, H., Saidi, W., Car, R., and E, W. (2018b). End-to-end Symmetry Preserving Inter-atomic Potential Energy Model for Finite and Extended Systems. In Bengio, S., Wallach, H., Larochelle, H., Grauman, K., Cesa-Bianchi, N., and Garnett, R., editors, *Advances in Neural Information Processing Systems 31*, pages 4436–4446. Curran Associates, Inc.

Zhang, L., Lin, D.-Y., Wang, H., Car, R., and E, W. (2019). Active learning of uniformly accurate interatomic potentials for materials simulation. *Phys. Rev. Mater.*, 3(2):023804. Publisher: American Physical Society.

Zheng, L., Chen, M., Sun, Z., Ko, H.-Y., Santra, B., Dhuvad, P., and Wu, X. (2018). Structural, electronic, and dynamical properties of liquid water by *ab initio* molecular dynamics based on SCAN functional within the canonical ensemble. *J. Chem. Phys.*, 148(16):164505.

APPENDIX A

COMPUTATIONAL RESOURCES AND SOFTWARE

A.1 Clusters and Supercomputers

Most of the *ab initio* molecular dynamics simulations in this dissertation are performed using the Edison Cray XC30 and Cori Cray XC40 supercomputers provided by the National Energy Scientific Computing center (NERSC). The large amount of *ab initio* data are stored with NERSC's High Performance Storage System (HPSS).

Most of the molecular dynamics simulations adopting artificial neural network force field as well as data analysis are completed using Owlsnest and Owlsnesttwo, two generations of high-performace and scientific computing clusters in Temple University.

A.2 Software packages

Most of *ab initio* molecular dynamics, self-consistent ground state calculations, and simulations of XAS at the static COHSEX level shown in this dissertation is performed using the standard distribution or the modified versions of QUANTUM-ESPRESSO package [Giannozzi et al., 2017]; an integrated suite of Open-Source computer codes for electronic-structure calculations and materials modeling at the nanoscale based on density-functional theory, plane waves, and pseudopotentials.

Some electronic ground state and vibration state calculations of water monomers are conducted with Vienna Ab initio Simulation Package (VASP); a computer program for atomic scale materials modelling, e.g. electronic structure calculations and quantum-mechanical molecular dynamics, from first principles.

Path integral deep potential molecular dynamics are completed using the combining of i-PI package [Kapil et al., 2019], DeePMD-kit package [Wang et al., 2018] and the Large-scale Atomic/Molecular Massively Parallel Simulator (LAMMPS) package [Plimpton, 1995], where i-PI is a universal force engine interface written in Python, designed to be used together with an ab-initio (or force-field based) evaluation of the interactions between the atoms; LAMMPS is an open-source classical molecular dynamics simulation code with a focus on materials modeling; DeePMD-kit is a package written in Python/C++, designed to minimize the effort required to build deep learning based model of inter-atomic potential energy and force field and to perform molecular dynamics.

The G_0W_0 calculation for the single particle energy levels from many-body perturbation theory were performed with the BerkeleyGW package [Hybertsen and Louie, 1986; Deslippe et al., 2012]; a many-body perturbation theory code for

excited states, using the GW method and the GW plus Bethe-Salpeter equation (GW-BSE) method to solve respectively for quasiparticle excitations and optical properties of materials.

APPENDIX B

SUPPORTING INFORMATION FOR CHAPTER 5

B.1 Path-integral deep potential molecular dynamics simulation

The liquid configurations of light and heavy water were generated using path-integral deep potential molecular dynamics (PI-DPMD) method which includes the following three steps.

1. Generation of training data from path-integral *ab initio* molecular dynamics

Born-Oppenheimer path-integral *ab initio* molecular dynamics (PI-AIMD) simulation of H_2O was carried out in an isobaric-isothermal (NPT) ensemble at ambient condition (300 K and 1.0 bar) for 11 ps with a time step of 0.48 fs. The nuclear and cell dynamics were controlled by the i-PI code [Ceriotti et al., 2014] in conjunction with the density functional theory (DFT) [Hohenberg and Kohn, 1964] potential energy computed with QUANTUM ESPRESSO [Giannozzi et al., 2009].

A periodically replicated cubic cell containing 64 water molecules was adopted.

The nuclear degrees of freedom were sampled using eight beads with a colored-noise generalized Langevin equation thermostat [Ceriotti et al., 2009b; Ceriotti and Manolopoulos, 2012] to accelerate the convergence of the quantum distribution. The pressure was controlled using an isotropic barostat as implemented in the i-PI code. The time constant associated with the dynamics of the piston was set to 200 fs. The cell was thermostatted by another generalized Langevin equation thermostat [Ceriotti et al., 2009a, 2010a] to enhance sampling efficiency.

The electronic potential energy surface (PES) at each PI-AIMD step was calculated using DFT with the strongly constrained and appropriately normed (SCAN) density functional [Sun et al., 2015] and optimized norm-conserving HSCV pseudopotentials [Hamann et al., 1979; Vanderbilt, 1985]. Only the gamma point was used to sample the Brillouin zone. The method described in Ref. [Bernasconi et al., 1995] was applied to keep a constant planewave kinetic energy cutoff of 130 Ry in the NPT simulation. To ensure access of sufficient planwaves to achieve a constant planewave kinetic energy, buffer planewaves were generated with 150 Ry and a reference lattice cell parameter of 12.66 Å. The thresholds for the convergence of self-consistent total potential energy and ionic forces were set to 6×10^{-6} Hartree and 1×10^{-3} Hartree/Bohr, respectively.

2. Training of the DPMD model

The atomic position, total potential energy E, ionic forces $\mathbf{F}_i$, and the stress tensor $\boldsymbol{\Xi}$ at each time step were extracted from the above mentioned 11 ps PI-AIMD trajectory and adopted as the input training data for the DPMD model. The training was conducted for 10^6 steps using the DeePMD-kit package [Wang

et al., 2018] interfaced with the Tensorflow library [Abadi et al., 2016] following the procedure described in Refs. [Zhang et al., 2018a]. First, the input data were transformed to local coordinate frames for every atom and its neighbors inside a cutoff distance of 6 Å to preserve the translational, rotational, and permutational symmetries of the environment. Then the Adam method [Kingma and Ba, 2017] was applied to optimize the deep neural network parameters with the loss function:

$$\mathcal{L}(p_\epsilon, p_f, p_\xi) = p_\epsilon \Delta\epsilon^2 + \frac{p_f}{3N}\sum_i |\Delta\mathbf{F}_i|^2 + \frac{p_\xi}{9}\|\Delta\boldsymbol{\xi}\|^2$$

, where $\Delta\epsilon$, $\Delta\mathbf{F}_i$, and $\Delta\boldsymbol{\xi}$ represent the differences between the training data and current DPMD prediction for the quantities $\epsilon \equiv E/N$, $\mathbf{F}_i$, and $\boldsymbol{\xi} \equiv \boldsymbol{\Xi}/N$, respectively, N is the number of atoms, p_ϵ, p_f, and p_ξ are tunable prefactors. In the training process of this work, p_ϵ and p_ξ progressively increase from 0.02 to 8, while p_f progressively decrease from 1000 to 1. The resulting root-mean-square error between the energy predicted by the DPMD model and that predicted by PI-AIMD is about 0.39 meV/atom.

3. PI-DPMD simulations

The obtained DPMD model was applied to conduct the PI-DPMD simulation using the i-PI code [Ceriotti et al., 2014] in conjunction with the DeePMD-kit package [Wang et al., 2018]. For both H_2O and D_2O, a 0.3 ns PI-DPMD simulation was conducted in an NPT ensemble at ambient condiction with a time step of 0.48 fs. The simulation cell was expanded to 128 water molecules to reduce the finite-size effects. The simulation parameters related to nuclear and cell dynamics are the same as those adopted in the PI-AIMD simulation in the first step, except that the atomic mass of deuterium was set to 2.01 u. The model trained using the trajectory of H_2O can be adopted to the PI-DPMD simulation of both H_2O and

D_2O, because H_2O and D_2O share the same underlying PES [Ko et al., 2019].

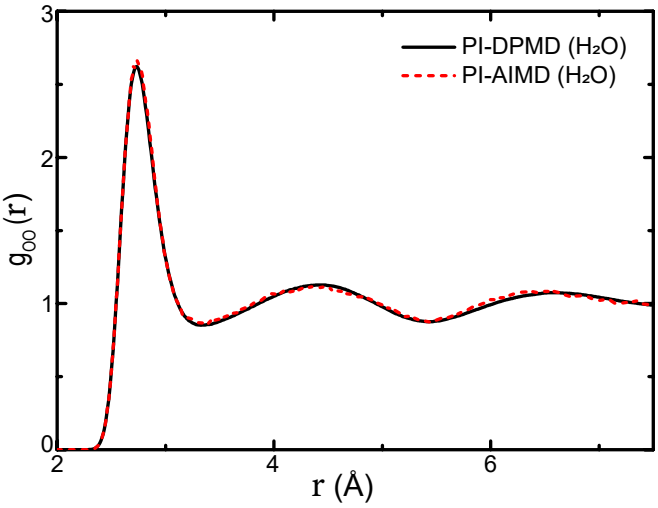

Figure B.1: $g_{OO}(r)$ of H_2O from PI-DPMD (solid black line) and PI-AIMD (dashed red line) simulations.

Figure B.1(a) shows that the oxygen-oxygen pair distribution function, $g_{OO}(r)$, of H_2O obtained from PI-DPMD agrees well with the $g_{OO}(r)$ obtained from PI-AIMD, suggesting that our PI-DPMD method can accurately reproduce the PI-AIMD trajectory.

B.2 Spectral calculations

Derived from Fermi's golden rule, the X-ray absorption spectroscopy (XAS) spectral cross section can be calculated as:

$$\sigma(\omega) = 4\pi^2 \alpha_0 \hbar\omega \sum_f |M_{if}|^2 \delta(\omega_{if} - \omega)$$

where α_0 is the fine-structure constant, ω_{if} is the angular frequency of the absorbed photon which has the energy $\hbar\omega_{if} = E_f - E_i$, with E_f and E_i representing the energy eigenvalues of the final and initial states, respectively. M_{if} is the transition matrix elements between the initial state $|\phi_i\rangle$ and final state $|\phi_f\rangle$, which can be

evaluated within the electric-dipole approximation as $M_{if} \sim \langle \phi_i | x | \phi_f \rangle$, averaging over the three Cartesian directions. The initial state $|\phi_i\rangle$ adopted in this work was the $1s$ atomic core state obtained from the all-electron calculation. The final state $|\phi_f\rangle$ was computed using our recently developed enhanced static Coulomb-hole and screened exchange (COHSEX) approximation [Kang and Hybertsen, 2010; Sun et al., 2017].

The static COHSEX method [Hedin, 1965] approximate the GW self-energy operator in terms of the Coulomb-hole (COH) contribution and the dynamically screened-exchange (SEX) contribution. The major error of the static COHSEX approximation with respect to the full GW calculations comes from the short-wavelength contributions of the assumed adiabatic accumulation of the Coulomb hole. The enhanced static COHSEX method [Kang and Hybertsen, 2010] introduces a universal function f to approximately include the dynamics screening in the original static model in the COHSEX formula. The enhanced static COH term can be expressed as:

$$\Sigma_{COH}(\mathbf{r}_1, \mathbf{r}_2; E) = \frac{1}{2}\delta(\mathbf{r}_1 - \mathbf{r}_2) \int W_p(q; E = 0) f(\frac{q}{k_f}) e^{-i\mathbf{q}\cdot\mathbf{r}} d\mathbf{q}$$

where W_p is the Coulomb hole, q is a plane wave, and k_f is the Fermi vector. The correction factor is

$$f(x) = \frac{1 + a_1 x + a_2 x^2 + a_3 x^3 + a_4 x^4 + a_5 x^5 + a_6 x^6}{1 + b_1 x + b_2 x^2 + b_3 x^3 + b_4 x^4 + b_5 x^5 + b_6 x^6}$$

, with $a_1 = 1.9085, a_2 = -0.542572, a_3 = -2.45811, a_4 = 3.08067, a_5 = -1.806, a_6 = 0.410031, b_1 = 2.01317, b_2 = -1.55088, b_3 = 1.58466, b_4 = 0.368325, b_5 = -1.68927$, and $b_6 = 0.599225$. For more details of the enhanced static COHSEX method, the reader is referred to Ref. [Kang and Hybertsen, 2010; Sun et al., 2017].

For both H_2O and D_2O, one representative snapshot, which has eight beads, was selected from the PI-DPMD trajectory, and used for the calculation of XAS spectra. The supercell containing 128 water molecules have been proved to be large enough to incorporate the long-range effects into the XAS spectra [Sun et al., 2017]. To sample the different local environments of disordered liquid water structure, 64 water molecules were randomly selected from the 128-molecule supercell and were excited. In each excitation, the excitation energies of 512 excitons were calculated. Therefore, for both light and heavy water, $1 \times 8 \times 64 \times 512 = 262144$ excitons were calculated. The final XAS spectra were averaged over all the excitons, which has been confirmed in Ref. [Sun et al., 2018] to be sufficient to generate a converged spectrum.

Due to the different local environments in liquid water for each excited oxygen atom, the XAS spectrum obtained from each excitation was shifted according to the standard approach to compute the core-level shifts [Pehlke and Scheffler, 1993] before added up. Subsequently, the XAS spectrum of each bead was aligned according to the position of the pre-edge [Sun et al., 2018]. Finally, the XAS spectra of H_2O and D_2O were aligned according to the position of the post-edge, because the post-edges of H_2O and D_2O coincide in experiment [Schreck and Wernet, 2016]. All calculated spectral were smoothed by Gaussian broadening with a full width at half maximum of 0.25 eV.

B.3 Decomposition of the XAS spectra

Figure B.2 shows the XAS spectra of light and heavy water contributed by water molecules in part $\mathrm{LSI}_{\mathcal{L}}$ and part $\mathrm{LSI}_{\mathcal{H}}$. As can be seen, from $\mathrm{LSI}_{\mathcal{L}}$ to

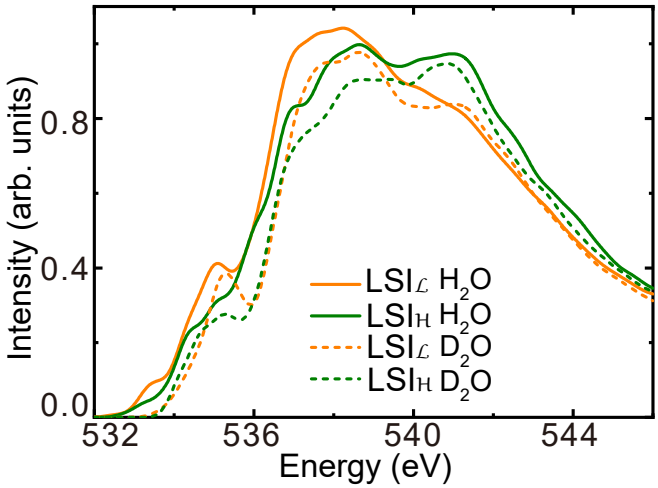

Figure B.2: XAS spectra of liquid H_2O (solid lines) and D_2O (dashed lines) contributed by water molecules in part $LSI_{\mathcal{L}}$ (orange lines) and part $LSI_{\mathcal{H}}$ (green lines).

$LSI_{\mathcal{H}}$ the excitation energies move to larger values for both light and heavy water. Moreover, the XAS spectra of heavy water have higher excitation energies, lower intensities, and less broadened spectral shape than light water for both the $LSI_{\mathcal{L}}$ and $LSI_{\mathcal{H}}$ parts.

APPENDIX C

SUPPORTING INFORMATION FOR CHAPTER 6

C.1 Classical and quantum molecular dynamics simulations

Aqueous solution of Cl^- ion with 0.87 molar concentration is studied in the canonical ensemble (NVT) at ambient condition. Both systems used a periodical cubic box with cell length of 12.42 Å, containing 63 H_2O molecules and one Cl^- ion. All first-principle molecular dynamics simulations were performed within Born-Oppenheimer approximation. Both classical AIMD and quantum PI-AIMD simulations were carried out based on the potential energy surface (PES) provided by the SCAN functional. Hamann-Schlüter-Chiang-Vanderbilt (HSCV) norm-conserving pseudopotentials [Vanderbilt, 1985] were used to model the core level electrons, while valence electrons were represented by a plane-wave basis (with 85 Ry cutoff) as implemented in the Quantum ESPRESSO package [Gian-

nozzi et al., 2009, 2017]. Only the gamma point was used to sample the Brillouin zone of the supercell. In AIMD, nuclei temperature was controlled by Nosé-hoover [Nosé, 1984; Hoover, 1985] method. In PI-AIMD, an 8-bead ring polymer with a colored-noise generalized Langevin equation thermostat (i.e. PIGLET) [Ceriotti et al., 2009b; Ceriotti and Manolopoulos, 2012] were used to model quantum nuclei fluctuations using the I-PI package [Kapil et al., 2019]. To address NQEs, light water were adopted in all simulations. The nuclear mass of hydrogen was set to 1.00794 a.m.u. while the nuclear mass of oxygen was set to 15.9995 a.m.u. Both simulations were performed at T=300 K with a time step of 0.48 fs, and last for over 40 ps and 15 ps (for AIMD and PI-AIMD, respectively) after equilibrium.

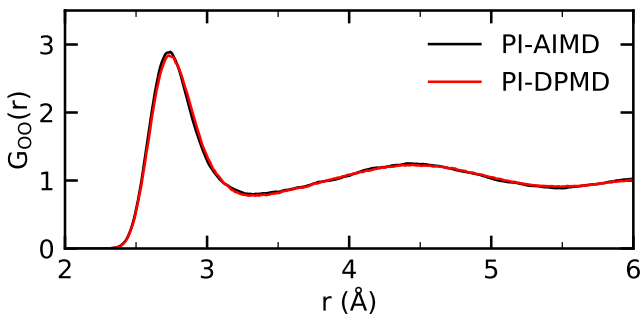

Figure C.1: O-O RDFs in pure water system obtained from PI-AIMD and PI-DPMD simulations.

For comparing, pure water systems with 64 H_2O molecules in periodic cubic box were simulated with the same parameters. In order to achieve better convergence of liquid structures, deep potential molecular dynamics (DPMD) [Zhang et al., 2018a] were adopted. After the training process, the deep learning base force field had a energy mean square error of 0.48 meV per atom. With DPMD, pure water simulations were extended to 480 and 160 ps for AIMD and PI-AIMD, respectively. To show the convergence of our DPMD simulation, we compare the oxygen-oxygen radial distribution function (RDF) obtained from both PI-AIMD and PI-DPMD

in Figure C.1.

C.2 Structure detail

Table C.1 shows details of positions of the first maxima and the first minima in Cl-O Cl-H RDFs as well as coordination numbers summarized from this work along with other previous studies. Compared to other exchange-correlation functional used by former studies [Bankura et al., 2013; Zhang et al., 2013; Gaiduk et al., 2014], the SCAN functional improves predictions of both $G_{ClO}(r)$ peaks and coordination numbers on the level of classical *ab initio* simulations without applying artificially increased temperature. SCAN provides a precise PES for Cl^-(aq) system and a favourable condition to study NQEs which heavily depend on the accurate description of PES.

Table C.1: Tabulated summaries of positions of the first maxima, minima and coordination numbers for $G_{ClO}(r)$ and $G_{ClH}(r)$. Mean values and errors of SCAN trajectories are estimated by 10 segments of each trajectory. Results from previous studies are listed as a reference.

Simulation	Temperature	Cl-O			Cl-H		
		r_{max}(Å)	r_{min}(Å)	N_{coord}	r_{max}(Å)	r_{min}(Å)	N_{coord}
SCAN-AIMD	300K	3.14±0.06	3.82±0.18	6.7±0.5	2.19±0.05	2.95±0.04	5.8±0.3
SCAN-PI-AIMD	300K	3.16±0.06	3.85±0.17	7.2±0.6	2.21±0.04	2.90±0.01	5.8±0.5
PBE[Zhang et al., 2013]	388K	3.11±0.01	3.79±0.17	6.1±0.9	2.15±0.03	2.84±0.03	4.9±0.1
PBE0[Zhang et al., 2013]	379K	3.14±0.01	3.83±0.04	6.4±0.3	2.21±0.01	2.90±0.06	5.2±0.3
PBE[Bankura et al., 2013]	330K	3.11±0.02	3.64±0.03	5.5±0.2	2.14±0.03	2.88±0.06	5.2±0.1
PBE+Ts[Bankura et al., 2013]	330K	3.14±0.01	3.78±0.12	6.3±0.9	2.17±0.02	2.93±0.06	5.2±0.3
PBE0[Bankura et al., 2013]	330K	3.14±0.02	3.72±0.12	5.8±0.7	2.18±0.01	2.86±0.15	5.1±0.5
PBE0+Ts[Bankura et al., 2013]	330K	3.16±0.02	3.73±0.12	6.3±0.8	2.18±0.03	2.90±0.11	5.5±0.2
PBE[Gaiduk et al., 2014]	400K	3.13±0.03	3.73±0.12	6.0±0.5			
PBE0[Gaiduk et al., 2014]	380K	3.13±0.02	3.78±0.08	6.2±0.5			
NaCl/expr[Mancinelli et al., 2007a]		3.16±0.11		6.9±1.0	2.19±0.16		6.0±1.1
KCl/expr[Mancinelli et al., 2007a]		3.14±0.17		7.0±1.1	2.18±0.04		6.1±1.0

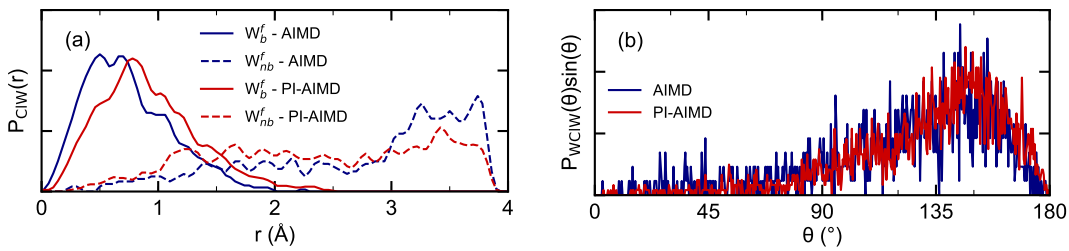

Figure C.2: (a) Distribution functions of the distance between Cl^- and centroids of both W_b^f (solid) and W_{nb}^f (dashed) in classical (blue) and quantum (red) Cl^- solution. (b) Angular distribution of W_b^f-Cl-W_{nb}^f in classical (blue) and quantum (red) Cl^- solution.

C.2.1 Hydration pattern

Chloride ion is a polarizable ion. Its polarization is determined by the configuration of the surrounding water molecules. Thus, it is important to understand the configuration of the Cl^- hydration shell. In this work, the first hydration shell of Cl^- is defined as water molecules within the first minima of Cl-O RDF, the cutoff of which is 3.82 and 3.84 Å for AIMD and PI-AIMD. As described in chapter 6, not all water molecules in the first hydration shell (W^f) are bonded to Cl^-. They can be classified by water molecules bonded to Cl^- (W_b^f) and water molecules in the first shell but non-bonded to Cl^- (W_{nb}^f). The distribution of W_b^f and W_{nb}^f are studied in detail. Figure C.2 shows the distribution of centroids of W_b^f and W_{nb}^f with respect to the position of Cl^-. Both W_b^f and W_{nb}^f have inhomogeneous distributions around the anion. In Figure C.2(a), the centroids of W_b^f exhibit a peak at ∼0.6 (0.8) Å in AIMD(PI-AIMD). By contrast, the centroids of W_{nb}^f in both simulation tend to locate further away from the solvated Cl^-. Moreover, in Figure C.2(b), centroids of W_b^f and W_{nb}^f form obtuse angles for both AIMD and PI-AIMD simulations. The above fact indicates that W_b^f and W_{nb}^f tend to occupy two opposite sides of the hydration shell. The asymmetric solvation of Cl^- in bulk

water is similar to the surface-enhanced effect as observed in cluster studies[Tobias et al., 2001].

C.2.2 Coordination numbers

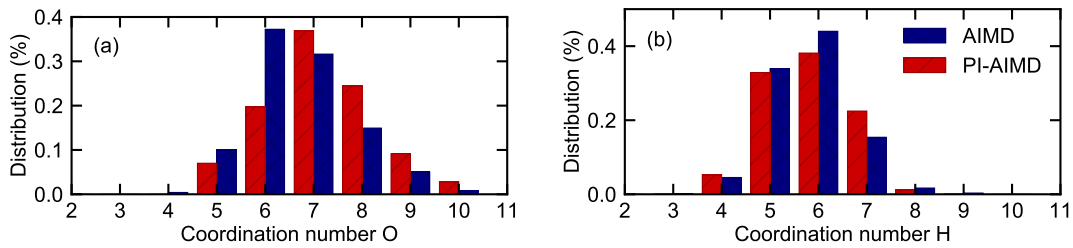

Figure C.3: Coordination number of (a) O and (b) H in the first hydration shell of classical (blue) and quantum (red) Cl^- solution.

As listed in Table C.1, the oxygen coordination numbers (CN) are 6.7 and 7.2 for AIMD and PI-AIMD simulations which are close to the experimental value of ~ 7.0. We show the distributions of oxygen and hydrogen CN in Figure C.3. It is worth mentioning that the distribution of oxygen CN centered at 6 in AIMD and moves to 7 in PI-AIMD, while both classical and quantum simulations has the hydrogen CN centered at 6. Under the influence of NQEs, more water molecules tend to squeeze into the first hydration shell with the oxygen site and leave the hydrogen site pointing away from (non-bonded to) the anion. This is consistent with the observation in Figure 6.4(a), where Cl^- shows increased probability locating at the oxygen site of a water molecule in PI-AIMD trajectories.

To address the above observation, the hydrogen (H)-bonding between water-water and ion-water are studied. A 3.5 Å O-O distance and 30° O-O-H angle (the angle between O-O direction and O-H covalent bond direction) cutoff [Luzar and Chandler, 1996] as well as a 3.9Å Cl-O distance and 30° Cl-O-H angle cutoff

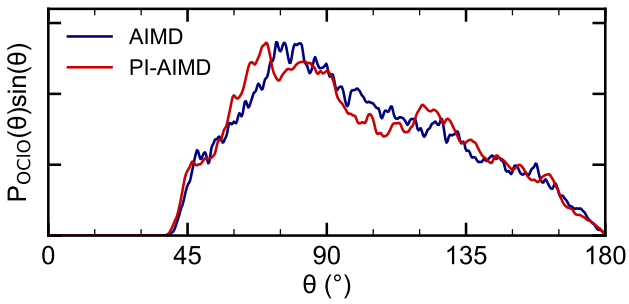

Figure C.4: Distribution functions of O-Cl-O in the first Cl^- hydration shell of classical (blue) and quantum (red) Cl^- solution.

[Wang et al., 2013] are adopted to characterize the H-bond for O-H and Cl-H, respectively. The average accept and donate H-bond numbers for both water and Cl^- are listed in Table C.2. Not surprisingly, both O-H and Cl-H H-bond are weaken due to the H-bond fluctuation from NQEs. Instead of bonding with Cl^-, more W^f tend to point H atoms away from Cl^- and donate H-bond to surrounding solvent water. Thus, under NQEs, the average number of accepting H-bonds for W^f is reduced, while the donating H-bonds count keep unchanged. Furthermore, the average number of W^f_b decrease from 5.03 in AIMD to 4.82 in PI-AIMD. The count of W^f_{nb} increases from 1.66 to 2.35 due to NQEs. Typically, we find that the most common configuration in the first hydration shell is 5 W^f_b with 1 W^f_{nb} in AIMD and 5 W^f_b with 2 W^f_{nb} in PI-AIMD. Considering the polarized nature of

Table C.2: Average accept donate H-bond count in chloride ion solution. Note that for donate number of water in the first shell only H-bond donate to water are considered.

	Accept	Donate	All
water-Classical (W-C)	1.78	1.78	3.56
water-Quantum (W-Q)	1.69	1.69	3.38
W-C-first shell	1.71	1.07	2.78
W-Q-first shell	1.56	1.07	2.63
Cl-Classical	5.03		
Cl-Quantum	4.82		

Cl^- as discussed above, the increased population of W^f_{nb} locates on the opposite side of Cl^- as compared to W^f_b. As a result, one observes a increased obtuse peak in the three body distributions of H-Cl-H as well as O-Cl-O (as shown in Figure 6.4(b) and Figure C.4).

C.3 Additional AIMD simulations: Cl^- ionic solution with AIMD and PI-AIMD at PBE-GGA level

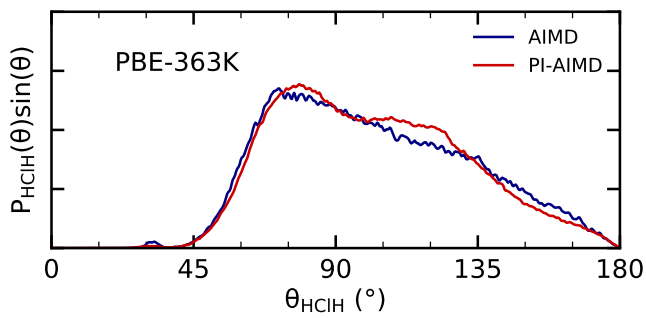

Figure C.5: Probability distribution of H-Cl-H angles in the first hydration shell of Cl^- ion in Cl^- solution at 363K obtained from both AIMD (blue) and PI-AIMD (red) simulations adopting the PBE functional.

In order to show the importance of NQEs on the hydration of Cl^- ion does not depend on the choice of XC functionals, we present another set of simulations adopting the PBE functional [Perdew et al., 1996a]. Similarly, we use 63 water molecules and a Cl^- ion to simulate the 0.8667 molarity solution. The length of the simulation cell is set to 12.44 Å. The system is set to an elevated temperature, 363K, within the canonical ensemble. The increase of temperature is a standard approach to mitigate the over structure error by PBE functional [Gaiduk and Galli, 2017]. Other parameters are set accordingly to the simulation with SCAN

functional. The length of AIMD and PI-AIMD trajectory are 50 ps and 20 ps, respectively. In order to capture the characteristic feature of NQEs, we show the H-Cl-H triple angular distribution functions from both trajectories in Figure C.5. In the AIMD trajectory, the H-Cl-H ADF shows a broad peak centered at ∼70 degree, while the second broader peak around 120∼135 degree is missing. In the PI-AIMD trajectory, the second peak appears at around 120 degree. Due to the drawback that PBE functionals overestimate the strength of H-bond in aqueous systems, the H-bonded and non-bonded water molecules around the Cl^- ion are not widely separated as modeled by the SCAN functional. As a result, the position of the second peak in H-Cl-H shifts slightly to a smaller value. Clearly, Cl^- solutions modeled by the PBE functional still show qualitatively similar nuclear quantum effects as that of the SCAN functional, which proofs that the importance of NQEs on the hydration of Chloride ion is a genuine physical effect.

C.4 Additional definitions

C.4.1 Centers of maximally localized Wannier functions and water electron pairs

The maximally localized Wannier functions (MLWFs) are generated by minimizing the second moment spread of each Wannier charge density based on occupied Kohn–Sham eigenstates of the system [Marzari et al., 2012]. MLWFs have been widely used to analyze chemical bonds in liquid systems combined with molecular dynamics [Tobias et al., 2001]. In the manuscript, we adopt centers of MLWFs and their relative distances to the atom to analyze the strength of H-bond

in Cl^- ion solution. Similar analysis have been carried out in pure liquid water [Chen et al., 2017] and solvated water ions in liquid water [Chen et al., 2018]. For each water molecule, one can find four centers of MLWF located around the oxygen atom within 1 Å. Two of the MLWF centers locate roughly at center of the O-H covalent bond, which are the bonding electron pairs. And the other two MLWF centers that are further away from the Hydrogen atoms, but close to the oxygen atom ($\sim$ 0.35 Å) are defined as the lone electron pairs. The natures of lone electron pairs can be further determined by the symmetry requirement, in which the line connecting the two lone electron pair of one water molecule is perpendicular to the plane determined by two hydrogen and one oxygen atom of the water.

C.4.2 Peak positions

Only one Cl^- ion is included in each snapshot along molecular dynamics trajectories. The sampling of Cl-water pairs is not as abundant as that of water-water interactions. As a result, the Cl-O RDFs show slightly wiggled curves. In order to extract well defined peak positions and keep consistency throughout different plots, we calculated the position of a given peak/trough by the following procedure. First, we take a section of curve around the given peak/trough within 1 Angstrom along the x-axis. Next, we fit the curve to a polynomial of eighth order using the least square method. Then, we take the position of the maximum/minimum in the polynomial as the peak position.

C.4.3 Normalized tetrahedral order parameter

In this work, we adopted a similar definition of Q as used by Chau *et al.* [Chau and Hardwick, 1998], where

$$Q = \frac{3}{32}\sum_{j=1}^{3}\sum_{k=j+1}^{4}(\cos\psi_{j,k} + \frac{1}{3})^2$$

. The Q has a value from 0 to 1, where 0 stands for a perfect tetrahedron structure, and 1 stands for non-tetrahedron structure. In other words, for a given water molecule, the higher value of Q indicates that it has a more disordered structure as compared to the perfect tetrahedral structure. In this regard, we calculated the averaged Q value for water molecules in both Cl^- ionic solutions (Q_s) and pure water (Q_w) from both AIMD and PI-AIMD trajectories. Base on the Q_s and Q_w, we calculated the normalized tetrahedral order parameter ($\bar{Q} = Q_s/Q_w$), which gives the anion's disruptive effect on the tetrahedral structure of pure water. Similar to the description before, for a given water molecule in the Cl^- solution, the higher value of $\bar{Q}$ shows that the Cl^- ion caused a severer disruption on the structure. On the other hand, $\bar{Q} = 1$ means that the Cl^- ion barely has any influence on the given water molecule, and it has a similar structure as in pure water. Furthermore, in Cl^- solution, we averaged Q_s for groups of water molecules which is in different solvation shell of Cl^- ion. Then we calculated and plotted the averaged $\bar{Q}$ for water molecules in the first, second, and third solvation shell of Cl^- ion in Figure. 6.4(a), which shows how the disruptive effect of Cl^- ion to the liquid structure decays over distances. From Figure. 6.4(a), one can tell that Cl^- shows a greater disruptive effect within the first solvation shell in classical simulations and the disruptive effect remains to the second and even third shell. However, with NQEs, the disruptive effect of Cl^- decays fast within the first hydration shell

and the liquid structure is able to return to the bulk water cases in second shell and beyond.

C.4.4 O-O RDFs within the first hydration shell of Cl^- ion

The O-O RDFs within the first hydration shell of Cl^- are obtained by taking the following steps. First, the O-O RDF of a single water molecule a takes the form, $g_{\mathrm{a}}(\overrightarrow{r}) = \mathrm{d}n(\overrightarrow{r})/\mathrm{d}\overrightarrow{r}$, where n is the particle density of oxygen atom. Then, considering only oxygen atoms within the first coordination shell of Cl^- ion, the O-O RDF within the first Cl^- hydration shell of water molecule a can be written as $g_{\mathrm{a}}^{1st}(\overrightarrow{r}) = \mathrm{d}n^{1st}(\overrightarrow{r})/(\mathrm{d}\overrightarrow{r})$. Next, one can integral over the angular parts $g_{\mathrm{a}}^{1st}(r) = \int g_{\mathrm{a}}^{1st}(\overrightarrow{r})\frac{\mathrm{d}\overrightarrow{r}}{\mathrm{d}r}$. Finally, one get the general the O-O RDF within the first Cl- hydration $g_{\mathrm{OO}}^{1st}(r)$ by averaging over all water molecules that is in the first coordination shell of Cl- ion.

APPENDIX D

SUPPORTING INFORMATION FOR CHAPTER 7

D.1 Computational details of single-particle energy levels from many-body perturbation theory

Since the GW calculation requires a large amount of the computation resources, we limited the number of the snapshots which included in the calculation. We first randomly chose snapshots but set the average number of the bonded and non-bonded water molecules from the selected snapshots close to the number of the most common configurations. Typically, we find that within the 1st hydration shell, the most common configuration is $N_{bonded} = 5$ with $N_{non\text{-}bonded} = 1$ in the AIMD structure, and $N_{bonded} = 5$ with $N_{non\text{-}bonded} = 2$ in the PI-AIMD structure. The selected 8 snapshots from AIMD trajectory give $N_{bonded} = 5.25$ with

$N_{\text{non-bonded}} = 1.125$, while the 8 bead from the selected snapshot give $N_{\text{bonded}} = 4.75$ with $N_{\text{non-bonded}} = 2.25$.

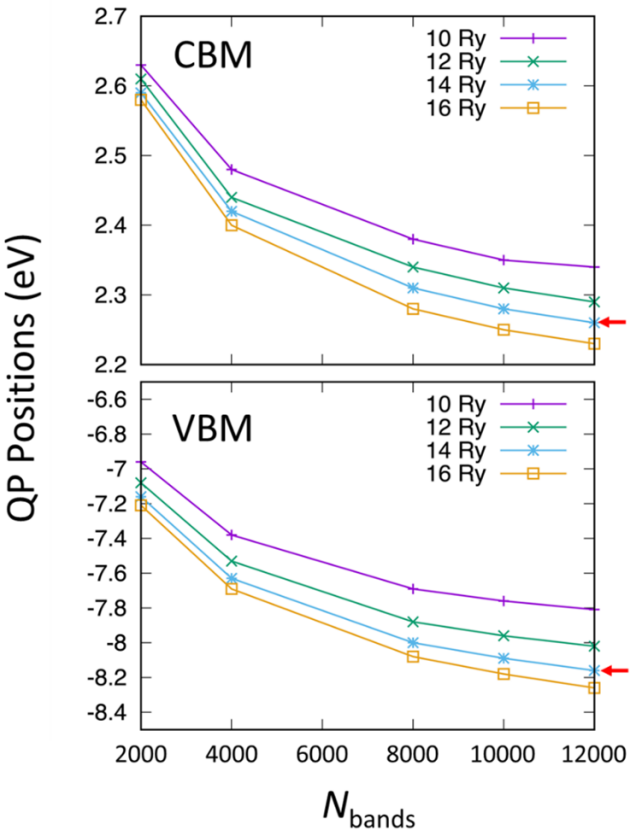

Figure D.1: VBM and CBM quasi-particle energy positions as a function of number of bands (N_{bands} and ϵ^{-1} cutoff) used. The red arrows highlight the parameters used in the present study. Lines are for eye-guidance.

The G_0W_0 calculation for the single particle energy levels from many-body perturbation theory were performed with the BerkeleyGW package [Hybertsen and Louie, 1986; Deslippe et al., 2012], starting from PBE XC wavefunctions. We set the kinetic energy cutoff for the wavefunctions to 85 Ry and used HSCV pseudopotential for H, O and Cl atoms. A single Γ point in the Brillouin zone was used throughout. All our static COHSEX calculations were carried out with a dielectric matrix, ϵ^{-1}, that included plane wave components up to 14 Ry and 12000 bands in the sum over bands in the calculation of polarizability. The self-energies

were all computed in the static limit (i.e. the static COHSEX approximation). To confirm that the adopted parameters (N_{bands} = 2000, ϵ^{-1} cutoff of 14 Ry) are sufficient for convergence, we look at the convergence of the conduction band minimum (CBM) and valence band maximum (VBM), which is shown in Figure D.1. We find that the VBM and CBM calculated with the adopted parameters (N_{bands} = 12000, ϵ^{-1} cutoff of 14 Ry) are within 0.1 eV accuracy, which is enough for the current study in the balance of the computation costs. As a comparison, the previous G_0W_0 calculation based on 32 H_2O pure water system adopted the parameters N_{bands} = 2000 and an ϵ^{-1} cutoff value of 12 Ry [Chen et al., 2016].

APPENDIX E

LIST OF PUBLICATIONS

E.1 Ongoing works and manuscript under review

- **Jianhang Xu**, Chunyi Zhang, Linfeng Zhang, Biswajit Santra, and Xifan Wu, *Nuclear quantum effects on molecular structure and electronic properties of liquid water via deep potential molecular dynamics based on SCAN functional* (Under review of Phys. Rev. B)

- **Jianhang Xu**, Zhaoru Sun, Chunyi Zhang, Mark DelloStritto, Michael L. Klein, Deyu Lu, and Xifan Wu, *Importance of Nuclear Quantum Effects on the Hydration of Chloride Ion.* (Under review of Phys. Rev. Lett.)

- Fujie Tang, **Jianhang Xu**, Diana Y. Qiu, and Xifan Wu, *Impact of nuclear quantum effects on the electronic structure of the aqueous solvation chloride ions* (Under review of J. Phys. Chem. Lett.)

- Mohan Chen, Chunyi zhang, Linfeng Zhang, Han Wang, **Jianhang Xu**,

Hsin-Yu Ko, Biswajit Santra, John P Perdew, Weinan E, and Xifan Wu, *Theoretical Studies of Water by Climbing Jacob's Ladder with Deep Neural Network* (Manuscript in progress)

E.2 Published works

- **Jianhang Xu**, Mohan Chen, Cui Zhang, and Xifan Wu, *First-principles study of the infrared spectrum in liquid water from a systematically improved description of H-bond network.*
  Phys. Rev. B 99, 205123 [2019]

- Chunyi Zhang, Linfeng Zhang, **Jianhang Xu**, Fujie Tang, Biswajit Santra, and Xifan Wu, *Isotope effects on the X-ray absorption spectra of liquid water.*
  Phys. Rev. B 102, 115155 [2020]

- Shanshan Yang, Mohan Chen, Yudan, Su, **Jianhang Xu**, Xifan Wu, and Chuanshan Tian, *Stabilization of hydroxide ion at interface of hydrophobic monolayer on water via reduced proton transfer*
  Phys. Rev. Lett. 125 (15), 156803 [2020]

- Fujie Tang, Xuanyuan Jiang, Hsin-Yu Ko, **Jianhang Xu**, Mehmet Topsakal, Guanhua Hao, Alpha T. N'Diaye, Peter A. Dowben, Deyu Lu, Xiaoshan Xu, and Xifan Wu, *Probing ferroelectricity by x-ray absorption spectroscopy in molecular crystals*
  Phys. Rev. Materials 4, 034401 [2020]

- Mark DelloStritto, **Jianhang Xu**, Xifan Wu and Michael L. Klein, *Aqueous solvation of the chloride ion revisited with density functional theory: impact*

of correlation and exchange approximations.

Phys. Chem. Chem. Phys. [2020]

- Tatsuhiko Ohto, Mayank Dodia, **Jianhang Xu**, Sho Imoto, Fujie Tang, Frederik Zysk, Thomas D. Kühne, Yasuteru Shigeta, Mischa Bonn, Xifan Wu, Yuki Nagata, *Accessing the Accuracy of Density Functional Theory through Structure and Dynamics of the Water–Air Interface.*

  J. Phys. Chem. Lett. 10, 17, 4914-4919 [2019]

- Liying Zhou, **Jianhang Xu**, Limei Xu, Xifan Wu, *Importance of van der Waals effects on the hydration of metal ions from the Hofmeister series.*

  J. Chem. Phys. 150, 124505 [2019]